Eindhoven University of Technology

MASTER

Numerical study of the influence of secondary jets on the separation efficiency of an air curtain

de Haas, K.

Award date:
2019

Link to publication

Disclaimer
This document contains a student thesis (bachelor's or master's), as authored by a student at Eindhoven University of Technology. Student theses are made available in the TU/e repository upon obtaining the required degree. The grade received is not published on the document as presented in the repository. The required complexity or quality of research of student theses may vary by program, and the required minimum study period may vary in duration.

General rights
Copyright and moral rights for the publications made accessible in the public portal are retained by the authors and/or other copyright owners and it is a condition of accessing publications that users recognise and abide by the legal requirements associated with these rights.

- Users may download and print one copy of any publication from the public portal for the purpose of private study or research.
- You may not further distribute the material or use it for any profit-making activity or commercial gain

EINDHOVEN UNIVERSITY OF TECHNOLOGY

Department of Applied Physics
Turbulence and Vortex Dynamics

Numerical study of the influence of secondary jets on the separation efficiency of an air curtain

Master thesis

Kimberley de Haas

Supervised by:

prof. dr. ir. G.J.F. van Heijst

dr. ir. T.A.J. van Hooff

C.A. Alanis Ruiz (MSc, PDEng)

March 26, 2019

Abstract

An air curtain is an aerodynamic seal between two environments in the form of a plane turbulent impinging jet. It aims to separate two spaces while avoiding an obstructed passage, such as a door. Air curtains are often used in public buildings where doors are frequently used, to prevent heat loss. Aside from energy efficiency and air quality, air curtains are also used for other purposes, such as thermal comfort, fire and chemical safety. In this study, the influence of secondary jets on the separation efficiency of an air curtain is investigated by means of 2D numerical simulations. The distance between the jets and the discharge velocities are varied to find an optimal configuration. Steady RANS simulations are performed to gather information about velocity and entrainment. Unsteady RANS simulations are conducted to measure species transfer across the air curtains directly. It can be concluded that secondary jets significantly reduce the species transfer across the jets compared to a single jet. The species transfer across the jets is dependent on the entrainment velocity, which controls the amount of species entering the jet, and the centreline velocity, which controls how fast the species are transported through the jets. The entrainment velocity, and also the species transfer, is minimised when the secondary jets have approximately the same velocity as the main jet. However, an optimal distance between the jets has not been found.

Acknowledgements

I would like to thank my supervisors GertJan van Heijst and Twan van Hooff for making it possible to do a graduation project at both the Department of Applied Physics and the Department of the Built Environment. The collaboration was very pleasant and I learned a lot from both fields of study. Combining fluid dynamics and building physics was the most rewarding for me. A special thanks to GertJan, for always having his door open for questions or a casual talk, especially during the past year as my supervisor, but also during the rest of my studies as my mentor. I am also grateful to my daily supervisor Claudio Alanis Ruiz for always replying immediately to my emails and taking the time to assist me during this project. Last but not least, a great thanks to all the master students in room CC 4.11 for all the inspiring lunch breaks, walks, and much-needed coffee breaks.

Contents

Nomenclature

α	Opening angle of a jet
$\boldsymbol{\omega}$	Vorticity vector [s^{-1}]
Δt	Time step [s]
$\delta_{0.5}$	Jet half width [m]
ϵ	Turbulence dissipation [m^2/s^3]
$\mathbf{F_v}$	Viscous forces vector [kg/ms^2]
$\mathbf{g}$	Gravitational acceleration vector [m/s^2]
$\mathbf{n}$	Normal (unit) vector
$\mathbf{u}$	Velocity vector [m/s]
μ_t	Turbulent or eddy viscosity
ν	Kinematic viscosity [m^2/s]
ω	Specific turbulence dissipation [s^{-1}]
ω_c	Critical value of the vorticity [s^{-1}]
$\Phi_{P_{jet}}$	Jet momentum flux [kg/s^2]
ψ	Stream function [m^2/s]
ρ	Fluid density [kg/m^3]
σ	Standard deviation
c	Species concentration [kg/m^3]
C_μ	Model constant
c_t	Mass fraction of tracer air
Cr	Courant number
D	Diffusion coefficient [m^2/s]
d	Distance between the nozzles of the secondary jets and the main jet [m]
D_H	Hydraulic diameter [m]
D_t	Turbulent diffusion coefficient [m^2/s]
F_s	Safety factor

h_{jet}	Height of the computational domain [m]
h_{outlet}	Size of the pressure outlets [m]
h_p	Length of the jet potential core [m]
I	Turbulence intensity [%]
k	Turbulent kinetic energy [m^2/s^2]
L	Characteristic length scale [m]
l	Turbulence length scale [m]
P	Pressure [Pa]
p	Order of accuracy of the numerical scheme
Q	Volume flux [m^2/s]
R	Velocity ratio: $R = V_2^*/V_1^*$
R_{jet}	Jet radius [m]
Re	Reynolds number
S	Sources and sinks of species
Sc_t	Turbulent Schmidt number
t	Time [s]
T_c	Circulation time [s]
u	x-component of the velocity [m/s]
V	Characteristic fluid velocity [m/s]
v	y-component of the velocity [m/s]
V_0	Jet discharge velocity [m/s]; $V_0 = \sqrt{V_1^2 + V_2^2}$
V_0^*	Desired jet discharge velocity [m/s]
V_1	Discharge velocity of the main jet [m/s]
V_1^*	Velocity imposed at the velocity inlet of the main jet [m/s]
V_2	Discharge velocity of the secondary jets [m/s]
V_2^*	Velocity imposed at the velocity inlets of the secondary jets [m/s]
V_E	Entrainment velocity [m/s]
v_E	Theoretical entrainment velocity [m/s]
V_{max}	Maximum velocity [m/s]
v_{max}	Theoretical centreline velocity [m/s]
V_x	x-component of the velocity [m/s]
V_y	y-component of the velocity [m/s]
w	z-component of the velocity [m/s]

w_1	Nozzle width of the main jet [m]
w_2	Nozzle width of the secondary jets [m]
w_{domain}	Width of the computational domain [m]
w_{jet}	Nozzle width of a single jet [m]
x	Cross-jet distance [m]
y	Downstream distance [m]
2D	Two-dimensional
BSL	Baseline $k-\omega$ Model
CFD	Computational Fluid Dynamics
FAC1.1	Factor of 1.1 of the observations
FAC1.5	Factor of 1.5 of the observations
GCI	Grid-convergence index
LES	Large Eddy Simulation
NMSE	Normalised mean squared error
PIV	Particle Image Velocimetry
PTIJ	Plane turbulent impinging jet
r	Linear grid refinement factor
R_p	Correlation coefficient
RANS	Reynolds-Averaged Navier-Stokes
RKE	Realizable $k-\epsilon$ Model
RNG	Re-Normalization Group $k-\epsilon$ Model
RSM	Linear Pressure-Strain Reynolds Stress Model
SKE	Standard $k-\epsilon$ Model
SOU	Second-order upwind
SST	Shear-Stress Transport $k-\omega$ Model
TKE	Turbulent kinetic energy

Chapter 1

Introduction

An air curtain is a plane turbulent impinging jet (PTIJ). A plane jet has a rectangular nozzle with a large aspect ratio, contrary to a circular jet which has a round nozzle. An impinging jet hits a wall somewhere downstream, opposed to a free jet that is not influenced by boundaries. Free jets are a well studied phenomena, and many of their characteristics are discovered by means of experiments (Pope, 2000). Impinging jets are often investigated in the interest of heat transfer or surface cleaning (Shuja et al., 1999; Beitelmal et al., 2006). However, in these applications, only small jet heights are used or solely the flow close to the impingement surface is studied. An air curtain is a PTIJ that is located on any side of a door frame. By creating a pressure drop, the air curtain forms an aerodynamic seal between the indoor and outdoor environments. The jets are strategically engineered to strike the floor with a particular velocity and position to reduce the heat and mass transfer through the doorway. The separation efficiency of an air curtain depends on a wide range of parameters. Environmental parameters, such as air temperature differences and pressure differences over the air curtain, as well as jet parameters, such as the jet Reynolds number, are of influence on the sealing efficiency.

In buildings, air curtains are widely used in entrance doors to restrict air infiltration and/or exfiltration. Cold air infiltration is one of the leading causes of energy loss in buildings and can account for up to 25% of the total heat losses in commercial buildings (Emmerich and Persily, 1998). Heat loss due to air infiltration becomes especially significant in public buildings, such as hospitals, supermarkets, offices, restaurants and stores, where the doors are frequently used. Air curtains can also be used to stop smoke spreading in a building in case of a fire (Krajewski, 2013). Furthermore, air curtains are used to preserve low temperatures in cold storage rooms and food display cabinets (Gonçalves et al., 2012a), to control dust in the mining industry (Colinet et al., 2006), and to maintain the air quality in the chemical and electronic industry, as well as in surgical units (Shih et al., 2011). In contrast to fast sliding doors, vestibules or plastic strip curtains, air curtains prevent outdoor air infiltration while also permitting an unobstructed entryway.

The optimisation of air-curtain devices is a relevant present-day topic. In a time where global warming is imminent, energy losses should be minimised. Furthermore, global pollution has a negative influence on air quality. Therefore, preserving and improving indoor air quality becomes more important. Air-curtain devices that make use of a single PTIJ are already in use for a long time, and their optimisation has been investigated by many. Gonçalves et al. (2012b) and Frank and Linden (2014) studied optimum discharge velocities. Costa et al. (2006), Shih et al. (2011) and Qi et al. (2018) discovered that the separation efficiency is enhanced by placing the

air curtain nozzle under an angle. They all found an optimum ejection angle of approximately 15°. Recirculating air curtains have also proven to optimise the separation efficiency (Hendrix et al., 1989; Gonçalves et al., 2012a). However, the complexity of the recirculation system and the installation and maintenance costs discourage its usage. Gonçalves et al. (2012a) compared vertical and horizontal air-curtain devices, and found that downward blowing air curtains present better sealing efficiency. Heated air curtains are studied by Frank and Linden (2015). They found that the effectiveness of an air curtain starts to decrease when it is heated beyond a critical temperature. Additionally, Qi et al. (2018) found that the presence of a person under the air curtain has little effect on its performance. Optimisation by means of parallel jets is not previously investigated. Double-stream twin-jet air curtains are used in the application of smoke and heat confinement (Elicer-Cortés et al., 2009). However, these devices do not optimise the separation efficiency, but operate as a confinement system.

Parallel jets start merging due to the intake of air across their boundaries, i.e. entrainment. Many have studied the merging behaviour of multiple parallel jets, especially the interaction of two parallel jets. Miller and Comings (1960) investigated the force-momentum fields of a single dual-jet configuration. Tanaka (1970) and Tanaka (1974) varied the distance between the nozzles and studied the effect on the resulting flow field, and compared their results with results from a single jet. They found that the velocity profiles of the combined flow are similar to those of the single jet, however, the turbulence intensities differ. Nasr and Lai (1997) were the first to use laser Doppler anemometry instead of hot-wire measurements to investigate the merging of two jets. They were able to give an elaborate analysis of the merging jets compared with a single jet, addressing jet characteristics such as pressure, mean velocity distributions, jet spreading, turbulence intensity distributions, and entrainment. Fujisawa et al. (2004) studied two parallel jets with different initial velocities and found that the jets develop toward the high velocity side. Although much is known about two parallel jets, three parallel jets, such as the ones in this research, are not often investigated.

The current study aims to optimise an air-curtain device by means of secondary jets, i.e. two jets with smaller nozzles that are placed at both sides of the main PTIJ. The secondary jets are expected to reduce the turbulence in the main jet. Therefore, stabilising the centreline velocity, and proving a better sealing. Two-dimensional (2D) Computational Fluid Dynamics (CFD) simulations are performed to gather information about velocity, entrainment and species transport across the jets. The distance between the jets and the discharge velocities are varied to find an optimal configuration. The effects of environmental parameters (e.g. pressure gradients) is beyond the scope of this study.

The report is organised as follows. Chapter 2 provides a theoretical background on the governing equations of fluid flow and their numerical approximations. Also, turbulence and turbulence modelling are discussed. Furthermore, the characteristics of a turbulent plane jet are illustrated, and a theoretical model is formulated. Chapter 3 describes a 2D numerical model of a PTIJ. A validation study is performed with the experimental data of Khayrullina et al. (2017), and the results are presented. Chapter 4 describes a 2D numerical model of a PTIJ with secondary jets. The simulation results of the numerical models from Chapter 3 and 4 are presented and discussed in Chapter 5. Recommendations for future work are presented in Chapter 6. Finally, the conclusions of this research are summarised in Chapter 7.

Chapter 2

Theoretical background

This chapter provides a theoretical background on the governing equations that describe fluid flow and species transport. A numerical approximation of these equations is given, which is used in Computational Fluid Dynamics (CFD). Turbulence is briefly described, and turbulence modelling in CFD is explained. Also, the characteristics of turbulent jets, such as entrainment, are described, and a theoretical model is defined for a 2D free plane jet.

2.1 Governing equations

The governing principles in fluid mechanics are the conservation laws for mass and momentum. The flow of an incompressible Newtonian fluid can be described by the continuity equation (conservation of mass)

$$\nabla \cdot \mathbf{u} = 0, \tag{2.1}$$

and the Navier-Stokes equations (conservation of momentum)

$$\rho \frac{\partial \mathbf{u}}{\partial t} + \rho(\mathbf{u} \cdot \nabla)\mathbf{u} = -\nabla P + \rho\nu\nabla^2\mathbf{u} + \rho\mathbf{g}. \tag{2.2}$$

Here, ρ is the (constant) fluid density, t the time, $\mathbf{u}$ the velocity vector, P the pressure, ν the kinematic viscosity of the fluid, and $\mathbf{g}$ the gravitational acceleration. Note, due to the constant density, body forces corresponding to gravity can be neglected (Kundu et al., 2016). Equations (2.1) and (2.2) are the differential forms of the conservation laws, and are often more appropriate for detailed analysis when field information is needed. When averaged or integrated quantities are sufficient, the integral forms can be used. Those are stated in terms of the evolution of a control volume, and the fluxes of mass and momentum that cross its control surface (Kundu et al., 2016). The integral form of the continuity equation (2.1) is given by

$$\iint (\mathbf{u} \cdot \mathbf{n})\, dA = 0, \tag{2.3}$$

where $\mathbf{n}$ is the normal (unit) vector, and A a control surface. Note that for the continuity equation (2.1) and (2.3), ρ is omitted because the flow is incompressible and isothermal, and therefore it is a constant. This makes that the continuity equation expresses conservation of volume rather than of mass. The integral form of the Navier-Stokes equation (2.2) is given by

$$\iiint \rho \frac{\partial \mathbf{u}}{\partial t}\, dV + \iint \rho \mathbf{u}(\mathbf{u}\cdot\mathbf{n})\, dA = -\iint P\mathbf{u}\, dA + \iiint \rho \mathbf{g}\, dV + \mathbf{F_v}. \tag{2.4}$$

Here, V is a control volume, and $\mathbf{F_v}$ describes the viscous forces. In the case of steady state, a uniform pressure field, and neglected viscous and gravitational effects, the Navier-Stokes equations reduce to

$$\iint \rho \mathbf{u}(\mathbf{u}\cdot\mathbf{n})\, dA = 0. \tag{2.5}$$

To visualise the trajectories of particles in a steady flow, the stream function for incompressible flows in two dimensions can be used. The stream function ψ satisfies

$$u = \frac{\partial \psi}{\partial y},\ v = -\frac{\partial \psi}{\partial x}, \tag{2.6}$$

where u and v describe the x-component and the y-component of the velocity, respectively (Kundu et al., 2016). Streamlines are represented by ψ = constant, and show the direction in which a fluid element will travel. In the case of a steady state, the streamlines coincide with the particle trajectories. By definition, there can be no flow normal to a streamline, meaning that there is conservation of mass between two streamlines. This implies that a high concentration of streamlines indicates a high velocity of the flow.

2.1.1 Species transport

The transport of a species is governed by the convection-diffusion equation:

$$\rho \frac{\partial c}{\partial t} + \rho \nabla \cdot (\mathbf{u}c) = \rho \nabla \cdot (D \nabla c) + S, \tag{2.7}$$

in which c is the species concentration, D the diffusivity coefficient, and S the sources and sinks of the species (Welty et al., 2009). Species transport is the net movement of species from one location to another, and is a result of convection and/or diffusion. Convection, also called advection when talking about species transport, is the passive transport by the carrying fluid, i.e. species are transported by the bulk motion of the fluid. Free convection occurs when there are density or temperature differences present in the fluid. Heavier fluid will sink, and lighter fluid will rise, causing a bulk fluid motion. Forced convection is the result of an external force setting the fluid in motion, such as a jet entering a quiescent fluid. In the present study, density differences are not considered (i.e. the flow is incompressible and isothermal), hence only forced convection is present.

Diffusion is mass transfer due to random motions of the fluid. In turbulent diffusion, the random motion of the fluid causes mixing, while in molecular diffusion it is the random motion of the molecules what is important. Thus, the degree of turbulent diffusion depends on the properties of the fluid flow, rather than on the properties of the molecules, as in molecular diffusion. Turbulent diffusion occurs much more rapidly than molecular diffusion. It greatly enhances mass transfer and is therefore extremely important for problems concerning mixing and transport. In equation (2.7), the second term on the left-hand side describes the convection of the species, the first term on the right-hand side describes diffusion of the species, and the second term on the right-hand side describes the creation or destruction of the species.

2.2 Turbulence

Turbulence is a fluid motion characterised by chaotic changes in pressure and flow velocity. Chaotic eddies, vortices and other flow instabilities of different sizes define turbulent flow. The onset of turbulence can be predicted by the dimensionless Reynolds number,

$$Re = \frac{VL}{\nu}, \tag{2.8}$$

where V is the velocity of the fluid, and L the characteristic length scale (Reynolds, 1895). The Reynolds number describes the balance between inertial forces and viscous forces. Inertial forces produce flow instabilities and viscous forces dampen them, so high values of Re indicate turbulence. For the case of a developed pipe flow, Reynolds (1895) suggested $Re \approx 2300$ for the upper limit of laminar flow. As the Reynolds number is increased, the transition from laminar to turbulent flow occurs over a range of Re depending on the details of the experiment (Pope, 2000). Although the Reynolds number gives an indication of the onset of turbulence, turbulence has resisted detailed physical analysis and therefore a unifying theory of turbulence does not yet exist (Cushman-Roisin, 2014).

2.3 Numerical approximation of the governing equations

The conservation principles for mass and momentum make it possible to predict fluid flow in all circumstances. Unfortunately, the equations are so complex that only analytical solutions for a few relatively simple cases can be found. Detailed solutions for complex flows were not possible until the development of computers, and the emergence of CFD. CFD is a technique that produces quantitative predictions of fluid-flow phenomena based on the conservation laws. With the help of digital computers, it allows for the prediction of the flow field by solving these equations numerically. In this study, the CFD solver ANSYS Fluent (ANSYS Inc., 2018) is used.

Computers work with discrete numbers, hence the continuous flow field must be approximated by discrete values and the partial differential equations must be replaced by discrete equations that relate the discrete values to each other (Kundu et al., 2016). The discretisation of equations can be done with different methods, such as the finite difference method, the finite volume method, and the finite element method. ANSYS Fluent uses the finite volume method which divides the continuum space in small control volumes. The integral forms of the conservation equations (equations (2.3) and (2.5)) are then applied to each control volume to find the average values of the 'unknowns', such as velocity and pressure. This automatically guarantees the conservation of fluxes through a particular control volume. In order to apply the finite volume method, the flow domain has to be discretised as well, which is done by means of a computational grid, carefully constructed according to appropriate guidelines (e.g., Franke et al. (2007)).

The discretised equations for conservation of mass and momentum, and the transport of species can be solved directly with CFD, which is called Direct Numerical Simulation (DNS). This method requires a very fine grid and very small time steps in order to capture all the scales of turbulence, and therefore, requires a long computational time. In many engineering applications, a complete description of turbulence is not needed and fast computation times are desired. Therefore, turbulence is often modelled instead of solved. Reynolds decomposition separates the variables (the velocity vector, $\mathbf{u}$, the pressure, P, and the concentration of species, c) into mean and fluctuating components:

$$\begin{aligned} \mathbf{u} &= \bar{\mathbf{u}} + \mathbf{u}', \\ P &= \bar{P} + P', \\ c &= \bar{c} + c', \end{aligned} \tag{2.9}$$

with the bar and the prime symbol indicating the mean and the fluctuating component, respectively. Substituting these decomposed variables into equations (2.1), (2.2) and (2.7), and taking the ensemble average, results in the unsteady Reynolds-Averaged Navier-Stokes (RANS) equations:

$$\frac{\partial \bar{u}_i}{\partial x_i} = 0, \tag{2.10}$$

$$\rho \frac{\partial \bar{u}_i}{\partial t} + \rho \bar{u}_i \frac{\partial \bar{u}_i}{\partial x_i} = -\nabla \bar{P} + \rho \nu \frac{\partial^2 \bar{u}_i}{\partial x_j^2} - \rho \frac{\partial \overline{u_i' u_j'}}{\partial x_j}, \tag{2.11}$$

$$\rho \frac{\partial \bar{c}}{\partial t} + \rho \frac{\partial \bar{c} \bar{u}_i}{\partial x_i} = \rho \frac{\partial}{\partial x_i} \left(D_{\bar{c}} \frac{\partial \bar{c}}{\partial x_i} \right) - \rho \frac{\partial \overline{c' u_i'}}{\partial x_i} + S_{\bar{c}}. \tag{2.12}$$

For convenience, the Einstein notation is used, i.e. $\mathbf{u} = u_i e^i$, with $i, j = 1, 2, 3$ in three dimensions, and $i, j = 1, 2$ in two dimensions. When the mean velocity field is not a function of time, the partial time derivative in equations (2.11) and (2.12) can be neglected, and the equations are referred to as the steady RANS equations. Equation (2.11) is similar to the Navier-Stokes equation of the instantaneous velocity field (equation (2.2)), except for the term $-\rho \partial \overline{u_i' u_j'} / \partial x_j$. This term describes the mean effect of the turbulent velocity fluctuations on the flow, and forms six additional unknowns (or three in two dimensions, i.e. $w' = 0$):

$$\overline{u'u'},\ \overline{v'v'},\ \overline{w'w'},\ \overline{u'v'},\ \overline{u'w'},\ \overline{v'w'}, \tag{2.13}$$

called the Reynolds or turbulent stresses. The same holds for equation (2.12) in which the term $-\rho \partial \overline{c' u_i'} / \partial x_i$ describes the turbulent diffusion fluxes, leading to three additional unknowns:

$$\overline{c'u'},\ \overline{c'v'},\ \overline{c'w'}. \tag{2.14}$$

Turbulence models attempt to close the RANS equations by modelling the Reynolds stresses and turbulent diffusion fluxes. First-order closure models make use of the Boussinesq eddy-viscosity hypothesis. This hypothesis relates the Reynolds stresses to the velocity gradients in the mean flow using a scalar called the turbulent or eddy viscosity, μ_t:

$$-\rho \overline{u_i' u_j'} = \mu_t \left(\frac{\partial u_i}{\partial x_j} + \frac{\partial u_j}{\partial x_i} \right) - \frac{2}{3} k \delta_{ij}, \tag{2.15}$$

with δ_{ij} the Kronecker delta, and k the turbulent kinetic energy defined as

$$k = \frac{1}{2} \overline{u_i' u_j'}. \tag{2.16}$$

The turbulent diffusion fluxes are related to mean concentration gradients according to the gradient-diffusion assumption (Pope, 2000):

$$-\rho\overline{c'u_i'} = D_t\frac{\partial \bar{c}}{\partial x_i}, \tag{2.17}$$

with D_t the turbulent diffusion coefficient defined as $D_t = \mu_t/Sc_t$, where Sc_t is the turbulent Schmidt number. Sc_t provides the ratio between the turbulent viscosity and the turbulent diffusion coefficient. In ANSYS Fluent, Sc_t has a default value of 0.7 (ANSYS Inc., 2018). A big limitation of the Boussinesq hypothesis is the inability to accurately model turbulence anisotropy (Wilcox, 2006). The scalar μ_t indicates isotropy which is mainly problematic in regions of high shear, where turbulence tends to be strongly anisotropic, resulting in an overestimation of turbulent production. This problem is solved when using second-order closure models, also called Reynolds Stress Models, which establish and solve additional transport equations for the Reynolds stresses and diffusion fluxes. However, these models comes with larger computational times and often experiences difficulties with numerical convergence.

2.3.1 Turbulence models

To gain a better understanding of the way that different turbulence models work, a brief description is given of all turbulence models used in this study, including their advantages and disadvantages. All models are RANS models. The $k-\epsilon$ and $k-\omega$ models are linear two-equation models which attempt to close the RANS equations using the turbulent viscosity. The linear pressure-strain Reynolds stress model is a Reynolds stress model, and thus solves additional transport equations for each of the Reynolds stresses.

Standard $k-\epsilon$ model (SKE)

The standard $k-\epsilon$ model solves the transport equations for the turbulent kinetic energy, k, and the turbulence dissipation, ϵ (Jones and Launder, 1972). The $k-\epsilon$ model assumes that the flow is fully turbulent, and the effects of molecular viscosity are negligible. Therefore, the standard $k-\epsilon$ model is only valid for fully turbulent flows (ANSYS Inc., 2018). The eddy viscosity is computed as $\mu_t = \rho C_\mu k^2/\epsilon$, with $C_\mu = 0.09$. The values of the other constants in the transport equations are determined from experiments for fundamental turbulent flows (ANSYS Inc., 2018). The SKE model is the most widely-used turbulence model for industrial applications, because it is robust, not memory-intensive, reasonably accurate and it offers good convergence. However, ϵ is not solved in the near-wall region, and therefore wall functions must always be used. The model also performs poorly for flows with strong separation, large streamline curvature and large pressure gradients (Wilcox, 2006).

Re-normalization group $k-\epsilon$ model (RNG)

The re-normalization group $k-\epsilon$ model is a modification of the SKE model. It uses similar transport equations, however, an extra term is added to the ϵ-equation that accounts for the mean flow distortion of turbulence dissipation, resulting in lower turbulence levels and a probability of underestimating k. The eddy viscosity is estimated with a differential equation, but in the high-Reynolds number limit it is given by $\mu_t = \rho C_\mu k^2/\epsilon$, with $C_\mu = 0.0845$. Note that C_μ has almost the same value as for the SKE model. However, it is derived analytically by a statistical technique called renormalization group theory, just as the other constants in the transport equations of the RNG model (ANSYS Inc., 2018). The model performs better than the SKE model for more complex shear flows, and flows with high strain rates, swirl and separation (Yakhot et al., 1992).

Realizable $k-\epsilon$ model (RKE)

The realizable $k-\epsilon$ model is another modification of the SKE model. It adopts a new model equation for ϵ and a new eddy-viscosity formula. Similar to the SKE model and RNG model, the eddy viscosity is computed from $\mu_t = \rho C_\mu k^2/\epsilon$, however, C_μ is no longer a constant. The model constants have been established to ensure that the model performs well for certain canonical flows (ANSYS Inc., 2018). The RKE model provides improved predictions for the spreading rate of both planar and round jets. The model also performs better for flows involving rotation, recirculation and streamline curvature (Shih et al., 1994).

Baseline $k-\omega$ model (BSL)

The baseline $k-\omega$ model is a modification of the standard $k-\omega$ model (SKW), which solves the transport equations for the turbulent kinetic energy, k, and the specific turbulence dissipation, ω (Menter, 1994). The SKW model is neglected in this study due to known convergence problems and issues with free stream flows. The most significant advantage of the $k-\omega$ models is that the equations are valid throughout the whole boundary layer, i.e. wall functions are not needed. The BSL model differs from the SKW model as it gradually changes from the SKW model in the inner region of the boundary layer to the SKE model in the outer part of the boundary layer, in order to take advantage out of the free-stream independence of the $k-\epsilon$ models.

Shear-stress transport $k-\omega$ model (SST)

The shear-stress transport $k-\omega$ model is a modification of the BSL model, and thus includes all its advantages. In addition, it accounts for the transport of the turbulence shear stress in the definition of the turbulent viscosity. As a result, the turbulent viscosity is no longer overpredicted as it was in the BSL model and separation and reattachment are predicted better (Menter, 1994).

Linear pressure-strain Reynolds stress model (RSM)

The Reynolds Stress Models give the most complete physical representation of turbulent flows. The models solve the Reynolds stresses directly using the RANS equations, avoiding the eddy-viscosity approximation that other models use (Launder, 1989). This means that three additional transport equations need to be solved in 2D. The linear pressure-strain Reynolds stress model is an ϵ-based Reynolds stress model, and thus the ϵ-equation has to be solved as well. Although the RSM model has greater potential to give accurate predictions for complex flows, the modelling of the pressure-strain terms is particularly challenging, and is often considered to be responsible for compromising the accuracy. Other disadvantages of the RSM model are the high computational cost due to the many equations that need to be solved, and the requirement of a high-quality mesh.

2.4 Turbulent plane jet

Experimental observations of turbulent jets have revealed many of their characteristics (Pope, 2000). In the axial direction of an impinging jet, such as an air curtain, the jet flow can be divided in three regions. The first region, the flow development region, contains the potential core, where the centreline mean velocity remains larger than or equal to 98% of the jet inlet velocity, V_0. In the second region, the fully developed flow region, turbulence has penetrated into the centreline of the jet and the potential core has dissipated. The third region is the

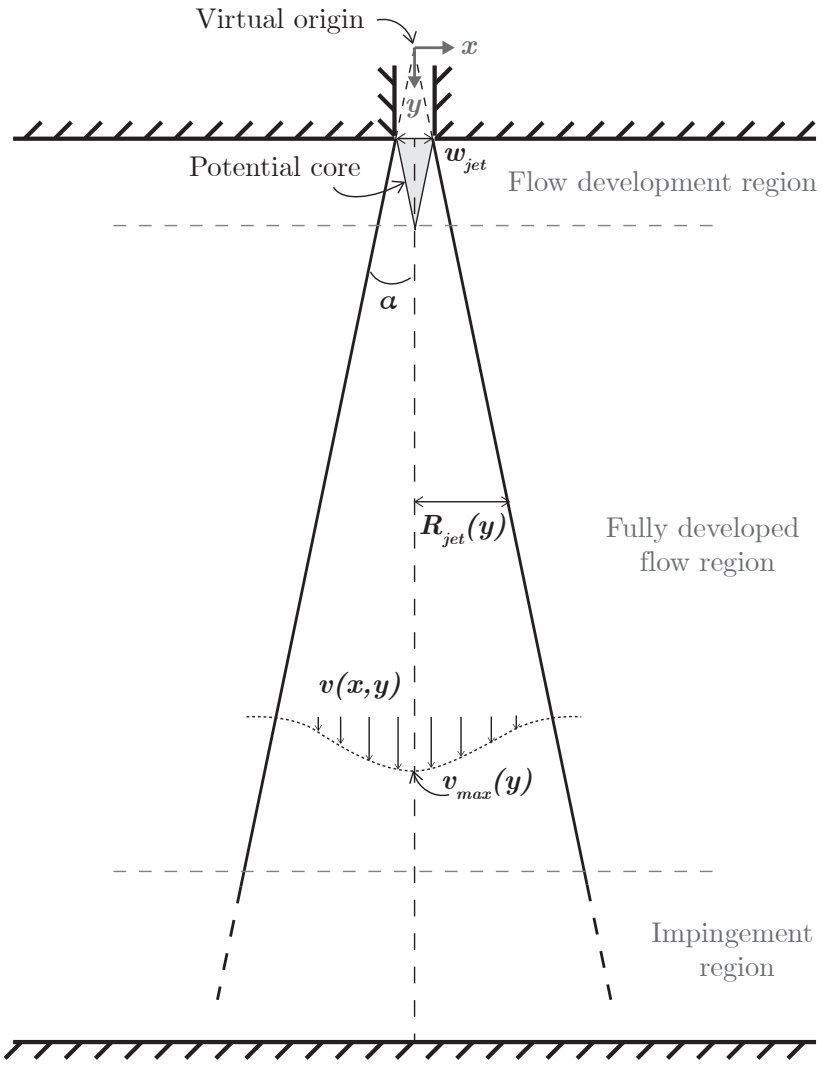

Figure 2.1: *Schematic description of an impinging jet.*

impingement region, in which the jet is influenced by the bottom wall. Figure 2.1 shows a schematic description of an impinging jet.

2.4.1 Velocity

In the fully developed flow region, the velocity profiles of all cross-sections show a nearly Gaussian shape (Pope, 2000; Turner, 1986). Therefore, the velocity profile in the y-direction can be described as

$$v(x, y) = v_{max} \exp\left(- \frac{x^2}{2\sigma^2} \right), \tag{2.18}$$

where v_{max} is the centreline velocity, and $\sigma(y)$ the standard deviation related to the spread of the velocity profile, also called the jet half width, $\delta_{0.5}$. A jet develops a nearly triangular shape (in the vertical plane) due to entrainment of fluid, caused by turbulence. The radius R_{jet} of the jet is thus proportional to the distance y downstream,

$$R_{jet}(y) = \alpha y. \tag{2.19}$$

The constant α depends on the opening angle of the jet. Experiments have shown that this angle is always approximately the same, $\alpha \approx 1/5$, for circular jets as well as for plane jets (Pope, 2000; Kotsovinos, 1976). For a Gaussian distribution, a width of 4σ accounts for 95% of the area under the Gaussian curve. Since $2R_{jet}$ is the diameter of the the jet, it can be stated that $4\sigma = 2R_{jet}$, i.e. $\sigma = \frac{1}{2}\alpha y$. The velocity profile can then be rewritten as

$$v(x, y) = v_{max} \exp\left(- \frac{2x^2}{\alpha^2 y^2} \right). \tag{2.20}$$

Note that the downstream distance y should be measured from the top of the triangle which is positioned above the nozzle in the so-called 'virtual origin' (see figure 2.1). The nozzle is then positioned at $y = R_{jet}/2\alpha$. The equation for the conservation of momentum (equation (2.5)) can be used to determine $v_{max}(y)$. Since momentum is described by mass and velocity, the only source of momentum is the jet itself. The surrounding fluid is initially at rest in the case of no external forcing and thus has no momentum. As a result, the momentum flux of the jet must remain constant downstream. By inserting equation (2.20) into the momentum balance, and treating the plane jet as a 2D problem, $v_{max}(y)$ is determined, with w_{jet} the nozzle width:

$$\int_{-\infty}^{+\infty} \rho v^2 \, dx = \rho V_0^2 w_{jet},$$

$$v_{max}(y) = V_0 \sqrt{\frac{2w_{jet}}{\sqrt{\pi}\alpha y}}. \tag{2.21}$$

2.4.2 Entrainment

In contrast to the momentum, the volume flux of the jet does not remain constant downstream due to entrainment of surrounding fluid. Entrainment can be described as the intake of fluid by the jet across its boundary. Most free turbulent flows, such as jets, depend for their energy supply on converting mean flow energy to turbulent energy by entrainment of non-turbulent ambient fluid (Townsend, 1970). When a fluid with a high velocity enters a quiescent fluid, as in the case of a jet, a shear flow is created at the boundaries due to the high velocity gradients. These shear flows are usually very unstable at high values of Re, when the viscosity of the fluid is not large enough to dampen out perturbations, resulting in vortices that transport fluid across the boundary of the jet, i.e. entrainment. To determine the volume flux Q as a function of the downstream distance y, the integral equation for conservation of mass (equation (2.3)) can be used, together with equations (2.20) and (2.21):

$$Q(y) = \int_{-\infty}^{+\infty} v \, dx, \tag{2.22}$$

$$Q(y) = V_0 w_{jet} \sqrt{\frac{\sqrt{\pi}\alpha y}{w_{jet}}}. \tag{2.23}$$

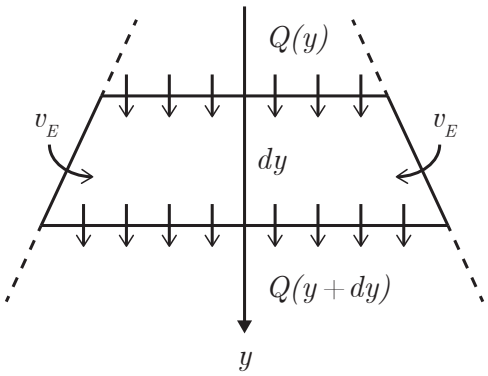

Figure 2.2: *Schematic description of the volume flux, $Q(y)$, and the entrainment velocity, v_E.*

The volume flux Q defines the total amount of fluid passing a cross-jet section at a certain y, per unit of time. The entrainment velocity, v_E, can then be defined by conservation of mass, as visualised in figure 2.2:

$$\mathrm{d}Q = v_E \mathrm{d}y, \tag{2.24}$$

$$v_E = \frac{\mathrm{d}Q}{\mathrm{d}y}, \tag{2.25}$$

resulting in

$$v_E = \frac{1}{2} V_0 \sqrt{\frac{\sqrt{\pi}\alpha w_{jet}}{y}}. \tag{2.26}$$

2.4.3 Comparison with a circular jet

In sections 2.4.1 and 2.4.2, the expressions for the jet radius, R_{jet}, the centreline velocity, v_{max}, the volume flux, Q, and the entrainment velocity, v_E, are derived for a 2D plane jet. Cushman-Roisin (2014) has derived these expressions for a three-dimensional circular jet, and they are compared in table 2.1.

Table 2.1: *Expressions for the jet radius, R_{jet}, the centreline velocity, v_{max}, the volume flux, Q, and the entrainment velocity, v_E, derived for a plane jet and a circular jet.*

	Plane jet		**Circular jet**	
R_{jet}	αy	[m]	αy	[m]
v_{max}	$V_0\sqrt{\frac{2w_{jet}}{\sqrt{\pi}\alpha y}}$	[m/s]	$\frac{V_0 w_{jet}}{\alpha y}$	[m/s]
Q	$V_0\sqrt{\sqrt{\pi} w_{jet}\alpha y}$	[m^2/s]	$\frac{1}{2}V_0 w_{jet}\pi\alpha y$	[m^3/s]
v_E	$\frac{1}{2}V_0\sqrt{\frac{\sqrt{\pi} w_{jet}\alpha}{y}}$	[m/s]	$\frac{V_0 w_{jet}}{4y}$	[m/s]

2.4.4 Multiple parallel jets

When two jets are placed next to each other, the fluid between the individual jets is rapidly removed due to the entrainment, causing the jets to be drawn towards each other and merge (Miller and Comings, 1960). As described earlier in this section, the flow field of a single jet can be divided into three regions. For multiple parallel jets, the first region, the flow development region, is divided into two additional regions; the converging region and the merging region (Nasr and Lai, 1997). The converging region includes the potential cores of the individual jets and recirculation zones, zones with sub-atmospheric static pressure, between the individual jets. This region ends at the merging points and the individual jets continue to merge until at the combined point where the horizontal velocity profile has only one maximum. Downstream from the combined point, the individual jets will unify to eventually resemble a single jet (Nasr and Lai, 1997). Figure 2.3 shows a schematic of the merging of three parallel jets, and indicates the merging points and the combined point.

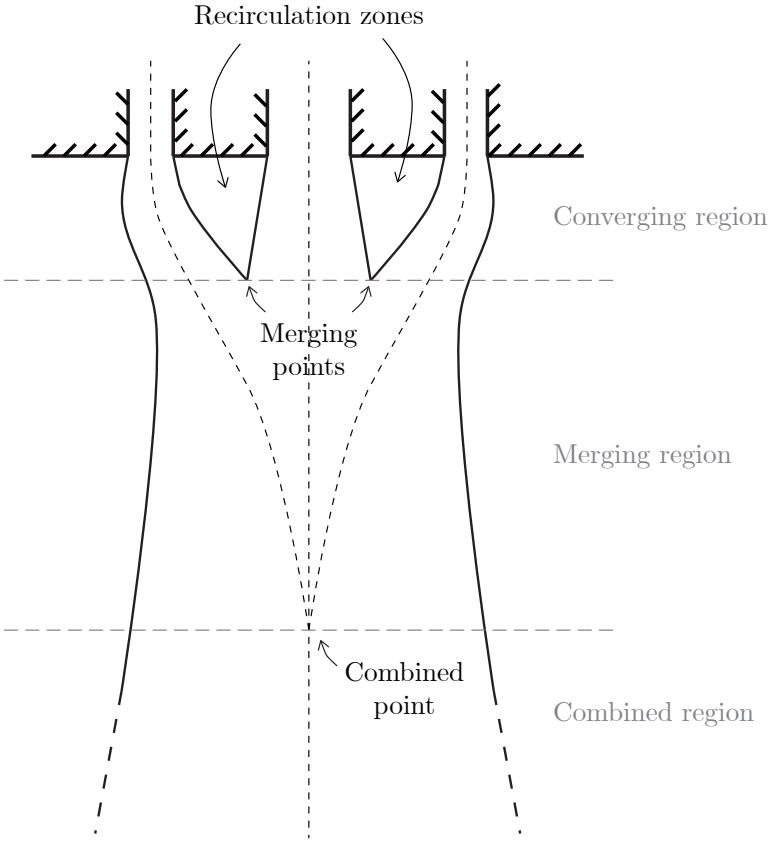

Figure 2.3: *Schematic description of three merging parallel jets.*

Chapter 3

Air curtain model with a single jet

2D CFD simulations are performed for an air curtain model with a single jet. The model geometry and boundary conditions are based on experiments performed by Khayrullina et al. (2017), and are described in section 3.1 and section 3.2, respectively. To ensure that the simulations do not depend on the computational grid, a grid-sensitivity analysis is performed in section 3.4, using four different grids and three different turbulence models. Finally, a validation study is performed with six turbulence models using the experimental data from Khayrullina et al. (2017). The results from the grid-sensitivity analysis and the validation study are used for the air curtain model with secondary jets, described in Chapter 4.

3.1 Computational geometry and grid

The computational model is a 2D replica of the experimental setup used by Khayrullina et al. (2017). In the experiments, a reduced-scale setup is used, which is filled with water. The computational model is 6.25 times larger with the proportions kept the same and filled with air, resembling a realistic environment for an air curtain. Figure 3.1 shows the geometry and its dimensions: the height of the domain, h_{jet} = 2.25 m, the width of the domain, w_{domain} = 12.5 m, the size of the pressure outlets, h_{outlet} = 31.25 mm, the nozzle width, w_{jet} = 50 mm, and the width of the velocity inlet (top of the contraction) of 562.5 mm. Note that these values are obtained by multiplying the dimensions of the experimental setup of Khayrullina et al. (2017)

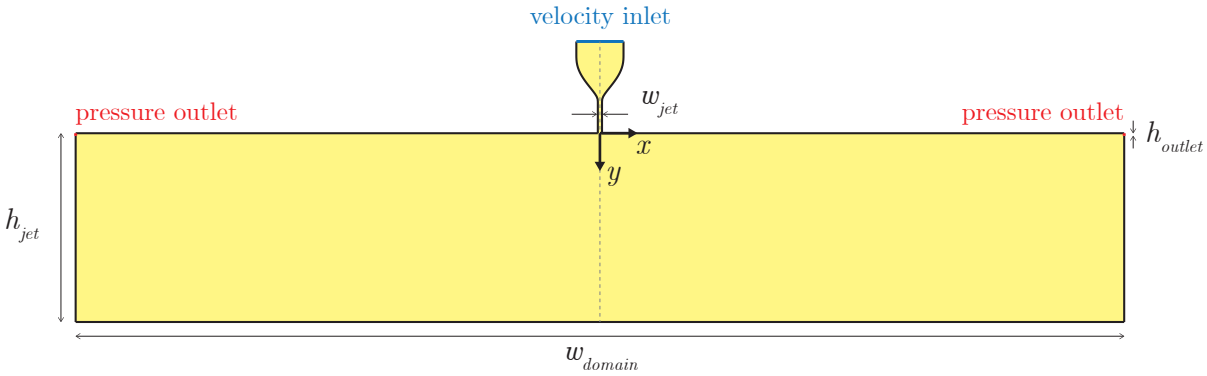

Figure 3.1: *Geometry of the 2D computational domain with indication of the coordinate system and the location of the pressure outlets and the velocity inlet. The dotted line indicates a symmetry line.*

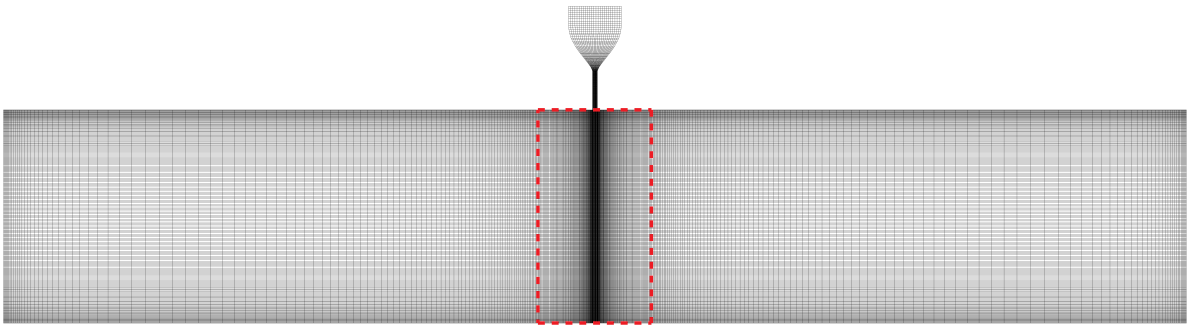

Figure 3.2: *Computational grid (fine) of the whole domain. The red dotted line indicates the region of interest.*

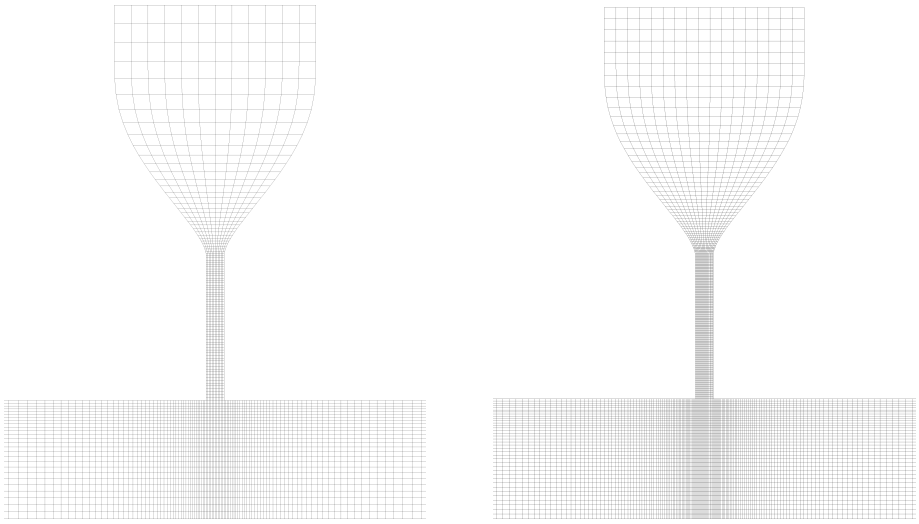

(a) *Coarse grid (23,300 cells).* **(b)** *Basic grid (48,188 cells).*

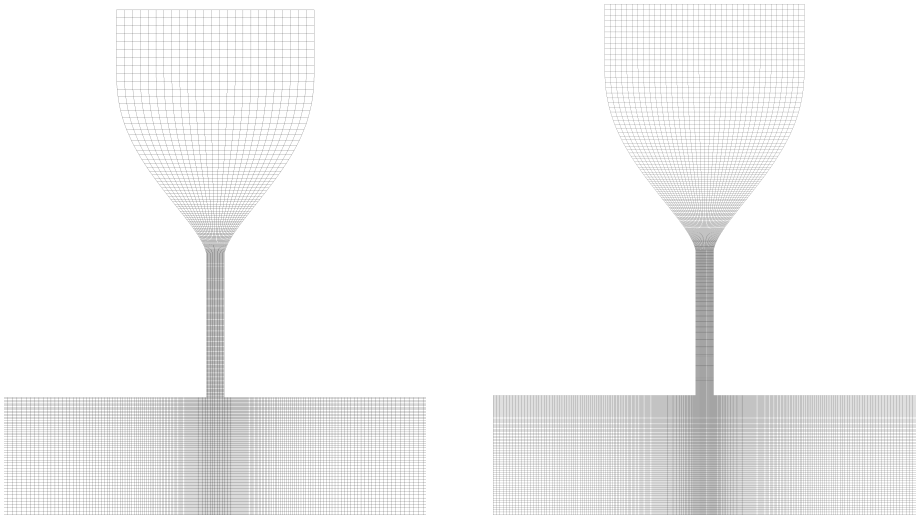

(c) *Fine grid (100,207 cells).* **(d)** *Finest grid (207,796 cells).*

Figure 3.3: *Grid refinement of the nozzle contraction and the upper part of the region of interest.*

with a factor 6.25. In the remainder of this report the y-coordinate is normalised with the domain height and will be referred to as y, i.e. $y' = y/h_{jet}$ and $y' \to y$. A fully structured grid is created with only quadrilateral cells (figure 3.2). In the region of interest, as indicated in figure 3.2, and in the nozzle contraction the resolution is increased. Four grids are constructed using a linear refinement factor of 1.44 in each direction. The total number of cells for each grid from coarse to finest is 23,300 cells (coarse), 48,188 cells (basic), 100,207 cells (fine), and 207,796 cells (finest), respectively. Franke et al. (2007) suggest to have at least 10 cells across an area of interest or an area with large gradients, therefore, 12 cells (coarse), 17 cells (basic), 25 cells (fine), and 36 cells (finest) are used across the nozzle contraction. Figure 3.3 shows the grid of the nozzle contraction and the upper part of the region of interest of the four grids.

3.2 Boundary conditions

The boundary conditions are chosen to replicate those of the experiments as closely as possible. All the surfaces, besides the velocity inlet and the pressure outlets, are smooth non-slip walls. A uniform velocity is imposed at the velocity inlet, see figure 3.1, which is based on the Reynolds number at the jet nozzle during the experiments. The desired jet discharge velocity, V_0^* is then given by

$$V_0^* = \frac{Re \cdot \nu}{w_{jet}}, \tag{3.1}$$

with $Re = 7200$, and ν the kinematic viscosity of air at 15 °C and 1 atm ($\nu = 1.461 \cdot 10^{-5}$ m^2/s (Cohen et al., 2003)). This results in $V_0^* = 2.104$ m/s at the jet nozzle. With mass conservation, the velocity at the velocity inlet was determined to be 0.187 m/s. In the remainder of this study, V_0 is used to denote the actual discharge velocity measured at the jet nozzle because it cannot be assumed that the turbulence models predict mass conservation in the exact same manner, i.e. $V_0^* \neq V_0$. For the velocity inlet, the turbulence parameters are specified based on the turbulence intensity ($I = 10\%$[1]) and the turbulence length scale

$$l = \frac{0.07L}{C_\mu^{3/4}}, \tag{3.2}$$

where L is the width of the gaps in the finest honeycomb in the contraction used in the PIV experiments ($L = 4.1$ mm), and C_μ a model constant with the value 0.09, resulting in a turbulence length scale of $l = 0.00175$ m. For the pressure outlets, the turbulence parameters are specified based on the turbulence intensity ($I = 10\%$) and the hydraulic diameter

$$D_H = \frac{2ab}{a+b} \approx 2a \quad \text{when} \quad b \gg a, \tag{3.3}$$

with $a = h_{outlet}$, and b the depth of the domain, resulting in a hydraulic diameter of $D_H = 0.0625$ m. Zero static gauge pressure is enforced at the outlets.

3.3 Solver settings

The 2D steady RANS equations are solved with ANSYS Fluent 17.2 (2016) and 19.0 (2018). To provide closure, six different turbulence models are used, which are described in section 2.3.1:

[1] Guyonnaud et al. (2000) found that, in the range of 0 – 20%, the turbulence intensity does not affect the air curtain performances.

1) SKE; 2) RNG; 3) RKE; 4) BSL; 5) SST; and 6) RSM. For the near-wall regions, scalable wall functions (ANSYS Inc., 2018) are used to avoid the deterioration of standard wall functions (Launder and Spalding, 1974) under grid refinement. Pressure-velocity coupling is performed by the SIMPLE (Semi-Implicit Method for Pressure-Linked Equations) algorithm. Pressure interpolation is second order for all turbulence models except RSM, where the pressure interpolation is taken standard in order to get convergence. Second-order upwind (SOU) discretisation schemes are used for both the convection terms and the viscous terms of the governing equations for all models. Convergence is monitored through scaled residuals and through analysing the velocity magnitude at reference points. It was made sure that all scaled residuals levelled out below four orders of magnitude (Franke et al., 2007) or dropped below twelve orders of magnitude (double-precision). At the same time, constant values of the velocity magnitude were observed at six reference points in the region of interest.

3.4 Grid-sensitivity analysis

A grid-sensitivity analysis is conducted to obtain (nearly) grid-independent results. The four grids described in section 3.1 are analysed. The grids are compared based on the dimensionless mean velocity magnitude, $|V|/V_0$, and the dimensionless turbulent kinetic energy (TKE), k/V_0^2, along the jet centreline and three cross-jet lines located at $y = 0.2$, $y = 0.5$ and $y = 0.8$ in the region of interest (see figure 3.2). Figure 3.4 shows the position of the four lines in the domain. The grid-sensitivity analysis is done using the SKE model. Figure 3.5, 3.6 and 3.7 show the dimensionless mean velocity magnitude and the dimensionless TKE along the four lines for the different grids. The figures show that for all positions the results of the different grids are almost identical, except for the centreline TKE (see figure 3.6b).

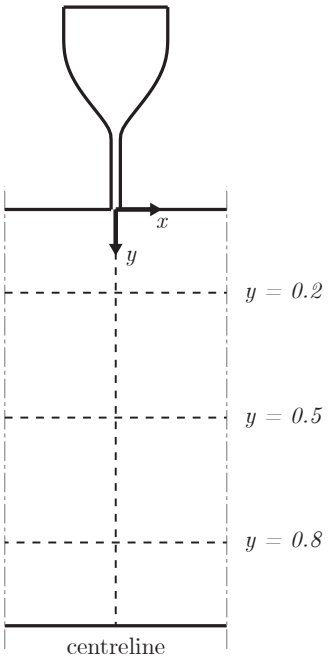

Figure 3.4: *Indication of the lines along which experimentally and numerically obtained values for the velocity and TKE are compared: centreline, $y = 0.2$, $y = 0.5$ and $y = 0.8$.*

To quantify the grid-sensitivity results, the grid-convergence index (GCI) by Roache (1994) is used. The GCI indicates how much the solution would change with a further refinement of the grid. For the fine grid it is defined as

$$GCI_{fine} = F_s \left| \frac{r^p (f_{fine} - f_{finest})}{1 - r^p} \right|, \tag{3.4}$$

with F_s a safety factor, taken to be 1.25, the recommended value when three or more grids are considered in the grid-sensitivity analysis (Roache, 1994), r the linear grid refinement factor ($r = 1.44$), p the order of accuracy of the numerical scheme, and f_{fine} and f_{finest} the solutions obtained with the fine grid and the finest grid, respectively, which correspond to $|V|/V_0$ or k/V_0^2. According to Celik et al. (2008), the observed order of accuracy, p, should be calculated as follows to get a more accurate GCI:

$$p = \ln \left(\frac{f_{basic} - f_{fine}}{f_{fine} - f_{finest}} \right) / \ln r. \tag{3.5}$$

However, non-monotonic convergence is present, resulting in negative values for $(f_{basic} - f_{fine})/(f_{fine} - f_{finest})$, which restrict the calculation of p. Therefore, the formal order of accuracy, $p = 2$, is used due to the second-order discretisation schemes that are used for the simulations.

For the calculation of the GCI, the coarse grid is neglected due to the deviations of the results from the results of the finest grid, visible in figure 3.6. The average and maximum values of the GCI for the fine grid and the basic grid, respectively, are presented in table 3.1 and 3.2. To get a better impression of these values, the GCI calculated for the fine grid is plotted in figure 3.8 and 3.9. To see the influence of the used turbulence model on the grid-sensitivity, a grid-sensitivity analysis is performed with the RNG model and the BSL model as well for the basic, fine and finest grid. The results are plotted in figure 3.10, 3.11, 3.12 and 3.13. Additionally, the average and maximum values are presented in table 3.1 and 3.2.

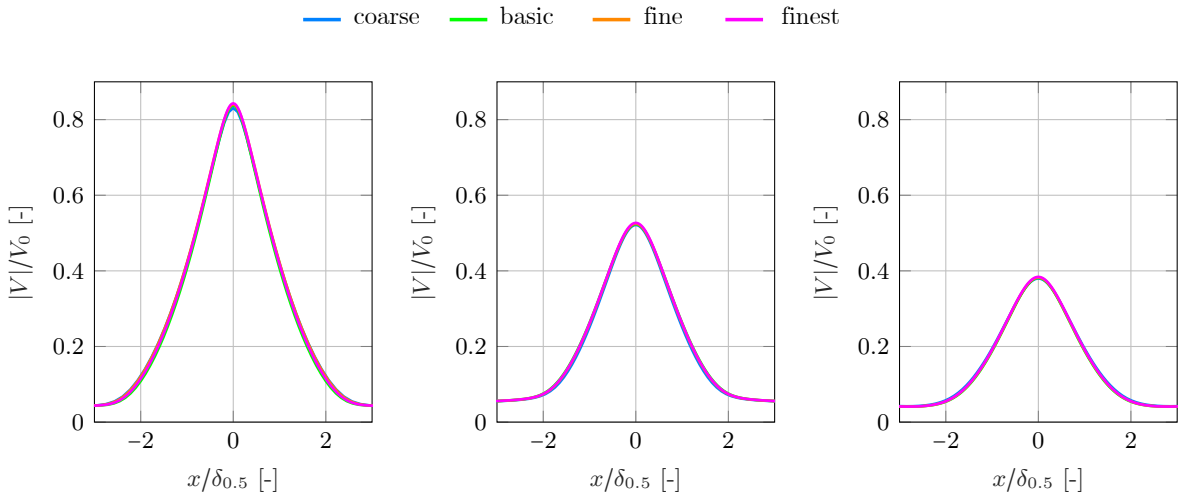

(a) $y = 0.2$. **(b)** $y = 0.5$. **(c)** $y = 0.8$.

Figure 3.5: *Comparison of dimensionless mean velocity magnitude, $|V|/V_0$ along three cross-jet lines at $y = 0.2$, $y = 0.5$ and $y = 0.8$, obtained with steady RANS CFD on four different grids.*

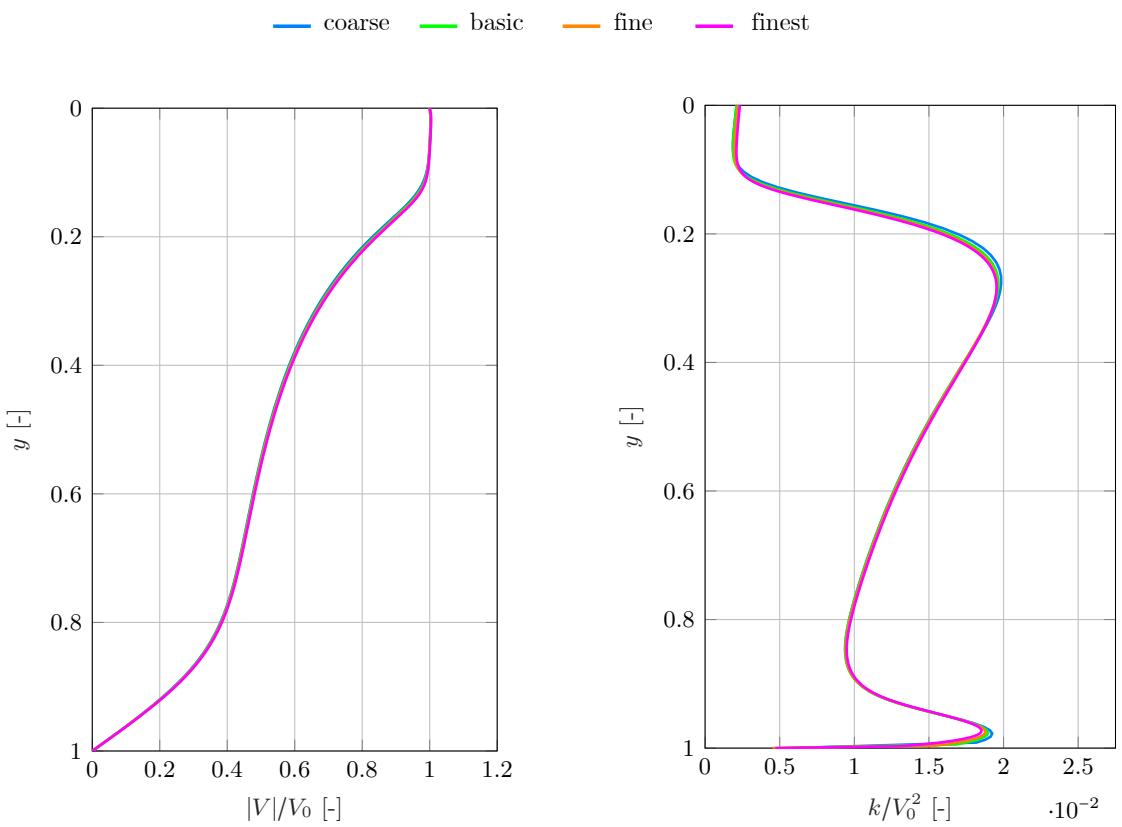

(a) *Dimensionless mean velocity magnitude.* **(b)** *Dimensionless TKE.*

Figure 3.6: *Comparison of dimensionless mean velocity magnitude, $|V|/V_0$, and dimensionless TKE, k/V_0^2, along the centreline obtained with steady RANS CFD on four different grids.*

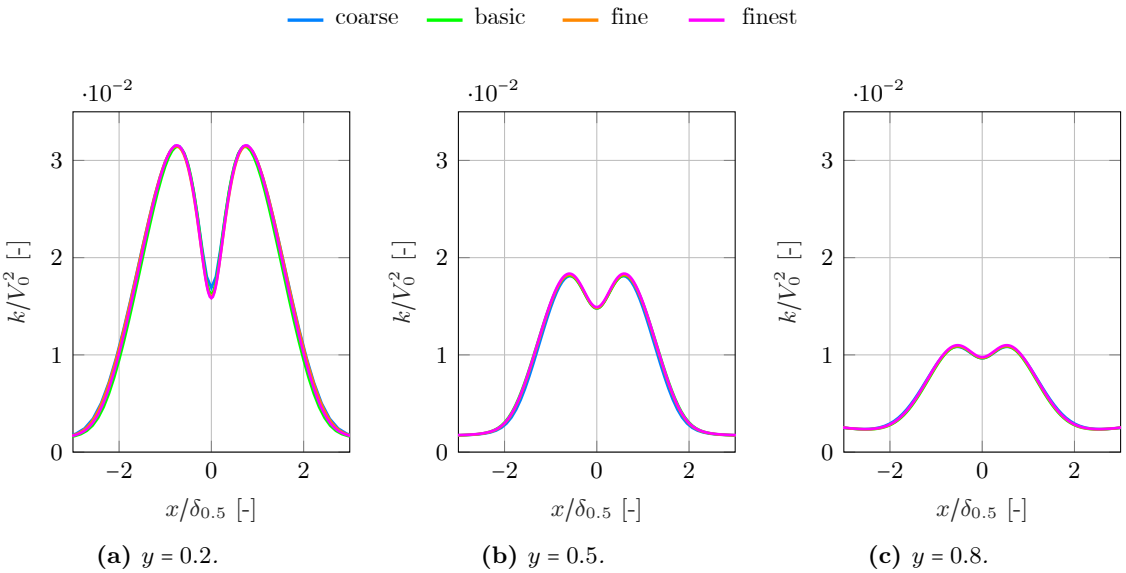

(a) $y = 0.2$. **(b)** $y = 0.5$. **(c)** $y = 0.8$.

Figure 3.7: *Comparison of dimensionless TKE, k/V_0^2 along three cross-jet lines at $y = 0.2$, $y = 0.5$ and $y = 0.8$, obtained with steady RANS CFD on four different grids.*

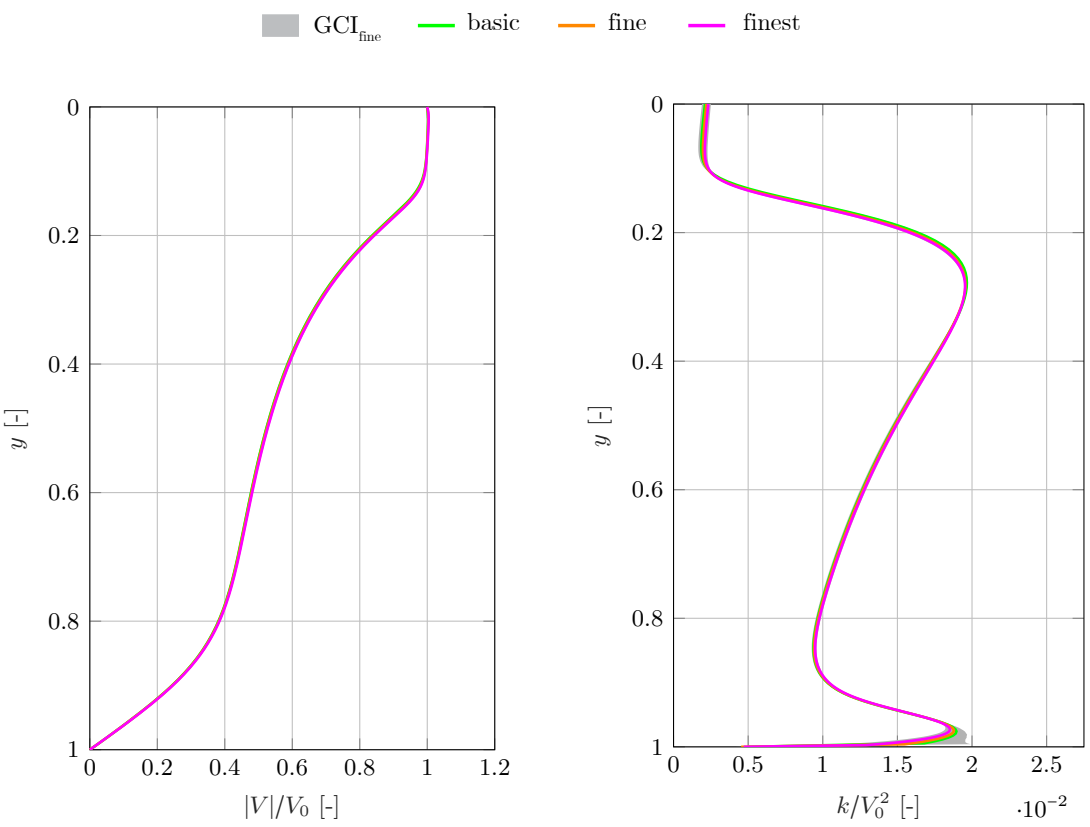

(a) *Dimensionless mean velocity magnitude.* **(b)** *Dimensionless TKE.*

Figure 3.8: *Band of GCI_{fine} for $|V|/V_0$ and k/V_0^2 along the centreline, obtained with the SKE model.*

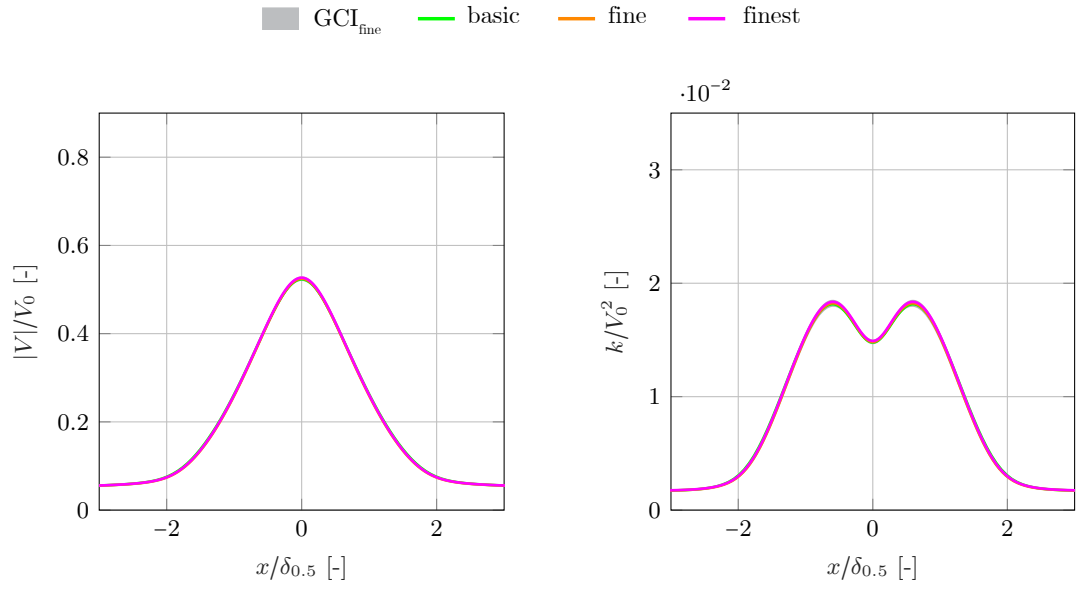

(a) *Dimensionless mean velocity magnitude.* **(b)** *Dimensionless TKE.*

Figure 3.9: *Band of GCI_{fine} for $|V|/V_0$ and k/V_0^2 along a cross-jet line at $y = 0.5$, obtained with the SKE model.*

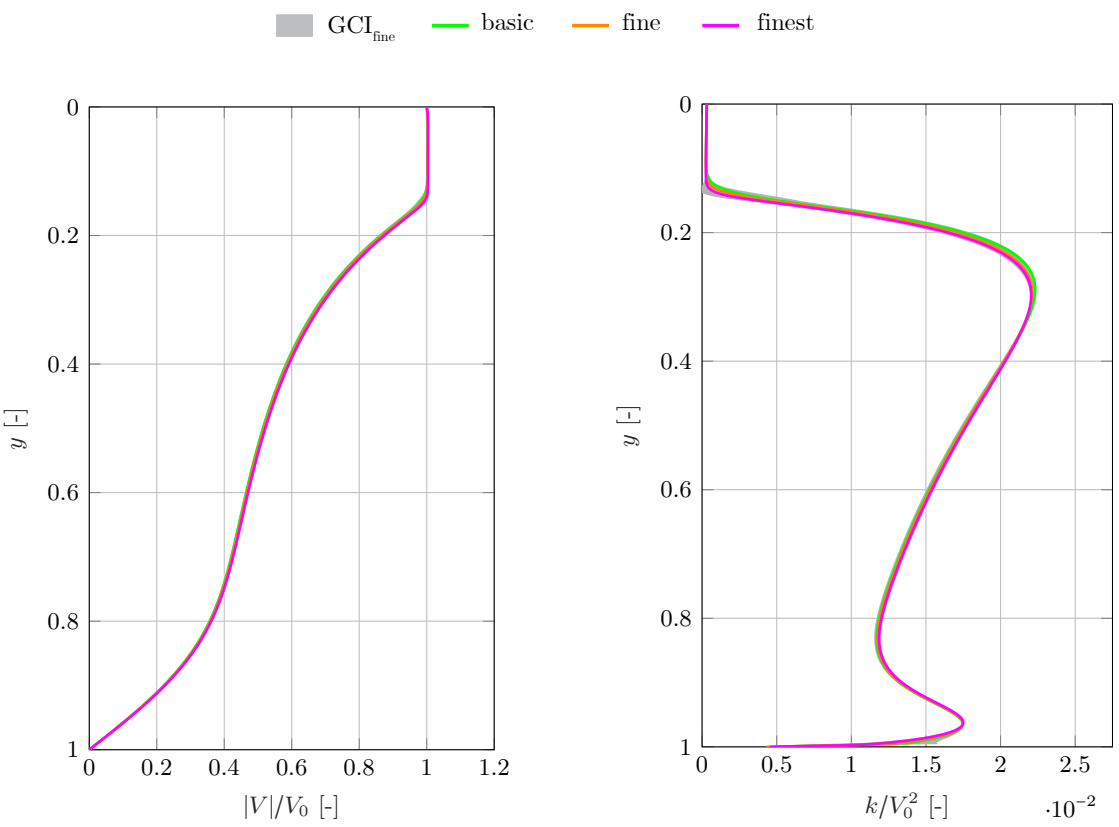

(a) *Dimensionless mean velocity magnitude.* **(b)** *Dimensionless TKE.*

Figure 3.10: *Band of GCI_{fine} for $|V|/V_0$ and k/V_0^2 along the centreline, obtained with the RNG model.*

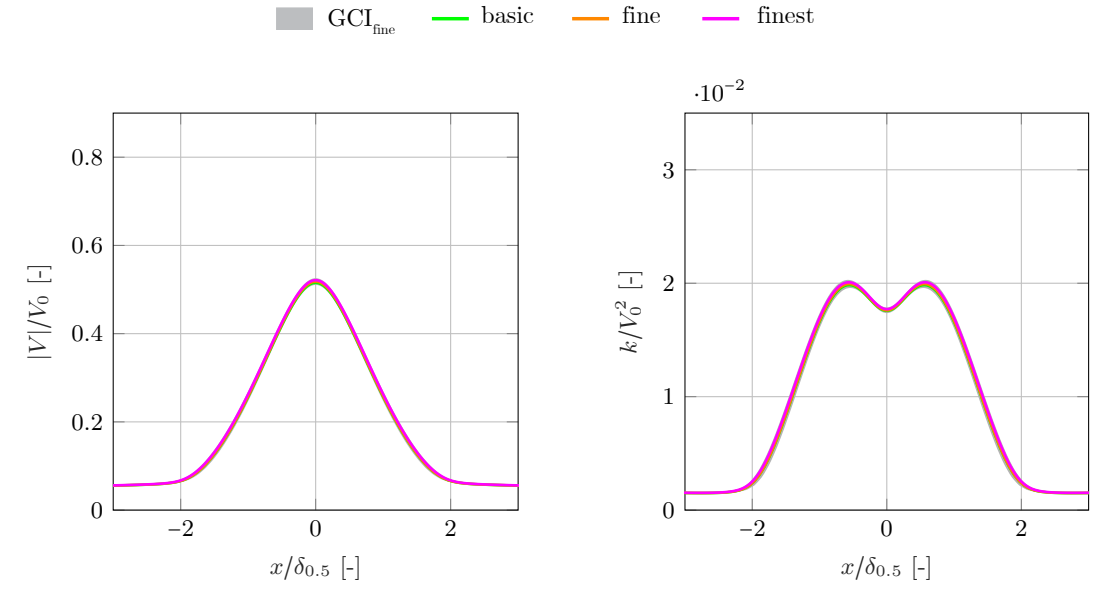

(a) *Dimensionless mean velocity magnitude.* **(b)** *Dimensionless TKE.*

Figure 3.11: *Band of GCI_{fine} for $|V|/V_0$ and k/V_0^2 along a cross-jet line at $y = 0.5$, obtained with the RNG model.*

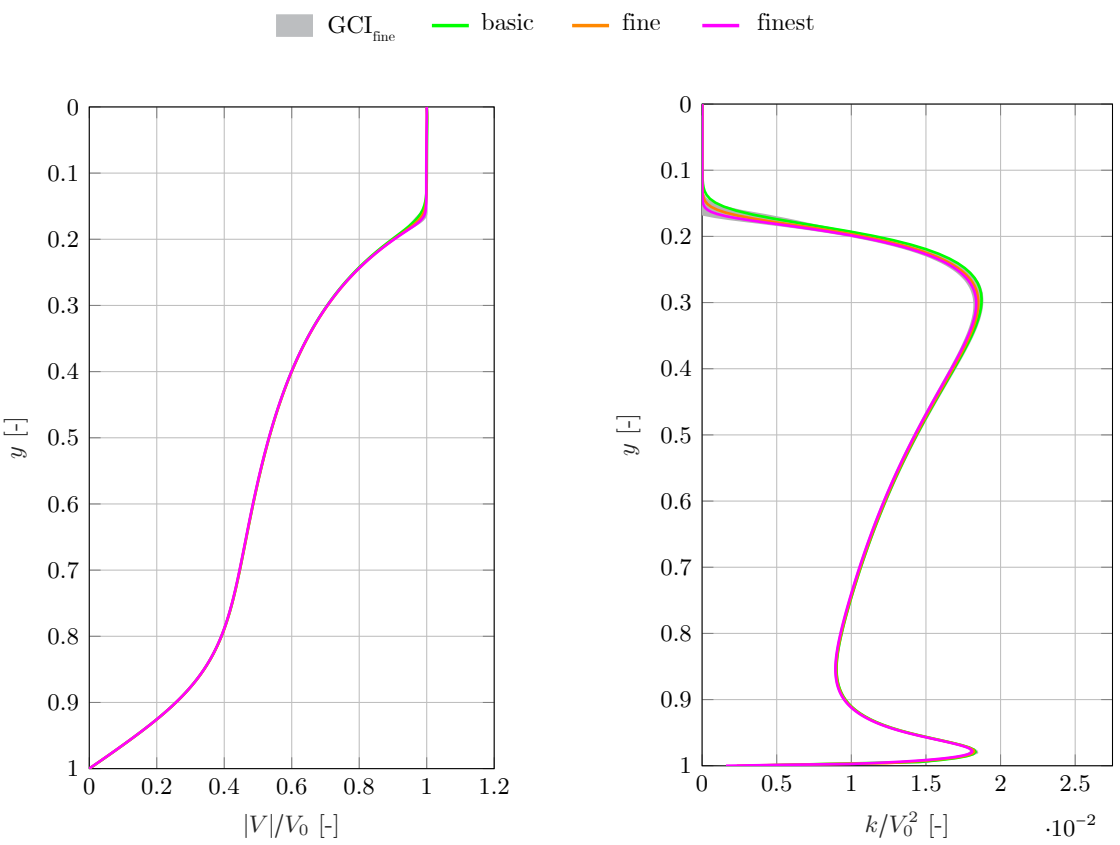

(a) *Dimensionless mean velocity magnitude.* **(b)** *Dimensionless TKE.*

Figure 3.12: *Band of GCI_{fine} for $|V|/V_0$ and k/V_0^2 along the centreline, obtained with the BSL model.*

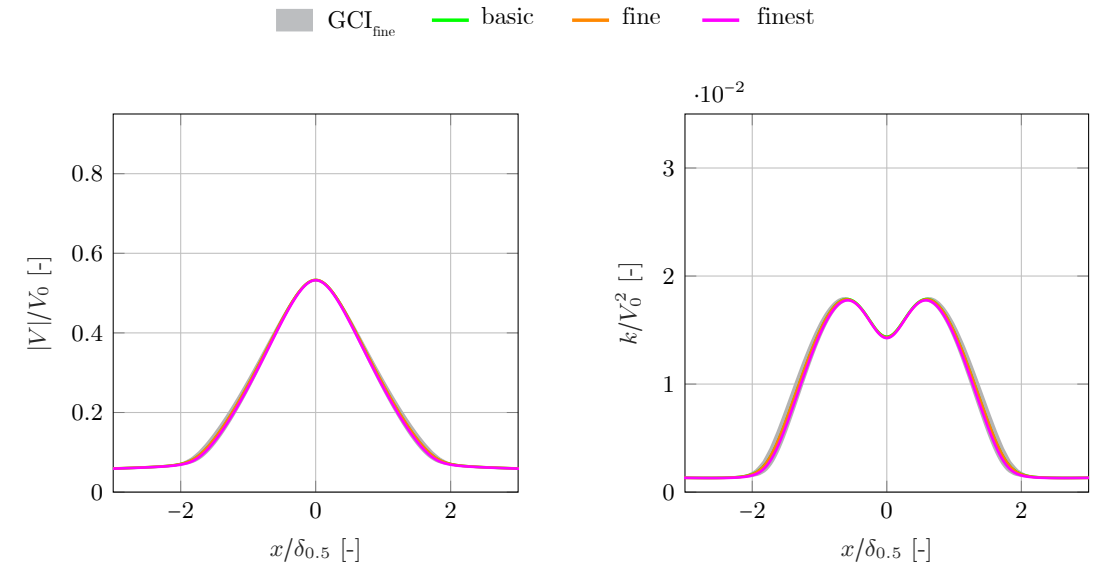

(a) *Dimensionless mean velocity magnitude.* **(b)** *Dimensionless TKE.*

Figure 3.13: *Band of GCI_{fine} for $|V|/V_0$ and k/V_0^2 along a cross-jet line at $y = 0.5$, obtained with the BSL model.*

Table 3.1: *Maximum and average GCI values for $|V|/V_0$ and k/V_0^2 for the fine grid along the centreline and along a cross-jet line at $y = 0.5$.*

GCI [%]	SKE		RNG		BSL	
	max.	avg.	max.	avg.	max.	avg.
centreline velocity	6.8%	1.0%	15.4%	1.4%	23.4%	0.6%
velocity at $y = 0.5$	2.4%	1.4%	8.0%	3.1%	13.3%	3.8%
centreline TKE	28.3%	4.7%	112.0%	5.9%	197.3%	10.6%
TKE at $y = 0.5$	4.5%	2.4%	16.0%	3.9%	28.9%	4.8%

Table 3.2: *Maximum and average GCI values for $|V|/V_0$ and k/V_0^2 for the basic grid along the centreline and along a cross-jet line at $y = 0.5$.*

GCI [%]	SKE		RNG		BSL	
	max.	avg.	max.	avg.	max.	avg.
centreline velocity	8.6%	0.7%	6.4%	1.1%	11.7%	0.4%
velocity at $y = 0.5$	6.7%	1.9%	1.3%	0.9%	1.6%	0.6%
centreline TKE	34.3%	4.3%	90.2%	5.5%	197.8%	15.3%
TKE at $y = 0.5$	10.2%	2.4%	2.0%	1.1%	3.5%	0.8%

The GCI values for the fine grid are presented in table 3.1. For all models, the centreline TKE is most influenced by the grid refinement, which is also visible in figure 3.6b. The large maximum values are due to the large gradients around $y = 0.2$ and close to $y = 1$. The SKE model only shows large GCI values near $y = 1$, and similar values have been found near $y = 1$ for the RNG model and the BSL model. However, the extremely high maximum values, 112% and 197%, for the RNG model and the BSL model, respectively, have been found around $y = 0.2$ (see figure 3.10b and 3.12b). Between $y = 0$ and $y = 0.1$, the average GCI values for the TKE for the RNG model and the BSL model are extremely small ($\sim 1\%$), in contrast to the SKE model ($\sim 15\%$).

The GCI values for the basic grid are displayed in table 3.2. Similar trends can be observed for basic grid compared to the fine grid. Again, the centreline TKE gives the largest GCI values, and the maximum values are found at similar y positions. Comparing table 3.1 and 3.2, not many differences can be found, and the fine grid does not seem to perform better than the basic grid. Nevertheless, it is decided to use the fine grid in the remainder of this study in order to get the best possible results. Note that the results from the SKE model seem to be least influenced by the grid-refinement compared to the results from the RNG model and the BSL model, which can be deduced from the lower GCI values for the SKE model.

3.5 Validation

To determine which turbulence model is most suitable for this study, a validation study is carried out. The outcome of six turbulence models, described in section 2.3.1, is compared with the results of PIV experiments conducted by Khayrullina et al. (2017). From the grid-sensitivity analysis in section 3.4 it is concluded that the fine grid gives the best results. Thus, the validation study is done with the fine grid. Again, the velocity magnitude and TKE are

compared along the four lines depicted in figure 3.4. Figure 3.15, 3.14 and 3.16 show the PIV data compared to the results from the CFD simulations with the six different turbulence models. To quantify the performance of the different turbulence models, the outcomes are compared to the experimentally obtained values of $|V|/V_0$ or k/V_0^2. Four validation metrics are used; the factor of 1.1 of the observations (FAC1.1), the factor of 1.5 of the observations (FAC1.5), the normalised mean squared error (NMSE), and the correlation coefficient (R_p), which are calculated using equation (3.6), equation (3.7), equation (3.8) and equation (3.9), respectively:

$$\text{FAC1.1} = \frac{1}{N}\sum_{i=1}^{N} n_i \quad \text{with} \quad n_i = \left\{ \begin{array}{ll} 1 & \text{for} \quad 0.91 \leq \dfrac{P_i}{O_i} \leq 1.1 \\ 0 & \text{else} \end{array} \right\}, \tag{3.6}$$

$$\text{FAC1.5} = \frac{1}{N}\sum_{i=1}^{N} n_i \quad \text{with} \quad n_i = \left\{ \begin{array}{ll} 1 & \text{for} \quad 0.67 \leq \dfrac{P_i}{O_i} \leq 1.5 \\ 0 & \text{else} \end{array} \right\}, \tag{3.7}$$

$$\text{NMSE} = \frac{[(O_i - P_i)^2]}{[O_i P_i]}, \tag{3.8}$$

$$R_p = \frac{[(O_i - [O])(P_i - [P])]}{\sigma_O \sigma_P}, \tag{3.9}$$

with P_i and O_i the time-averaged values obtained from CFD simulations and PIV experiments, respectively, N the number of data points, and σ_P and σ_O the standard deviations of P_i and O_i, respectively. The square brackets indicate averaging over all data points. The optimal score for FAC1.1, FAC1.5 and R_p is 1 and the optimal score for NMSE is 0. The four validation metrics are calculated along four lines (centreline, $y = 0.2$, $y = 0.5$, $y = 0.8$) for both the velocity and the TKE. The average values for the velocity and the TKE are stated in table 3.3 and table 3.4, respectively. Table 3.5 and 3.6 show the values along the centreline for the velocity and the TKE, respectively. In Appendix A, the complete tables can be found.

For the velocity (see table 3.3), the BSL and RKE models perform best and the RSM model performs worst. Especially FAC1.1 and NMSE reflect this. However, the other models, SKE, RNG and SST, perform very good as well. Based on R_p, all models perform equally good. For the turbulent kinetic energy, the SKE and RNG models perform significantly better than the other models. According to R_p, the SKE model performs best, but based on FAC1.1 and NMSE, the RNG model performs just slightly better. Along the centreline, the SKE model clearly performs best for the velocity (see table 3.5) as well as for the TKE (see table 3.6).

Table 3.3: *Values of the validation metrics defined for the dimensionless mean velocity magnitude averaged over the centreline and three cross-jet lines at $y = 0.2$, $y = 0.5$ and $y = 0.8$.*

$\|V\|/V_0$	**SKE**	**RNG**	**RKE**	**BSL**	**SST**	**RSM**
FAC1.1	0.673	0.460	0.734	0.775	0.617	0.208
NMSE	0.007	0.009	0.004	0.004	0.005	0.021
$\mathbf{R_p}$	0.990	0.990	0.989	0.989	0.988	0.988

Table 3.4: *Values of the validation metrics defined for the dimensionless TKE averaged over the centreline and three cross-jet lines at $y = 0.2$, $y = 0.5$ and $y = 0.8$.*

k/V_0^2	**SKE**	**RNG**	**RKE**	**BSL**	**SST**	**RSM**
FAC1.5	0.853	0.886	0.807	0.839	0.766	0.739
NMSE	0.087	0.075	0.146	0.105	0.143	0.095
$\mathbf{R}_\mathrm{p}$	0.952	0.936	0.894	0.915	0.931	0.917

Table 3.5: *Validation metrics defined for the dimensionless mean velocity magnitude along the centreline.*

$\lvert V\rvert/V_0$ (centreline)	**SKE**	**RNG**	**RKE**	**BSL**	**SST**	**RSM**
FAC1.1	0.922	0.722	0.756	0.861	0.800	0.278
NMSE	0.006	0.008	0.008	0.007	0.007	0.016
$\mathbf{R}_\mathrm{p}$	0.980	0.979	0.981	0.979	0.978	0.973

Table 3.6: *Validation metrics defined for the dimensionless TKE along the centreline.*

k/V_0^2 (centreline)	**SKE**	**RNG**	**RKE**	**BSL**	**SST**	**RSM**
FAC1.5	0.929	0.880	0.782	0.880	0.803	0.820
NMSE	0.056	0.045	0.180	0.045	0.164	0.097
$\mathbf{R}_\mathrm{p}$	0.849	0.810	0.633	0.713	0.786	0.750

Besides the validation metrics that are used to quantify the performance of the turbulence models, also the jet potential core, h_p, and the jet half width, $\delta_{0.5}$, obtained from the CFD simulations, are compared with the results from the PIV measurements to quantify the performance. The jet potential core is defined as the distance from the jet nozzle where the centreline mean velocity remains more than or equal to 98% of the inlet mean jet velocity, i.e. $|V|/V_0 \geq 0.98$. Table 3.7 shows the dimensionless jet potential core length, h_p/w_{jet}, and the difference relative to the PIV data. The jet half width is defined as the horizontal distance between the jet centreline and the point, where the mean velocity is equal to half the mean centreline velocity at a certain downstream position. Table 3.8 shows the dimensionless jet half width, $\delta_{0.5}/w_{jet}$, and the difference relative to the PIV data, at three different downstream positions ($y = 0.2$, $y = 0.5$, $y = 0.8$). The SKE model is the only model that underpredicts the length of the potential core, but does predict the length of the potential core best. The RNG model gives the smallest overprediction. The SKE model and the RNG model significantly overpredict the jet half width at $y = 0.2$, but this overprediction decreases when moving downstream, especially for the SKE model. Considering the jet half width, the BSL model and the SST model perform best.

Table 3.7: *Dimensionless length of the jet potential core, h_p/w_{jet}, obtained with six different turbulence models, compared to the PIV result.*

	h_p/w_{jet}	% difference
PIV	5.96	
SKE	5.49	−7.8%
RNG	6.82	+14.3%
RKE	7.84	+31.5%
BSL	7.54	+26.4%
SST	7.60	+27.4%
RSM	7.27	+21.9%

Table 3.8: *Dimensionless jet half width, $\delta_{0.5}/w_{jet}$, obtained with six different turbulence models, compared to the PIV results.*

	y = 0.2		y = 0.5		y = 0.8	
	$\delta_{0.5}/w_{jet}$	% difference	$\delta_{0.5}/w_{jet}$	% difference	$\delta_{0.5}/w_{jet}$	% difference
PIV	0.65		2.12		3.91	
SKE	0.84	+28.2%	2.25	+6.2%	3.89	−0.7%
RNG	0.79	+21.1%	2.33	+9.8%	4.34	+10.9%
RKE	0.70	+7.9%	2.03	−4.1%	3.57	−8.8%
BSL	0.70	+7.9%	2.10	−0.8%	3.67	−6.1%
SST	0.70	+7.9%	2.18	+2.7%	3.67	−6.1%
RSM	0.70	+7.9%	2.33	+9.8%	4.46	+14.0%

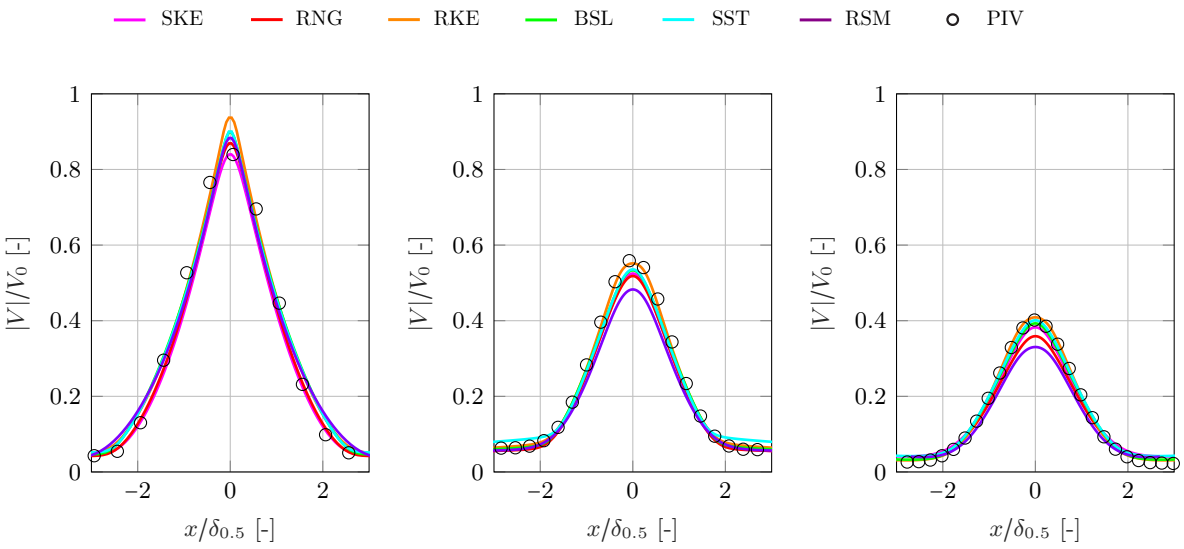

(a) y = 0.2. **(b)** y = 0.5. **(c)** y = 0.8.

Figure 3.14: *Comparison of PIV results with results of steady RANS CFD simulations of the dimensionless mean velocity magnitude obtained along three cross-jet lines at y = 0.2, y = 0.5 and y = 0.8.*

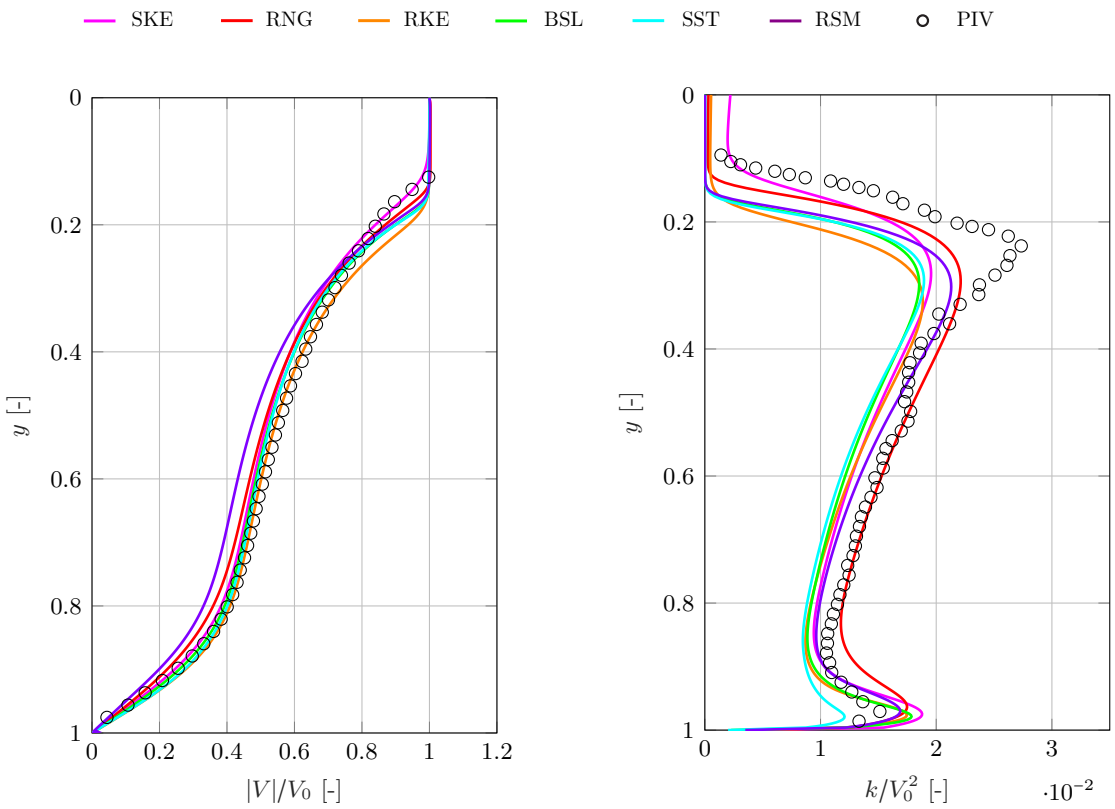

(a) *Dimensionless mean velocity magnitude.* **(b)** *Dimensionless TKE.*

Figure 3.15: *Comparison of PIV results with results of steady RANS CFD simulations of the dimensionless mean velocity magnitude and the dimensionless TKE obtained along the centreline.*

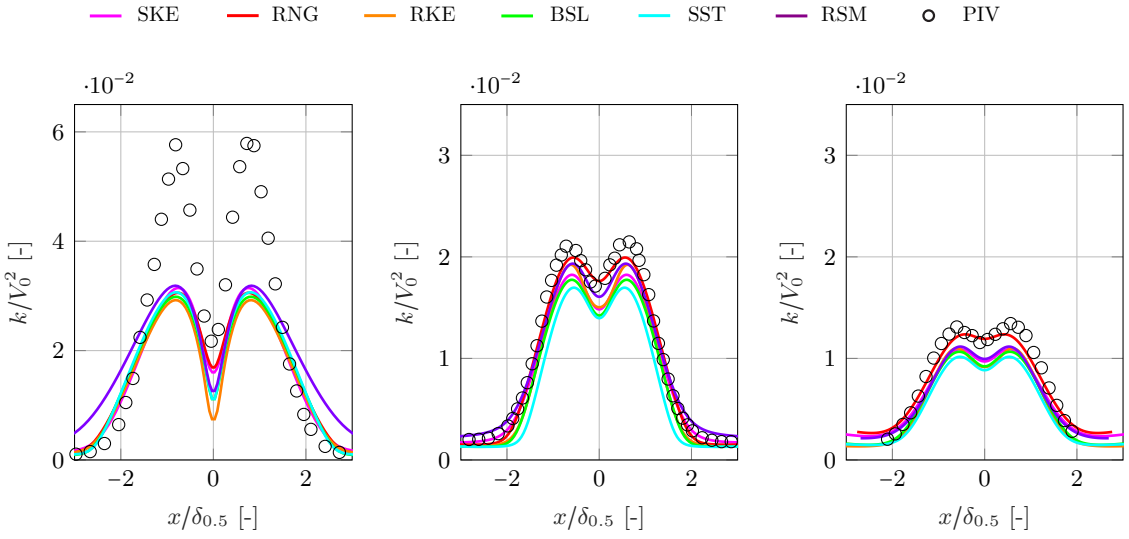

(a) $y = 0.2$. **(b)** $y = 0.5$. **(c)** $y = 0.8$.

Figure 3.16: *Comparison of PIV results with results of steady RANS CFD simulations of the dimensionless TKE obtained along three cross-jet lines at* $y = 0.2$, $y = 0.5$ *and* $y = 0.8$. *Note the different range of the vertical axis in subfigure (a).*

3.6 Conclusion

From the grid-sensitivity study in section 3.4, it is concluded that the fine grid gives nearly grid-independent results, and is therefore used in the remainder of this study. The fine grid has 100,207 cells and 25 cells everywhere across the nozzle contraction. The complete fine grid is shown in figure 3.2. In section 3.5, a validation study is performed. From the validation metrics for the velocity, a clear conclusion could not be drawn, except that the RSM model does not perform well and thus should not be used. For the TKE it can be concluded that the SKE model and the RNG model perform best. Along the centreline, the SKE model performs best. The length of the potential core is best predicted by the SKE model and the RNG model. The jet half width is best predicted by the BSL model and SST model.

From these observations it can be concluded that the SKE model and the RNG model perform best. The models perform equally well and can both be used to predict the behaviour of a 2D planar jet with $Re \approx 7200$. Since the SKE model is least influenced by changes in the grid, it is considered to be a more robust turbulence model than the RNG model with respect to grid resolution and convergence. Therefore, the SKE model is chosen as the most appropriate turbulence model and will be used in the remainder of this study.

Chapter 4

Air curtain model with secondary jets

To investigate the influence of secondary jets on the separation efficiency of an air curtain, 2D CFD simulations are performed for an air curtain model with secondary jets. The model is based on the air curtain model with a single jet, described in Chapter 3. A brief grid-sensitivity analysis is performed in section 4.4. Since no experimental data was available, the turbulence model is chosen based on the validation study of the model with the single jet.

4.1 Computational geometry and grid

The model developed for the air curtain with secondary jets is based on the model used in chapter 3. The computational domain has similar dimensions, only the contraction is removed and two secondary jets are placed at a distance d from the main jet. The distance d is measured from the centre of the main jet to the centre of the secondary jets. The widths of the jets, w_1 (main jet) and w_2 (secondary jets), are kept constant and $w_2 = \frac{1}{2}w_{jet} = \frac{1}{2}w_1 = 25$ mm. Instead of the contraction, three vertical pipes with a length of 1 m are placed above the jet nozzles to generate an appropriate velocity profile. In figure 4.1, the geometry of the model is shown. In this study, three different values for d are considered: $d = \frac{4}{5}w_1$, $d = 2w_1$ and $d = 4w_1$.

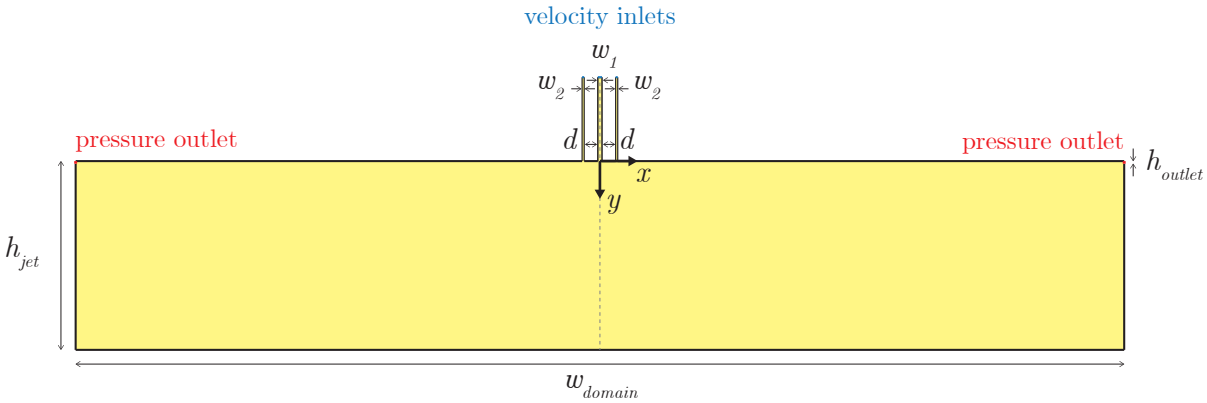

Figure 4.1: *Geometry of the 2D computational domain for $d = 4w_1$ with an indication of the coordinate system and the location of the pressure outlets and the velocity inlets. The dotted line indicates a symmetry line.*

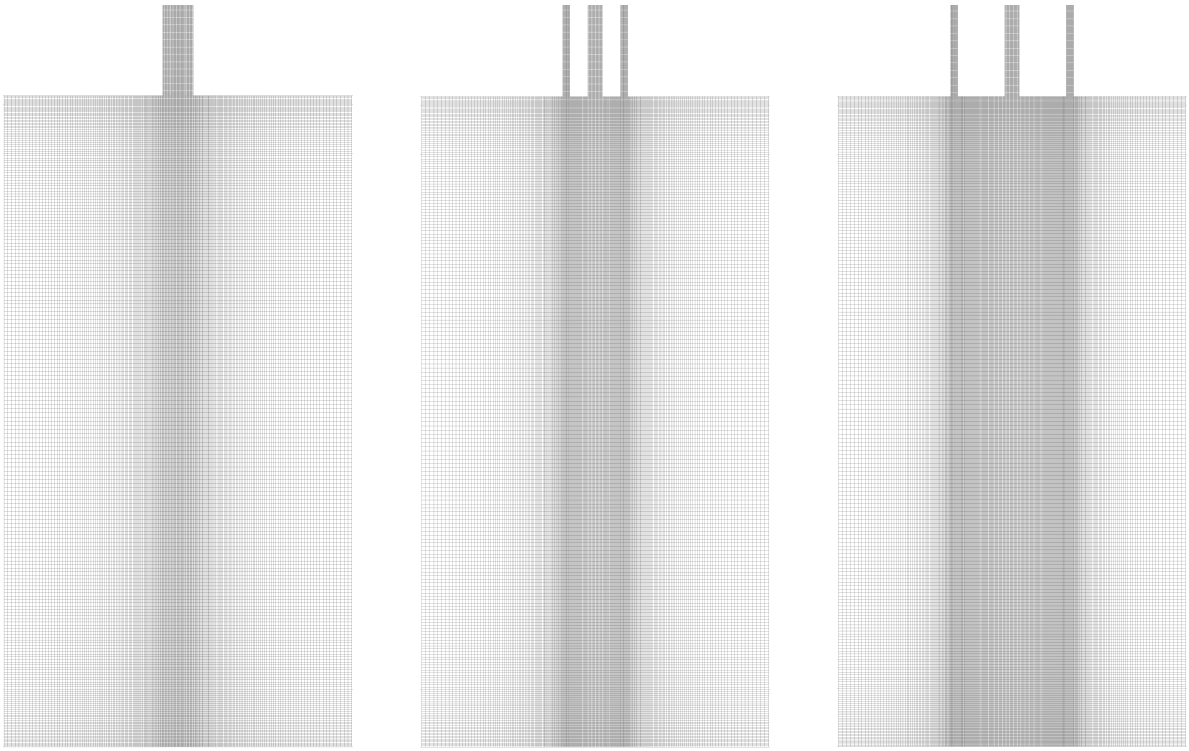

(a) $d = \frac{4}{5}w_1$. **(b)** $d = 2w_1$. **(c)** $d = 4w_1$.

Figure 4.2: *Grid in the region of interest and the lower part of the nozzle pipes for different spacings, d, between the jets.*

Fully structured grids with only quadrilateral cells are created based on the fine grid described in the previous chapter, which consisted of 100,207 cells. In the main nozzle pipe, 25 cells are used across the pipe. In the secondary nozzle pipes, 15 cells ($d = 2w_1$ and $d = 4w_1$) or 12 cells ($d = \frac{4}{5}w_1$) are used across the pipes. The region of interest is meshed accordingly, taking into account the guidelines from Franke et al. (2007). The total number of cells for each grid is 111,430 cells ($d = \frac{4}{5}w_1$), 125,242 cells ($d = 2w_1$) and 143,482 cells ($d = 4w_1$). Figure 4.2 shows the region of interest and the lower part of the nozzle pipes for each of the three grids.

4.2 Boundary conditions

The boundary conditions are chosen similarly to those of the model with the single jet described in the previous chapter. All the surfaces, besides from the velocity inlets and the pressure outlets, are smooth non-slip walls. For the pressure outlets, the turbulence parameters are specified based on the turbulence intensity ($I = 10\%$) and the hydraulic diameter ($D_H = 0.0625$ m). Zero static gauge pressure is enforced at the outlets. For the velocity inlets, the turbulence parameters are specified based on the turbulence intensity ($I = 10\%$) and the turbulence length scale ($l = 0.00175$ m). At the velocity inlets, uniform velocities are imposed. To make a fair comparison between the results from the model with a single jet and the results from the model with secondary jets, the total jet momentum flux is kept constant at the velocity inlets for all configurations. The jet momentum flux is given by

$$\Phi_{P_{jet}} = \rho(V_0^*)^2 w_{jet}, \tag{4.1}$$

where ρ is the density of air (ρ = 1.225 kg/m^3). Using the parameter values of the single jet, this results in $\Phi_{P_{jet}}$ = 0.27 kg/s^2. For the multiple jets, equation (4.1) transforms into

$$\Phi_{P_{jet}} = \rho(V_1^*)^2 w_1 + 2\rho(V_2^*)^2 w_2, \tag{4.2}$$

where V_1^* and V_2^* are the desired discharge velocities at the main jet nozzle and at the nozzles of the secondary jets, respectively. To examine the influence of the velocity, three combinations of V_1^* and V_2^* are used: $V_2^* = \frac{1}{2}V_1^*$, $V_2^* = V_1^*$ and $V_2^* = 2V_1^*$. For simplicity, the parameter $R = V_2^*/V_1^*$ is introduced and is used in the remainder of this study to denote the velocity combinations. The resulting values of V_1^* and V_2^* are listed in table 4.1. Since the nozzle pipes do not contain any contractions, V_1^* and V_2^* are the velocities imposed at the velocity inlets. However, the velocities at the nozzle exits can differ from those at the inlets, so in the remainder of this study, V_1 and V_2 are used to denote the actual discharge velocities measured at the main jet nozzle and the nozzles of the secondary jets, respectively. Regarding the species transport described in the following section, the mass fraction of tracer air is zero at all inlets.

Table 4.1: *Values of the velocity combinations imposed at the velocity inlets, and the associated velocity ratios, R.*

$\boldsymbol{R}$	$\boldsymbol{V_1^*}$ [m/s]	$\boldsymbol{V_2^*}$ [m/s]
1/2	1.878	0.939
1	1.485	1.485
2	0.939	1.878

4.3 Computational configuration

4.3.1 Solver settings for steady RANS simulations

The 2D steady RANS equations are solved with the CFD solver ANSYS 19.0 (2018). Based on the validation study presented in section 3.5 of the previous chapter, the SKE turbulence model is used in combination with scalable wall functions. Pressure-velocity coupling is performed by the coupled algorithm. Pressure interpolation is set to second order and SOU discretisation schemes are used for both the convection terms and the viscous terms of the governing equations. Convergence is monitored through scaled residuals; it is made sure that all scaled residuals level out below four orders of magnitude or drop below twelve orders of magnitude (double-precision).

4.3.2 Modelling of species transport

To measure the transport properties of the air curtain, a second type of air is introduced into the gas mixture with the exact same properties of the air present originally in the model. As a consequence, this 'tracer air' will not influence the flow properties of the air curtain, thus will act solely as a passive scalar. In the unsteady RANS simulations, the advection-diffusion equation is solved to determine the transport of the tracer air. The density of the gas mixture is computed based on the volume-weighted mixing law, as recommended for non-ideal gas mixtures (ANSYS Inc., 2018). For the specification of the mass diffusivity of the species in the gas mixture,

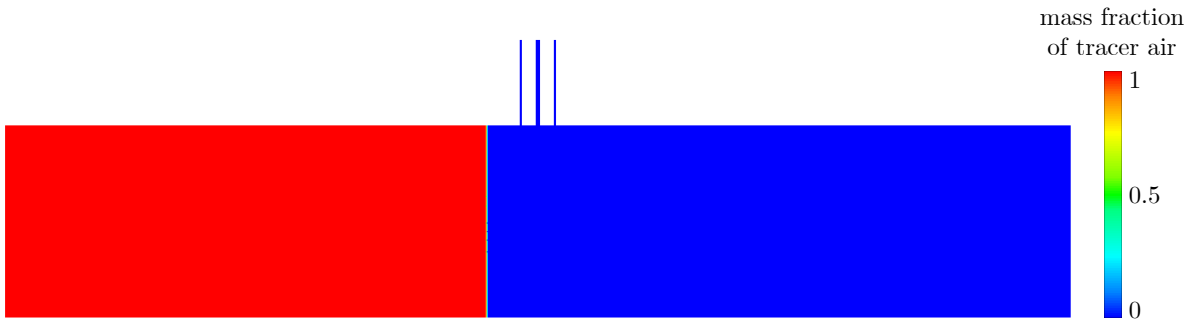

Figure 4.3: *Initial distribution of tracer air. The initial mass fraction of the tracer air is 1 in the left side of the domain, and 0 in the rest of the domain.*

the kinetic theory is used, hence solving the energy equation is not necessary. The tracer air is introduced to the left of the region of interest, the portion of the computational domain indicated in figure 4.3. The tracer air is introduced as a uniform distribution (i.e., not as a mass source), consequently there is a finite amount of tracer air present in the domain.

4.3.3 Solver settings for unsteady RANS simulations

The 2D unsteady RANS (URANS) simulations are solved with equivalent solver settings as the steady RANS simulations. Concerning the transient formulation, the Bounded Second Order Implicit formulation is used for optimal stability. For a stable, efficient calculation, the Courant number should not exceed a value of 20 – 40 in the most sensitive transient regions of the domain (ANSYS Inc., 2018). The Courant number is defined as

$$Cr = \frac{V_{max}\Delta t}{\Delta y}, \tag{4.3}$$

where V_{max} is the maximum velocity, Δt the time step and Δy the minimum cell size in the flow direction (Franke et al., 2007). For all configurations, Δy is the same and has a value of 4 mm. A constant time step of $\Delta t = 0.01$ s is chosen for all configurations. The resulting values of the Courant number are indicated in table 4.2. The values are well below the recommended values to increase stability. For the initialization, the solutions from the steady RANS simulations were used. To allow the full development of the flow before introducing the tracer air, 5 s of flow time are imposed. After those 5 s, the tracer air is introduced as described in section 4.3.2. Subsequently, all simulations are run for 150 s flow time to allow the transport and measurement of the tracer air across the air curtain and throughout the domain. Convergence was monitored through scaled residuals; it was made sure that all scaled residuals levelled out below four orders of magnitude or dropped below ten orders of magnitude per time step.

Table 4.2: *Values of the Courant number for different R.*

R	V_{max} [m/s]	Cr
0	2.27	5.7
1/2	2.15	5.4
1	1.68	4.2
2	2.09	5.2

4.4 Grid-sensitivity analysis

To make sure grid-independent results are truly obtained with the grids described in section 4.1, a brief grid-sensitivity analysis is conducted for $d = 4w_1$ with $R = 1$. Two grids are used; the basic grid described in section 4.1 (figure 4.2c) and a fine grid constructed using a linear refinement factor of 1.44 in each direction, resulting in a grid with 297,171 cells. The fine grid has 35 cells across the main nozzle pipe and 21 cells across the secondary nozzle pipes. The grids are compared based on the dimensionless mean velocity magnitude, $|V|/V_0$, and the dimensionless TKE, k/V_0^2, along the main jet centreline and a cross-jet line at $y = 0.5$ in the region of interest. In the remainder of this study, these flow variables are made dimensionless with V_0, which is defined as $V_0 = \sqrt{V_1^2 + 2\frac{w_2}{w_1}V_2^2} = \sqrt{V_1^2 + V_2^2}$.

To quantify the grid-sensitivity results, the GCI (equation (3.4)) is used for the basic grid. Since only two grids are analysed, the recommended safety factor is $F_s = 3$ (Roache, 1994). However, the grids are based on the results of a similar grid-sensitivity study (section 3.4), and are therefore expected to be more reliable, so the safety factor of 1.25 is kept. The results of the grid-sensitivity analysis including the band of the GCI for the basic grid are plotted in figure 4.4 and 4.5. The average and maximum values of the GCI are presented in table 4.3. The high maximum value of the GCI of the centreline velocity is found near the bottom ($y = 1$). This value occurs only once and might be a post-processing error since the second maximum value is only 4.6%. The centreline TKE shows large values of the GCI at $y = 0.2$ and $y = 1$, this is due to the large gradients in those areas. Even though some large maximum values of the GCI occur, the average values are small. Thus, from this grid-sensitivity analysis it can be concluded that the results from the basic grid and from the fine grid are sufficiently similar and therefore the basic grid solution shows an adequate degree of independence on the implemented spatial discretisation of the mesh.

Table 4.3: *Maximum and average GCI values of $|V|/V_0$ and k/V_0^2 for the basic grid along the centreline and a cross-jet line at $y = 0.5$.*

GCI [%]	max.	avg.
centreline velocity	24.0%	1.3%
velocity at $y = 0.5$	1.3%	0.5%
centreline TKE	26.4%	3.6%
TKE at $y = 0.5$	3.2%	2.2%

4.5 Conclusion

From the grid-sensitivity study in section 4.4, it is concluded that the results from the basic grid show a sufficient degree of independence on the mesh. Therefore the basic grid is used in the remainder of this study to investigate secondary jets. The basic grid has 111,430 cells ($d = \frac{4}{5}w_1$), 125,242 cells ($d = 2w_1$) and 143,482 cells ($d = 4w_1$), and 25 cells across the main nozzle pipe and 15 cells ($d = 2w_1$ and $d = 4w_1$) and 12 cells ($d = \frac{4}{5}w_1$) across the secondary nozzle pipes. The grids are partially shown in figure 4.2. Based on the validation study of the model of a single jet in section 3.5, the SKE turbulence model was chosen as the most appropriate turbulence model and is therefore also used in the model of the secondary jets. Furthermore, the boundary conditions as described in section 4.2, and the solver settings as described in section 4.3 are used in the remainder of this research for the model configurations with secondary jets.

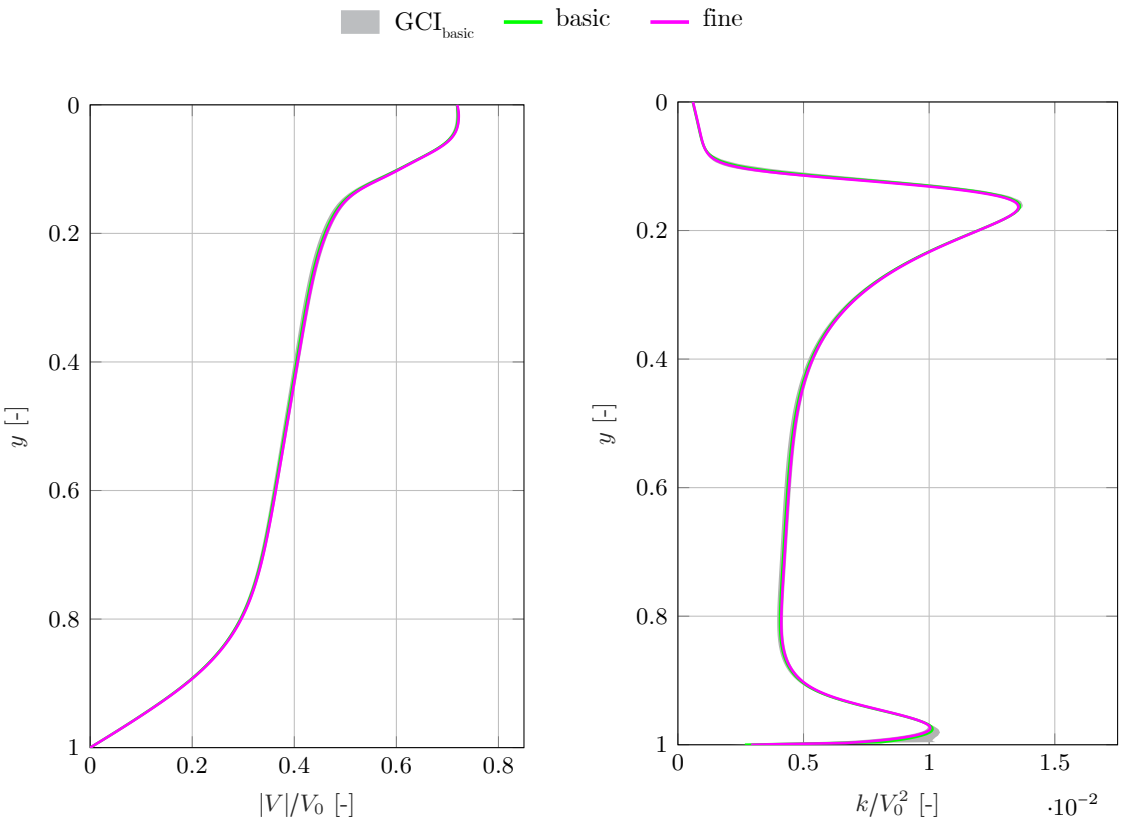

(a) *Dimensionless mean velocity magnitude.* **(b)** *Dimensionless TKE.*

Figure 4.4: *Band of GCI_{basic} for $|V|/V_0$ and k/V_0^2 along the centreline.*

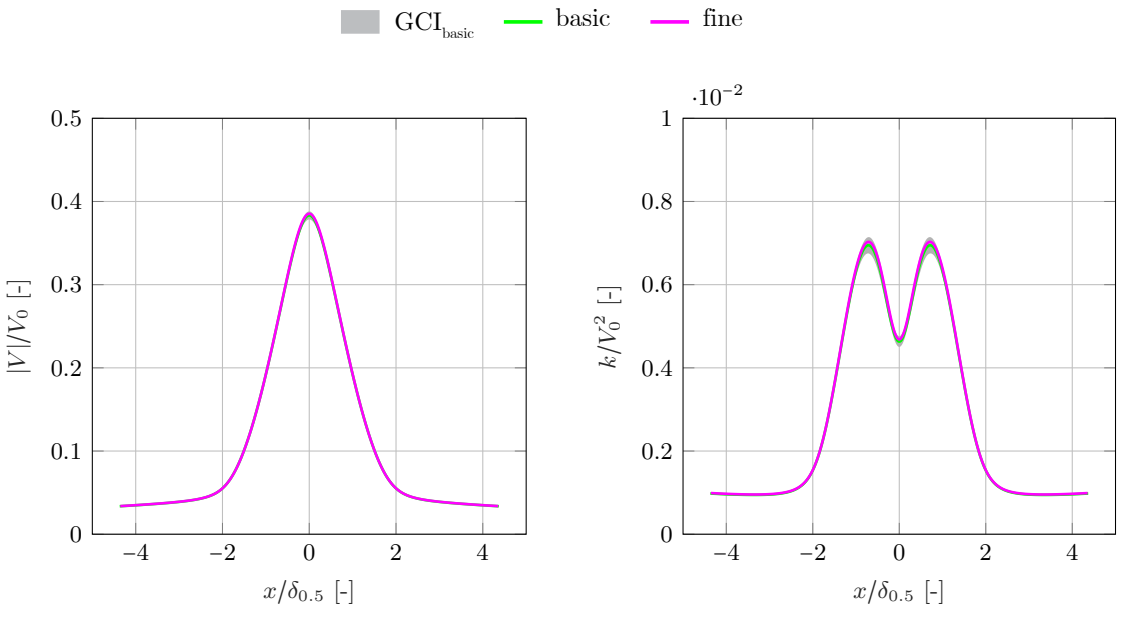

(a) *Dimensionless mean velocity magnitude.* **(b)** *Dimensionless TKE.*

Figure 4.5: *Band of GCI_{basic} for $|V|/V_0$ and k/V_0^2 along a cross-jet line at $y = 0.5$.*

Chapter 5

Results

This chapter presents the results from the simulations described in Chapter 3 and 4. Steady RANS simulations are performed to gather information about velocity and entrainment. Velocity profiles from the CFD model of the single jet are compared with the theoretical model described in section 2.4. The centreline velocity and cross-jet velocity profiles from the CFD model configurations with secondary jets are compared with each other and with those of the single jet in section 5.1. Next, the volume flux and entrainment velocity are investigated for all configurations in section 5.2. Species transport across the jets and the circulation of species in the bounded domain is studied by means of URANS simulations in section 5.3.

5.1 Velocity

The velocity profiles of the single jet model are compared with the theory of a single jet described in Chapter 2. Equations (2.20) and (2.21) are used to describe the theoretical centreline y-velocity and cross-jet y-velocity profiles, respectively. In figures 5.1, 5.2 and 5.3, the label *Theory* refers to these equations with two different theoretical opening angles, $\alpha = 1/5$ and $\alpha = 1/6$, and the label *CFD* refers to the results from the CFD model with a single jet. The theoretical model only applies to the fully developed flow region of a free jet, and thus does not suffice in the flow development region and the impingement region.

Figure 5.1 shows the dimensionless centreline velocity of the single jet model compared with the theoretical model. As expected, the theoretical model only corresponds well with the results of the CFD model in the region $y \sim 0.15 - 0.75$, which coincides with the fully developed flow region. In this region, the theoretical model with $\alpha = 1/5$ (as suggested in section 2.4) slightly underpredicts the centreline velocity. This difference almost disappears when considering a smaller opening angle, such as $\alpha = 1/6$, instead of $\alpha = 1/5$, as shown in figure 5.1. The flow development region, containing the potential core, ends at $y \sim 0.1 - 0.15$. This is in accordance with previous studies on plane jets by Khayrullina et al. (2017) and Maurel and Solliec (2001), who found potential core lengths of $4w_{jet} - 7w_{jet}$, corresponding to $y \sim 0.09 - 0.16$. As visible in figure 5.1, the results of the CFD model start deviating from the theoretical model at $y \sim 0.75$, implying the start of the impingement zone, which is in line with the findings from Gutmark et al. (1978). However, Maurel and Solliec (2001) claim that the height of the impingement region only constitutes $12 - 13\%$ of the total jet height, regardless of Reynolds number, nozzle width or jet height. They defined a velocity law for the impingement zone and interpreted the end of that region as the height where that velocity law intersects with the velocity law of the fully developed flow region. Nevertheless, this definition does not take into account the

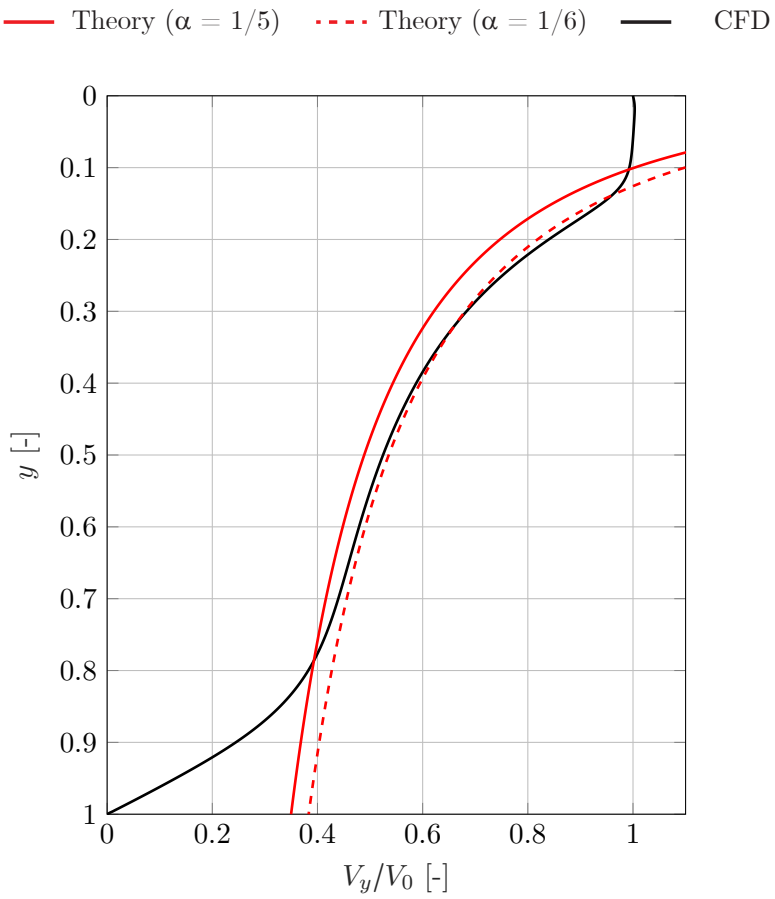

Figure 5.1: *Dimensionless y-velocity, V_y/V_0, of a single jet along the centreline, obtained with a CFD model and a theoretical model. The theoretical centreline velocity is described by equation (2.21) with $\alpha = 1/5$ and $\alpha = 1/6$.*

transition from the fully developed region to the impingement zone, resulting in the impingement zone starting further downstream.

Figures 5.2 and 5.3 compare dimensionless cross-jet y-velocity profiles of the theoretical model and the CFD model along cross-jet lines at $y = 0.2$, $y = 0.5$ and $y = 0.7$. For $\alpha = 1/5$, the maximum velocities are underestimated by the theoretical model, which is expected from figure 5.1. In addition, the spreading is slightly overestimated. For $\alpha = 1/6$, the maximum velocities and the spreading from the theoretical model have a better agreement with the results from the CFD model, which is expected when considering a smaller opening angle. When non-dimensionalising the results with the maximum velocity, V_{max}, and the jet half width, $\delta_{0.5}$ (figure 5.3), the theoretical models completely overlap, as expected, since the Gaussians describing the theoretical velocity profiles are self-similar. The results from the theoretical model are in agreement with the results from the CFD model within the region $|x/\delta_{0.5}| < 1$. For $|x/\delta_{0.5}| > 1$, the theoretical results shows a faster decrease in y-velocity than the CFD results, leading to $V_y = 0$ in $|x/\delta_{0.5}| > 3$. In the CFD results, V_y never becomes zero due to the circulating flows in the bounded domain. The theoretical model assumes an infinite unbounded domain, and therefore the results do not correspond to the results of the CFD model at the boundaries of the jet and outside of the jet.

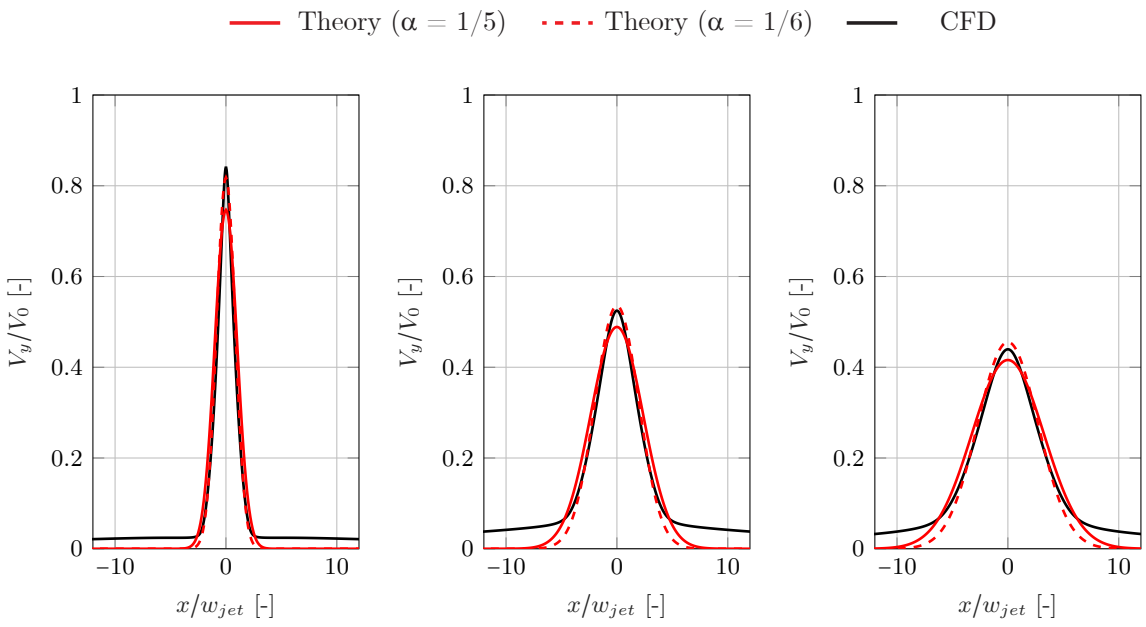

(a) $y = 0.2$. **(b)** $y = 0.5$. **(c)** $y = 0.7$.

Figure 5.2: *Dimensionless y-velocity, V_y/V_0, of a single jet along cross-jet lines at $y = 0.2$, $y = 0.5$ and $y = 0.7$, obtained with a CFD model and a theoretical model. The theoretical velocity is described by equation (2.20) with $\alpha = 1/5$ and $\alpha = 1/6$.*

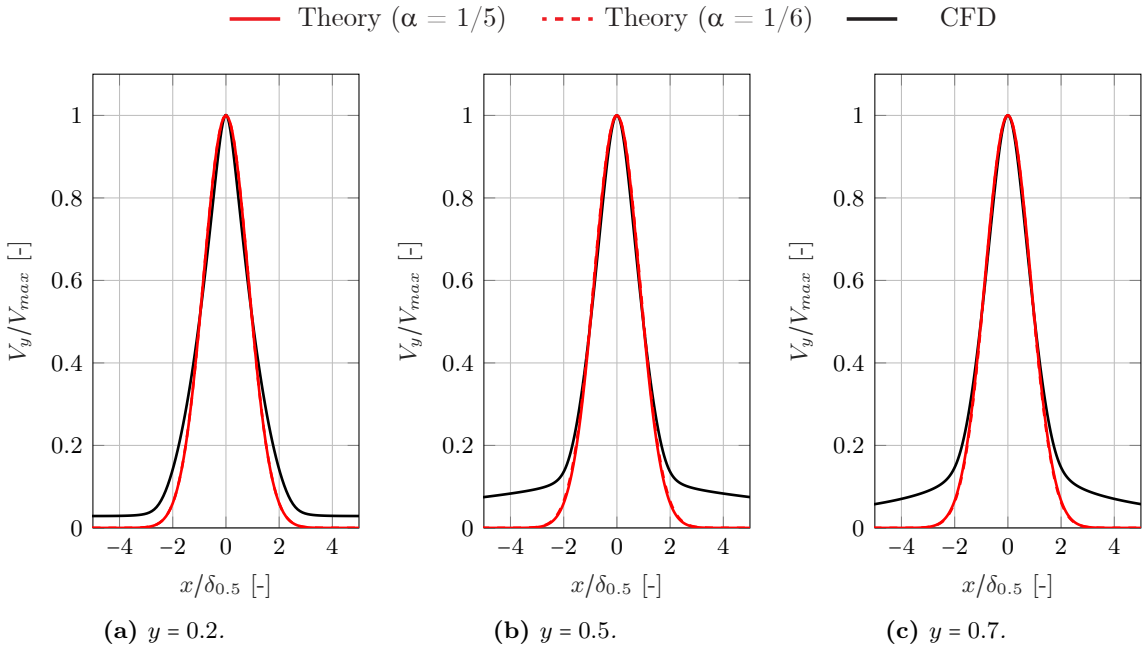

(a) $y = 0.2$. **(b)** $y = 0.5$. **(c)** $y = 0.7$.

Figure 5.3: *Dimensionless y-velocity, V_y/V_{max}, of a single jet along cross-jet lines at $y = 0.2$, $y = 0.5$ and $y = 0.7$, obtained with a CFD model and a theoretical model. The theoretical velocity is described by equation (2.20) with $\alpha = 1/5$ and $\alpha = 1/6$. Note the different non-dimensional horizontal axis, $x/\delta_{0.5}$.*

The velocity profiles of the model configurations with secondary jets are compared with each other and with those of the single jet model in figures 5.4 and 5.6. Figure 5.4 shows the mean centreline velocity magnitude for all configurations. The gray lines indicate the centreline velocities above the combined point, as described in section 2.4.4. The positions of the combined points are similar for equal R. However, it can be observed that for larger d, the merging happens slightly further downstream. The configuration with $d = 4w_1$ and $R = 2$ is an exception; due to the asymmetry in the flow, the merging starts further downstream. The behaviour of the centreline velocity above the combined point can best be described by looking at the velocity fields of the different configurations in figure 5.5. For $R = 2$, the main jet gets entrained by the secondary jets, and therefore, loses most of its velocity, causing a large drop in centreline velocity around $y = 0.1$. This is not the case for $d = \frac{4}{5}w_1$ (figure 5.5c), where the jets are placed so close to each other that there is low shear between the jets, and therefore, the main jet does not get entrained that much by the secondary jets. For $d = 4w_1$ (figure 5.5i), the main jet behaves asymmetrically, and therefore the centreline velocity drops substantially, since the velocity in the stagnation zone is measured instead of in the main jet. After the decrease in

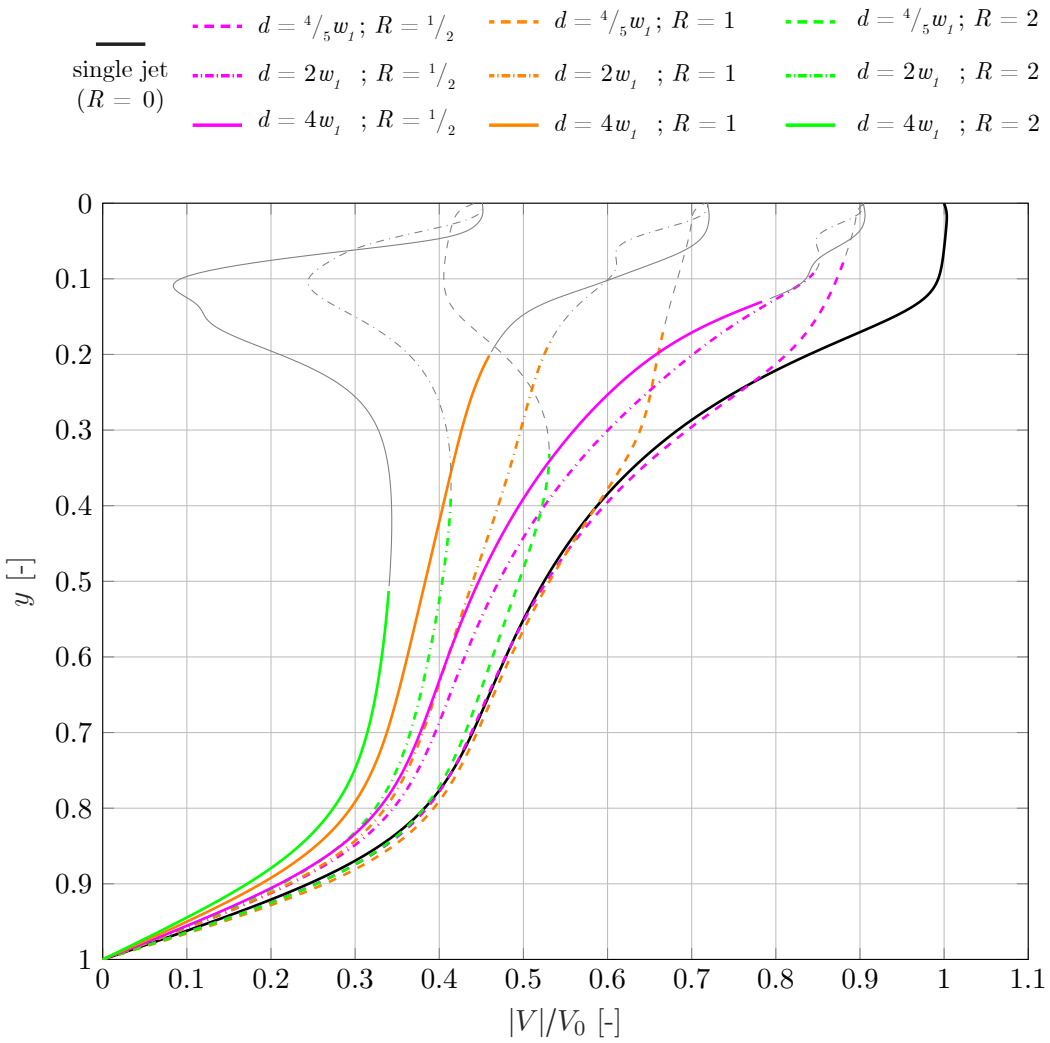

Figure 5.4: *Dimensionless centreline velocity magnitude for different d and R. The transition from gray to color indicates the combined point of multiple jets.*

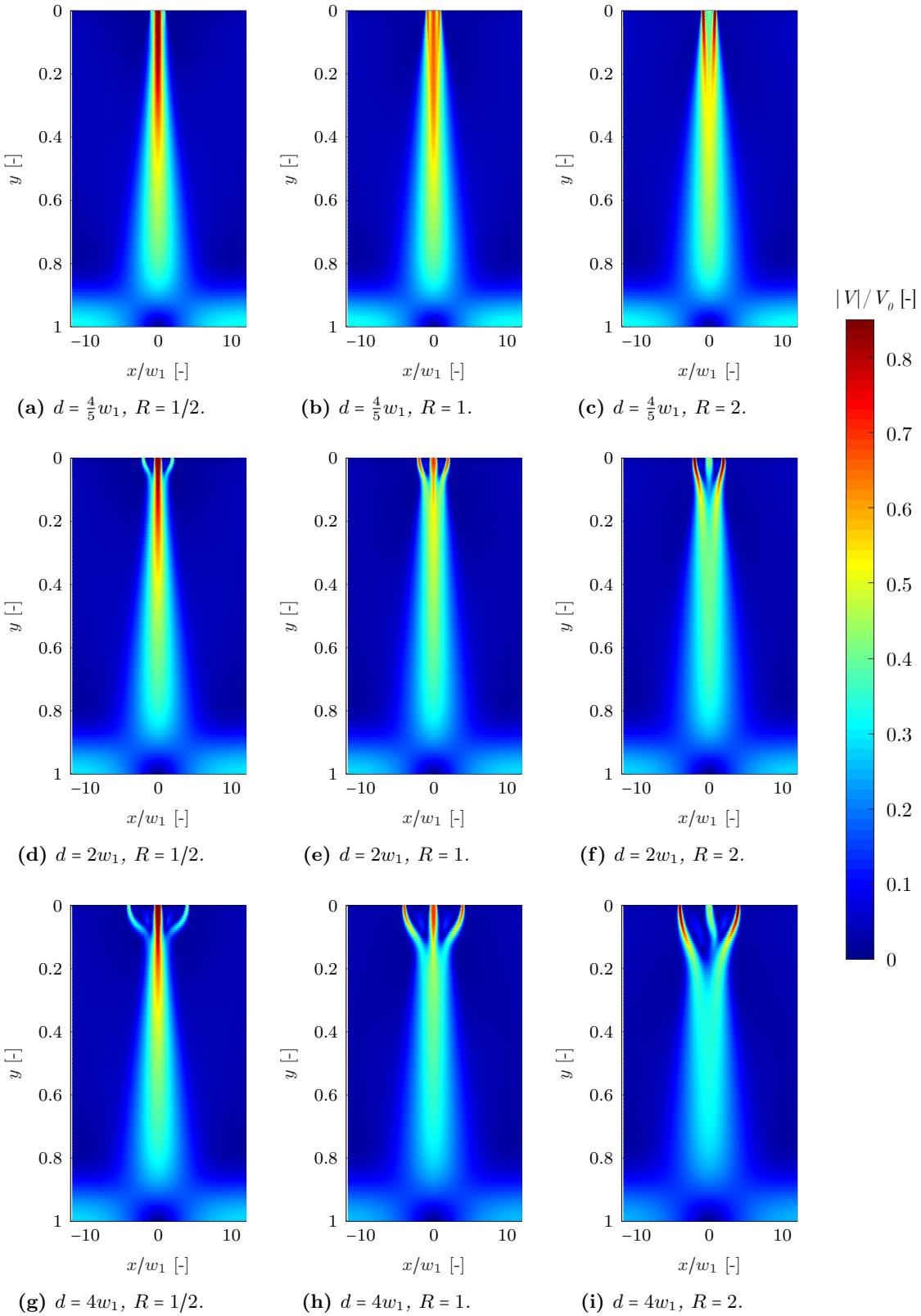

(a) $d = \frac{4}{5}w_1,\ R = 1/2.$ **(b)** $d = \frac{4}{5}w_1,\ R = 1.$ **(c)** $d = \frac{4}{5}w_1,\ R = 2.$

(d) $d = 2w_1,\ R = 1/2.$ **(e)** $d = 2w_1,\ R = 1.$ **(f)** $d = 2w_1,\ R = 2.$

(g) $d = 4w_1,\ R = 1/2.$ **(h)** $d = 4w_1,\ R = 1.$ **(i)** $d = 4w_1,\ R = 2.$

Figure 5.5: *Contour plots of the dimensionless mean velocity magnitude, $|V|/V_0$, for different d and R.*

centreline velocity, the jets start to combine and the centreline velocity increases again until the combined point for all d with $R = 2$. The configurations with $R = 1/2$ and $R = 1$ do not experience this behaviour, since $V_2 \leq V_1$, hence the resulting centreline velocity will not increase with respect to V_1. For $d = \frac{4}{5}w_1$ (figures 5.5a and 5.5b), the centreline velocity slowly decreases until the combined point. For $d = 2w_1$ (figures 5.5d and 5.5e), the centreline velocity rapidly decreases until the jets start to combine. When combining, the centreline velocity remains constant for a small distance downstream and then starts decaying again until the combined point. The configurations with $d = 4w_1$ (figures 5.5g and 5.5h) have a small potential core, but downstream of the potential core the centreline velocity starts decreasing rapidly until the combined point. Downstream of the combined point all configurations behave like a single jet. The centreline velocity decreases with increasing R, which is expected since V_1 decreases with increasing R. The configurations with $d = \frac{4}{5}w_1$ have almost the same centreline velocity as the single jet. The configurations with $d = 2w_1$ have a smaller centreline velocity, and those with $d = 4w_1$ have an even smaller centreline velocity. For $d = \frac{4}{5}w_1$, there is less shear between the jets, thus less turbulence, hence the centreline velocity does not dissipate as rapidly as for the other configurations, resulting in a higher centreline velocity. For $d = 2w_1$ and $d = 4w_1$, there is a larger shear between the jets, resulting in a faster dissipation of the centreline velocity. For the configuration with $d = 4w_1$ and $R = 1/2$, the secondary jets are fully entrained by the main jet, having almost no effect on the flow of the main jet. Therefore, the configuration with $d = 4w_1$ and $R = 1/2$ approximately resembles a single jet. The configuration with $d = 4w_1$ and $R = 2$ approximately resembles two merging jets, since the main jet is fully entrained by the secondary jets.

Figure 5.6 shows the cross-jet velocity profiles of all the configurations along $y = 0.7$. At this downstream distance, the jets of all configurations have combined, but the jets are not yet influenced by the bottom wall. Therefore, the profiles should resemble cross-jet profiles of single jets in the fully developed flow region and thus be self-similar. Figure 5.6b displays the dimensionless cross-jet velocity $|V|/V_{max}$ versus $x/\delta_{0.5}$, which clearly indicates this self-similarity. Figure 5.6a shows the dimensionless cross-jet velocity $|V|/V_0$ versus x/w_1. The maximum velocities behave as expected from the analysis of the centreline velocity (figure 5.4); the maximum velocity decreases with increasing d and with increasing R. The dimensionless maximum velocities, $|V_{max}|/V_0$, and the jet half widths, $\delta_{0.5}$, are presented in table 5.1 and 5.2, respectively. The values are normalised with $|V_{max}|/V_0$ and $\delta_{0.5}$ of the single jet. The jet half widths are directly related to the maximum velocities; a large jet half width corresponds to a low maximum velocity. This is expected from the self-similarity property of the cross-jet velocity profile.

Table 5.1: *Normalised dimensionless maximum velocity, $|V_{max}|/V_0$, based on the cross-jet velocity at $y = 0.7$ for different d and R. All values are normalised with $|V_{max}|/V_0$ of the single jet.*

$\boldsymbol{\lvert V_{max}\rvert/V_0}$	$R = 1/2$	$R = 1$	$R = 2$
$d = \frac{4}{5}w_1$	1.00	1.01	0.98
$d = 2w_1$	0.90	0.86	0.83
$d = 4w_1$	0.86	0.77	0.72

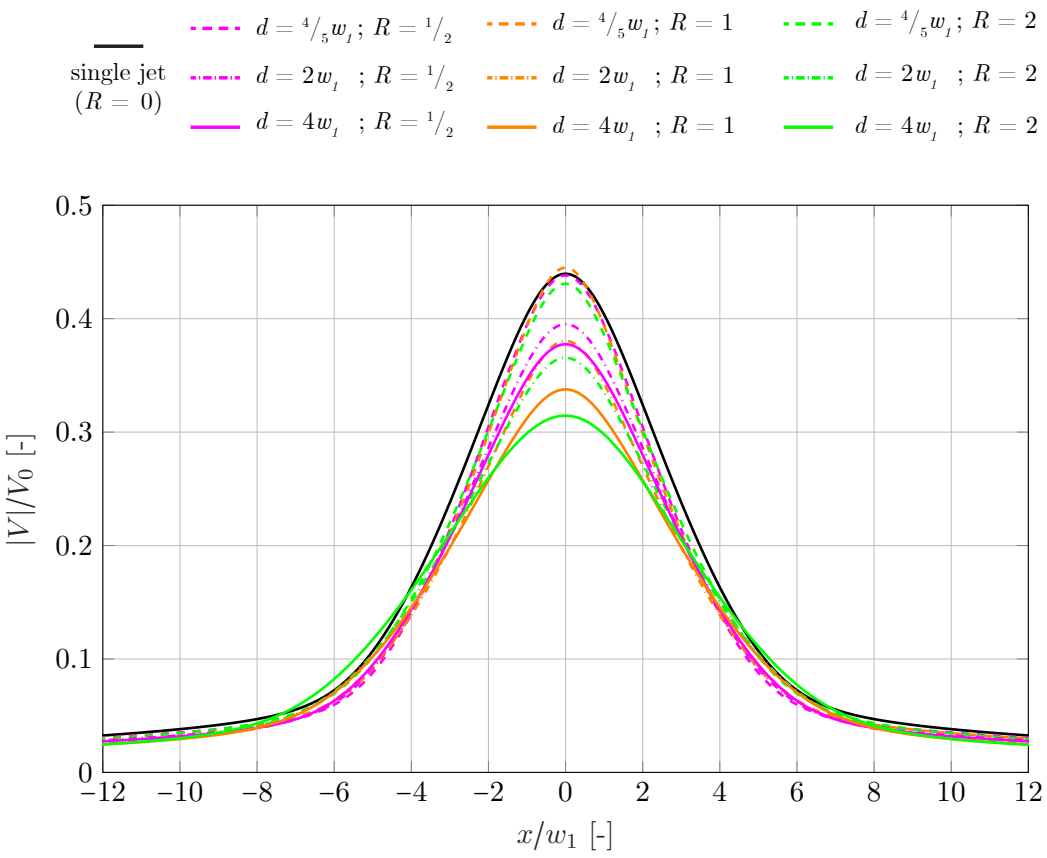

(a) *Dimensionless cross-jet velocity,* $|V|/V_0$.

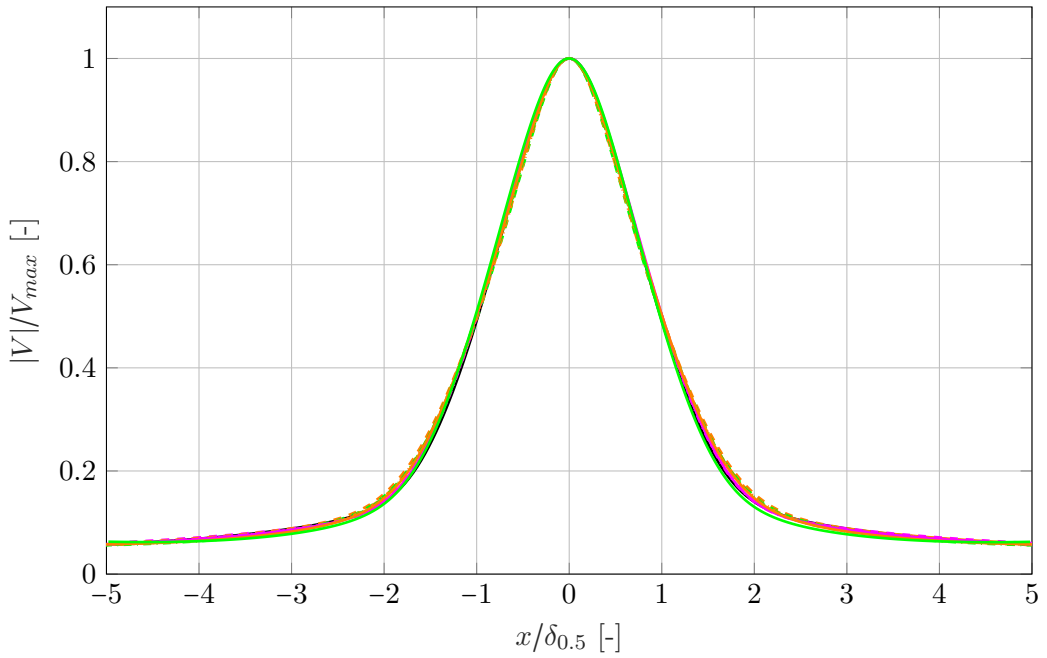

(b) *Dimensionless cross-jet velocity,* $|V|/V_{max}$. *Note the different non-dimensional horizontal axis,* $x/\delta_{0.5}$.

Figure 5.6: *Dimensionless mean velocity magnitude along a cross-jet line at* $y = 0.7$ *for different* d *and* R.

Table 5.2: *Normalised jet half width, $\delta_{0.5}$, based on the cross-jet velocity at $y = 0.7$ for different d and R. All values are normalised with $\delta_{0.5}$ of the single jet.*

$\boldsymbol{\delta_{0.5}/w_1}$	$R = 1/2$	$R = 1$	$R = 2$
$d = \frac{4}{5}w_1$	0.90	0.87	0.95
$d = 2w_1$	0.97	0.97	1.04
$d = 4w_1$	1.00	1.08	1.23

5.2 Entrainment

Entrainment is described in section 2.4.2 as the intake of fluid by the jet across its boundary. To quantify the entrainment, the dimensionless volume flux, Q/V_0w_1, and the dimensionless entrainment velocity, V_E/V_0, are determined for all configurations. The volume flux, Q, is calculated for different values of y, according to equation (2.22), which takes the integral of the y-velocity over an infinite horizontal (cross-jet) distance. Since the theoretical model assumes that the y-velocity equals zero outside the jet, the volume flux will be zero outside the jet as well. However, due to the bounded domain of the CFD model, the y-velocity outside the jet is nonzero. Therefore, the integration should only take place inside the jet, and thus the boundaries of the jet need to be determined. For a single jet, the jet boundary can be approximated by $R_{jet} = 2\delta_{0.5}$, or by $R_{jet} = \alpha y$ with $\alpha = 1/6$, as shown in figures 5.1 and 5.2. However, these relations do not apply for multiple jets, and therefore another definition needs to be found. The dynamics of jets are entirely controlled by the velocity gradients at the jet boundaries. These velocity gradients induce a shear flow which generates vorticity. The vorticity, $\boldsymbol{\omega}$, is defined as

$$\boldsymbol{\omega} = \nabla \times \mathbf{u}. \tag{5.1}$$

At the boundaries of the jet, a shear flow is generated, which gives rise to instabilities. These instabilities lead to the formation of vortices which entrain air, giving a jet its defining triangular shape. In theory, the velocity field outside the jet equals zero, hence there is no vorticity outside the jet. In practise, this is not the case due to the bounded the domain. However, the vorticity is very small outside the jet, so the boundary of the jet can be defined by the position where $|\boldsymbol{\omega}| = \omega_c$, in which ω_c is some small critical value of the vorticity, i.e. the jet is defined by $|\boldsymbol{\omega}| > \omega_c$. The theoretical definitions, $R_{jet} = 2\delta_{0.5}$ and $R_{jet} = \frac{1}{6}y$, assume to capture 95% of the jet, while it is desired to capture the whole jet, including the shear layer. Because it is unclear when the jet is fully captured, two values of ω_c are taken which both indicate a wider jet. Figure 5.7 pictures the boundaries of the single jet by making use of of $\omega_c = 0.5$ and $\omega_c = 0.25$, and the theoretical definitions, $R_{jet} = 2\delta_{0.5}$ and $R_{jet} = \frac{1}{6}y$.[1] Hereinafter, the jet boundaries of all configurations are determined by $\omega_c = 0.5$ and $\omega_c = 0.25$.

Figure 5.8 compares the dimensionless volume flux, Q/V_0w_1, at certain y downstream for a single jet, obtained with the CFD model and the theoretical model (equation (2.23)). The volume fluxes obtained with the CFD model are determined with $\omega_c = 0.5$ and $\omega_c = 0.25$. The results of the CFD model are in good agreement with the results from the theoretical model in the fully developed flow region. When taking $\omega_c = 0.25$ instead of $\omega_c = 0.5$, the boundaries of the jet lay further apart and a larger volume is captured, as visible in figure 5.7. This has a perceivable effect on the volume flux further downstream ($y > 0.25$), where the difference between $\omega_c = 0.25$

[1] Note that the boundaries of the jet are not exactly linear, as implied by most literature. However, Kotsovinos (1976) found that on a large scale the half width of a plane turbulent jet is a 'weak' nonlinear function of y, following a similar trend as $R_{jet} = 2\delta_{0.5}$ in figure 5.7.

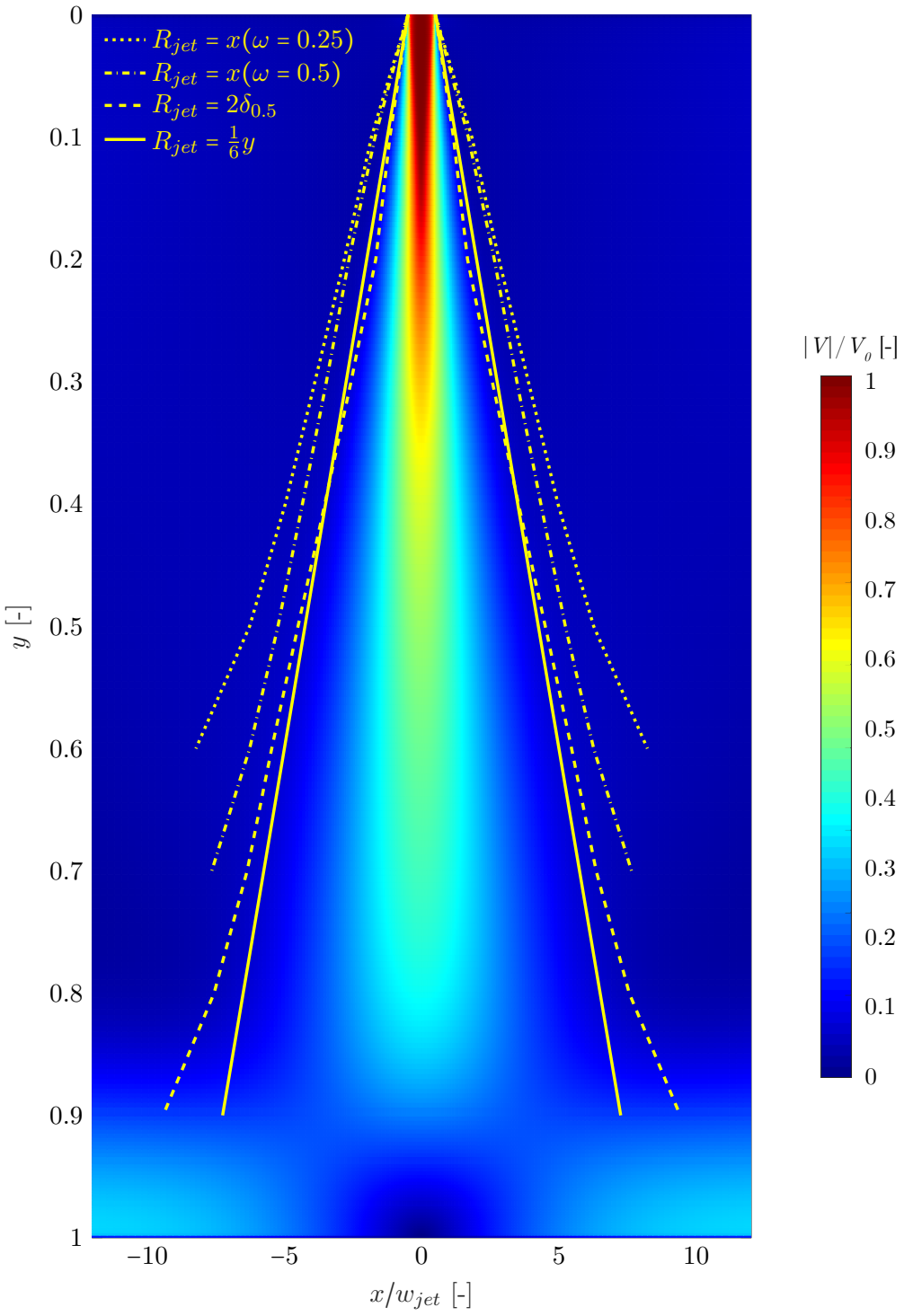

Figure 5.7: *Description of the jet boundary by means of the vorticity, ω, the jet half width, $\delta_{0.5}$, and the theoretical definition, $R_{jet} = \frac{1}{6}y$.*

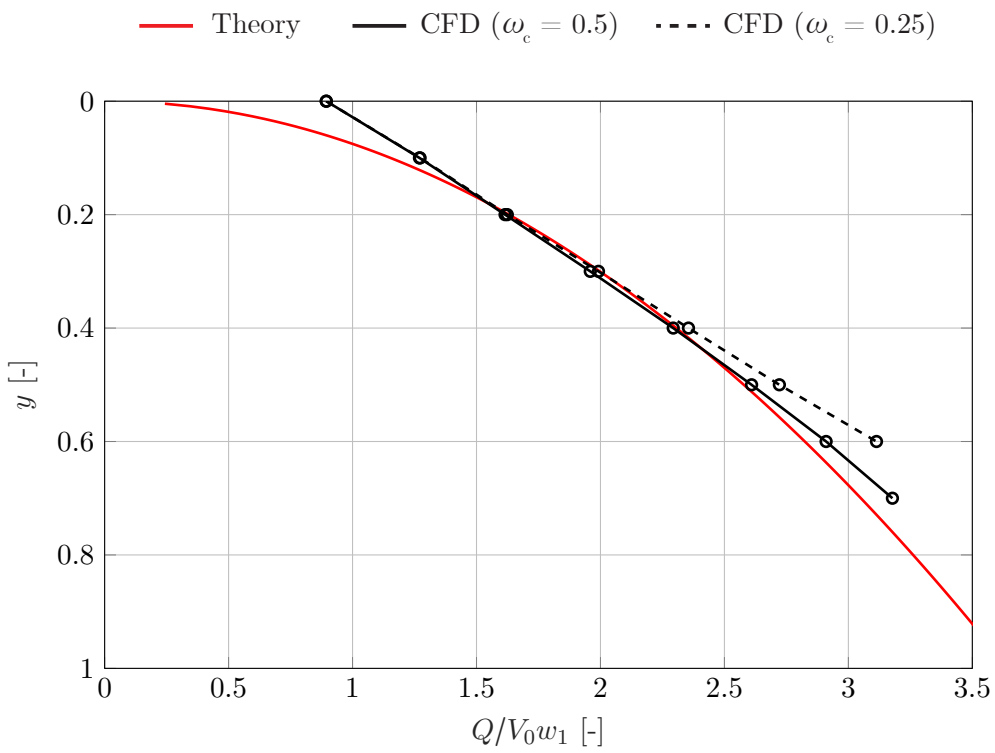

Figure 5.8: *Dimensionless volume flux, $Q/V_0 w_1$, of a single jet, obtained with a CFD model and a theoretical model. The theoretical volume flux is described by equation (2.23).*

and $\omega_c = 0.5$ becomes more prominent. The volume flux determined by $\omega_c = 0.25$ downstream of $y = 0.25$ is thus higher than the volume flux determined by $\omega_c = 0.5$. The volume flux obtained with $\omega_c = 0.5$ results in a better agreement with theory, and therefore this is considered a better approximation of the jet boundary than $\omega_c = 0.25$.

Figure 5.9 shows the dimensionless volume flux, $Q/V_0 w_1$, at certain y downstream for a single jet and for all configurations with secondary jets. At $y = 0$, the air curtains with secondary jets have a larger Q than the single jet. This is expected since the total jet momentum flux (equation (4.2)) is kept constant at the inlets, resulting in larger Q at the nozzles for the secondary jet configurations. The configurations with secondary jets entrain less air than the single jet, because of the higher velocity of the single jet, resulting in smaller volume flux gradients (i.e. smaller Q downstream). The difference between the results obtained with $\omega_c = 0.5$ and $\omega_c = 0.25$ can almost be neglected.

The difference in volume flux, $\mathrm{d}Q$, gives the entrainment flux through the boundaries of the jet. According to conservation of mass, the entrainment velocity is then defined as $V_E = \mathrm{d}Q/\mathrm{d}y$ (equation (2.25)). Since V_E is computed from the volume flux, and not directly measured, it is desired to know if it represents the actual entrainment velocity at the boundaries of the jet. Therefore, the entrainment velocity is compared with the x-velocity at the boundary of the jet, V_x.[2] Figure 5.10 compares the dimensionless entrainment velocity, V_E/V_0, and the dimensionless x-velocity, V_x/V_0, at certain y downstream for a single jet, obtained with the CFD model and the theoretical model (equation (2.26)). The entrainment velocity and the x-velocity from the

[2] V_E describes the total velocity magnitude at both boundaries, therefore, V_x is also defined as the total (absolute) x-velocity at both boundaries.

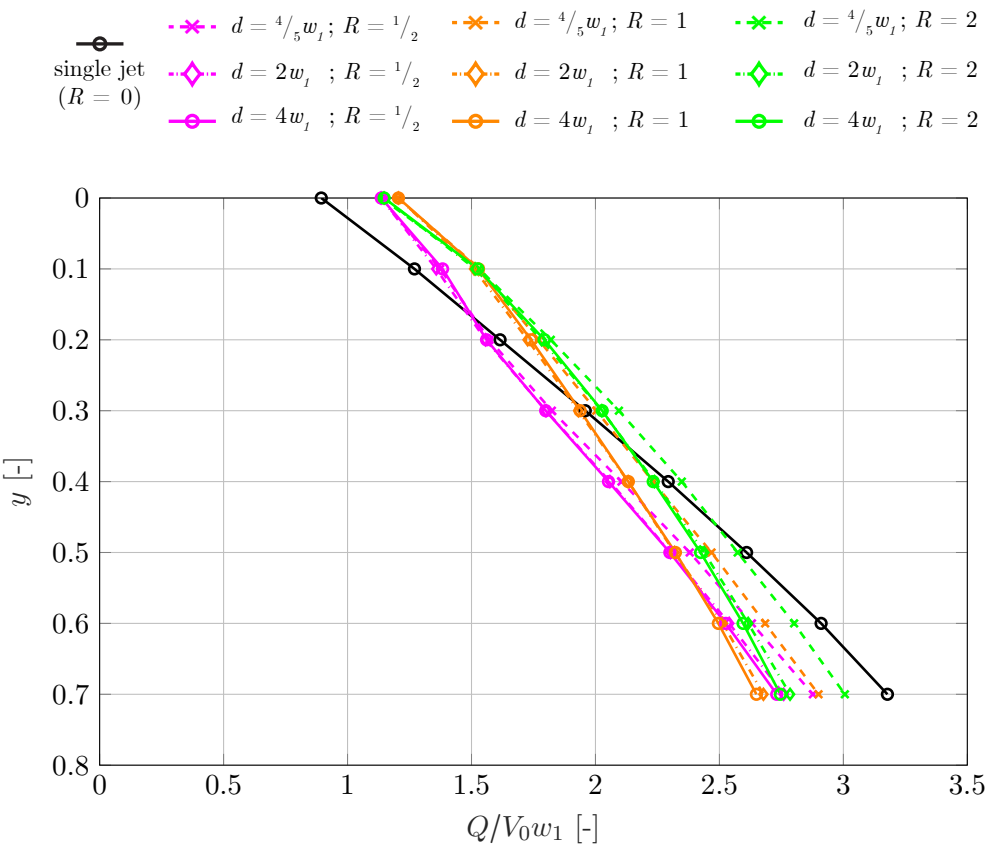

(a) *$Q/V_0 w_1$ determined by $\omega_c = 0.5$.*

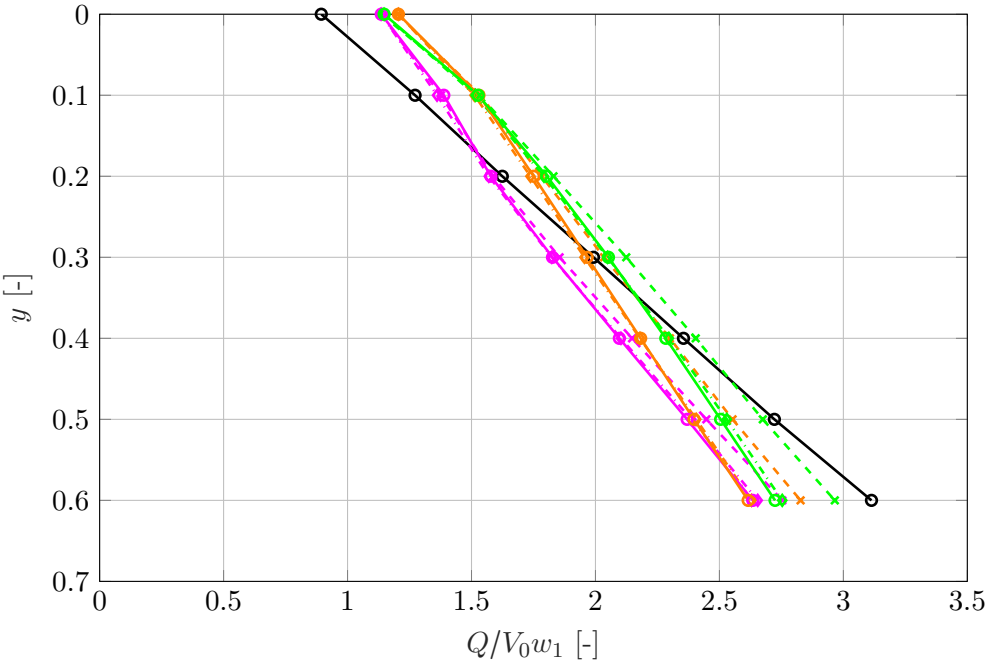

(b) *$Q/V_0 w_1$ determined by $\omega_c = 0.25$.*

Figure 5.9: *Dimensionless volume flux, $Q/V_0 w_1$, for different d and R.*

CFD model and the theoretical model have approximately the same magnitude. The x-velocity at the jet boundaries is expected to be smaller than the entrainment velocity, since V_x is not the velocity component perpendicular to the jet boundary. Hence, the y-component of the velocity at the jet boundaries has a contribution to the entrainment velocity as well. Figure 5.11 shows the streamlines through the boundary of the single jet. The streamlines show the direction of the velocity vector. The contribution of the y-velocity increases when moving downstream. Taking this into account, the velocity at the jet boundary perpendicular to the jet boundary will resemble the theoretical model and the entrainment velocity, V_E, more closely. The difference between $\omega_c = 0.5$ and $\omega_c = 0.25$ is almost negligible for the x-velocities, while the entrainment velocity obtained with $\omega_c = 0.5$ clearly provides a better approximation to the theory. Therefore, $\omega_c = 0.5$ is still considered a better definition of the jet boundary than $\omega_c = 0.25$.

Figure 5.12 shows the dimensionless entrainment velocity, V_E/V_0, for all configurations. The entrainment velocities follow similar trends for different velocity ratios R. Since the jets enter a (nearly) quiescent fluid, the higher the velocity of the jets, the higher the velocity gradients at the jet boundaries, resulting in more entrainment. Above the merging points ($y \sim 0 - 0.1$), air is only entrained by the secondary jets, hence the velocity of the secondary jets, V_2, determines the amount of entrainment. Thus, for higher V_2 (i.e. larger R), the entrainment velocities above the merging points is also higher. Downstream of the merging points, the jets start to combine, which results in a different downstream velocity. For $R = 1/2$, the downstream velocity increases compared to V_2, whereas for $R = 1$, the downstream velocity stays similar to V_2, and for $R = 2$,

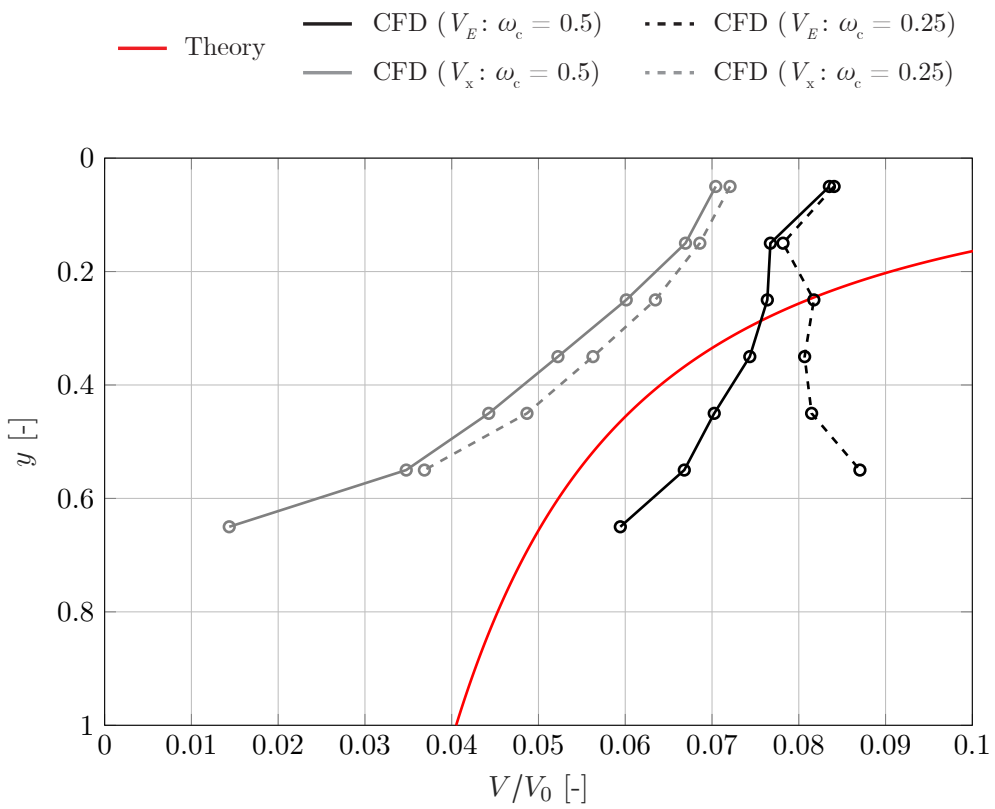

Figure 5.10: *Dimensionless entrainment velocity, V_E/V_0, and the dimensionless x-velocity, V_x/V_0, of a single jet, obtained with a CFD model and a theoretical model. The theoretical entrainment velocity is described by equation (2.26).*

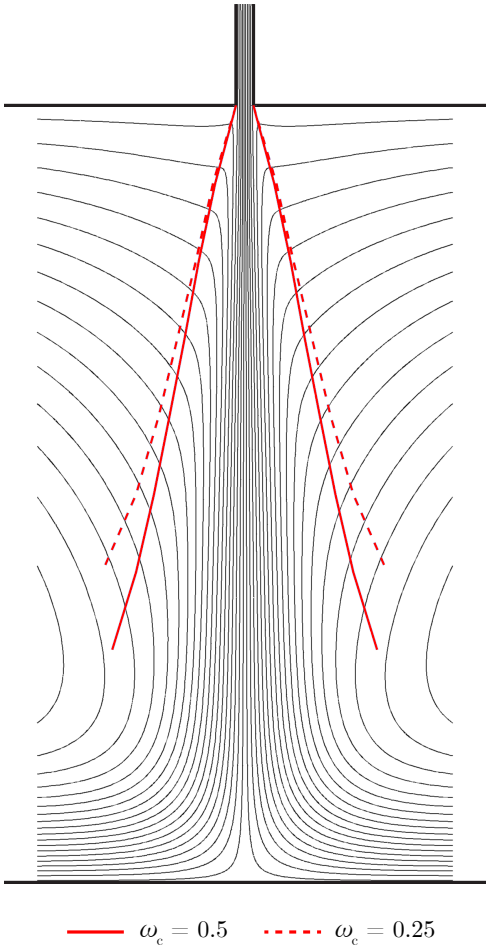

Figure 5.11: *Streamlines in the region of interest of the single jet model, with an indication of the jet boundaries obtained with* $\omega_c = 0.5$ *and* $\omega_c = 0.25$.

the downstream velocity decreases compared to V_2. Consequently, the entrainment velocity increases for $R = 1/2$, stays nearly constant for $R = 1$, and decreases for $R = 2$, as visualised in figure 5.12. For increasing d, the entrainment velocities decrease. Since the centreline velocities also decrease with increasing d, the velocity gradients at the jet boundaries are smaller, resulting in less entrainment. Figure 5.12 does not clearly show which configurations entrain less than others, therefore the average entrainment velocities for all configurations are given in table 5.3 and 5.4. The single jet entrains significantly more air ($\approx 140\%$) than the configurations with secondary jets. The entrainment decreases with increasing distance between the jets, d, which is also visible in figure 5.12. Also, the velocity ratio $R = 1$ results in the lowest entrainment. $R = 1/2$ and $R = 2$ give similar results, however, $R = 1/2$ results in low entrainment close to the nozzle ($y \approx 0 - 0.25$), and high entrainment further downstream ($y > 0.25$), which is oppositely for $R = 2$.

Figure 5.13 shows the dimensionless x-velocity at the jet boundaries, V_x/V_0, for all configurations. The x-velocities follow similar trends to the entrainment velocities. This can also be seen from the average values of V_x/V_0 in table 5.5 and 5.6. Since V_E/V_0 and V_x/V_0 show similar trends and magnitudes for $\omega_c = 0.5$, it can be concluded that the x-velocity at the jet boundaries gives a good representation of the entrainment velocity.

Table 5.3: *Average dimensionless entrainment velocity, $\langle V_E/V_0 \rangle$, for all d and R, determined by $\omega_c = 0.5$. All values are normalised with $\langle V_E/V_0 \rangle$ of the single jet configuration.*

$\langle V_E/V_0 \rangle$	$R = 1/2$	$R = 1$	$R = 2$
$d = \frac{4}{5}w_1$	0.76	0.74	0.82
$d = 2w_1$	0.71	0.64	0.72
$d = 4w_1$	0.70	0.63	0.70

Table 5.4: *Average dimensionless entrainment rate, $\langle V_E/V_0 \rangle$, for all d and R, determined by $\omega_c = 0.25$. All values are normalised with $\langle V_x/V_0 \rangle$ of the single jet configuration.*

$\langle V_E/V_0 \rangle$	$R = 1/2$	$R = 1$	$R = 2$
$d = \frac{4}{5}w_1$	0.73	0.73	0.82
$d = 2w_1$	0.68	0.64	0.72
$d = 4w_1$	0.68	0.64	0.71

Table 5.5: *Average dimensionless x-velocity on the jet boundaries, $\langle V_x/V_0 \rangle$, for all d and R, determined by $\omega_c = 0.5$. All values are normalised with $\langle V_x/V_0 \rangle$ of the single jet configuration.*

$\langle V_x/V_0 \rangle$	$R = 1/2$	$R = 1$	$R = 2$
$d = \frac{4}{5}w_1$	0.76	0.72	0.79
$d = 2w_1$	0.70	0.61	0.68
$d = 4w_1$	0.72	0.61	0.68

Table 5.6: *Average dimensionless x-velocity on the jet boundaries, $\langle V_x/V_0 \rangle$, for all d and R, determined by $\omega_c = 0.25$. All values are normalised with $\langle V_x/V_0 \rangle$ of the single jet configuration.*

$\langle V_x/V_0 \rangle$	$R = 1/2$	$R = 1$	$R = 2$
$d = \frac{4}{5}w_1$	0.73	0.72	0.80
$d = 2w_1$	0.69	0.62	0.71
$d = 4w_1$	0.71	0.63	0.71

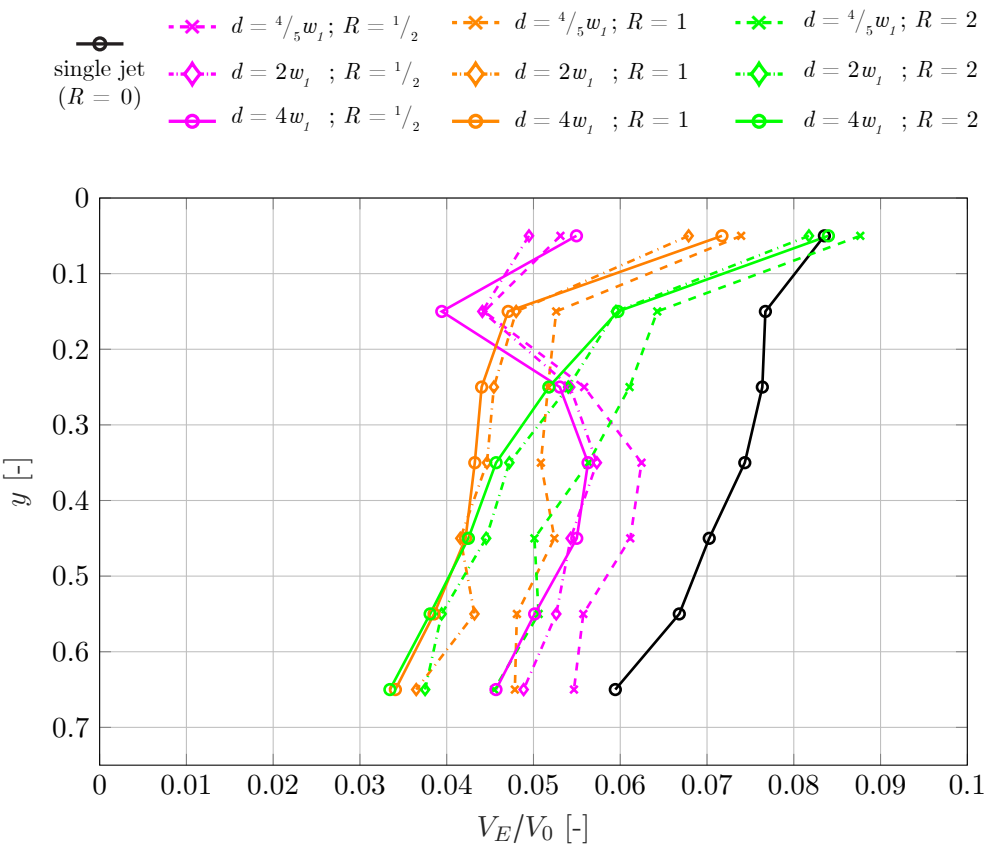

(a) V_E/V_0 *determined with* $\omega_c = 0.5$.

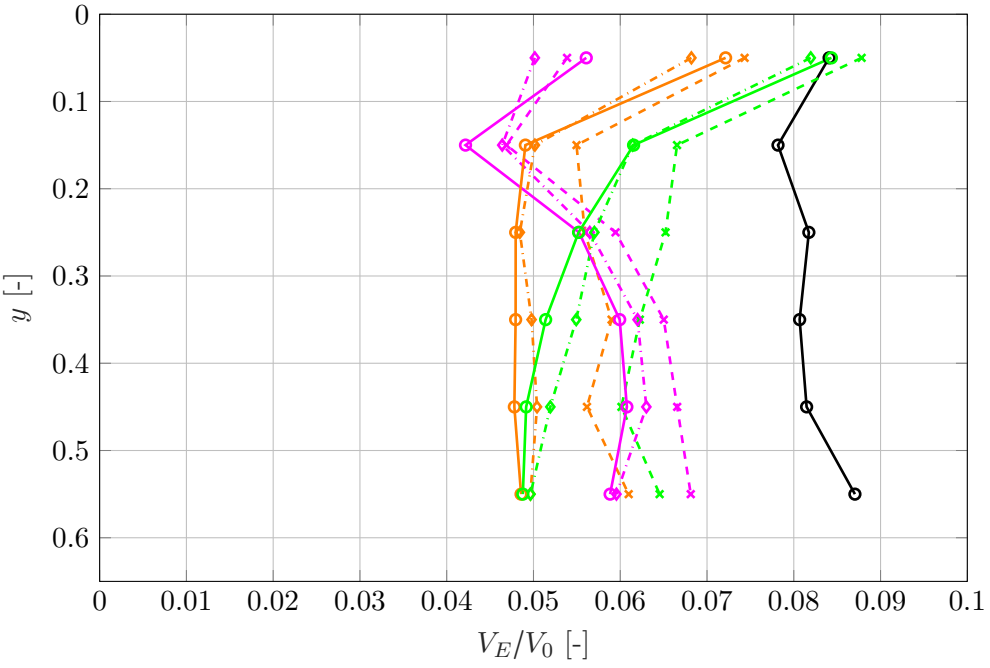

(b) V_E/V_0 *determined with* $\omega_c = 0.25$.

Figure 5.12: *Dimensionless entrainment velocity,* V_E/V_0*, for different* d *and* R.

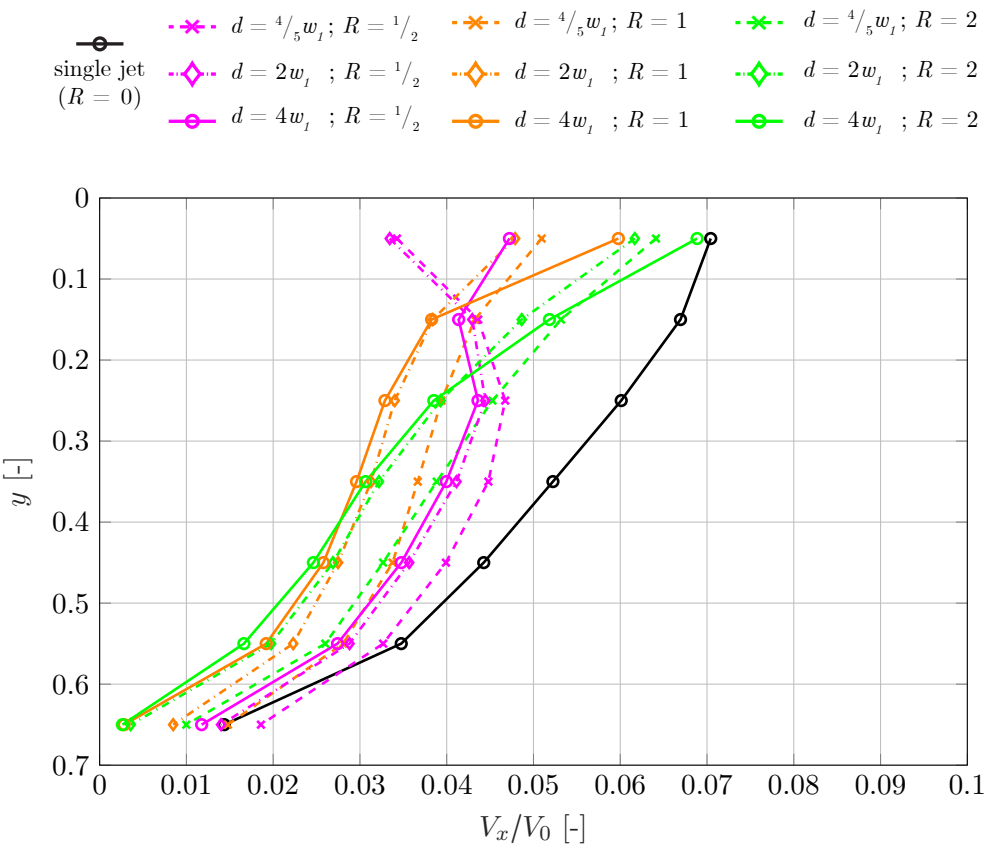

(a) *V_x/V_0 determined with $\omega_c = 0.5$.*

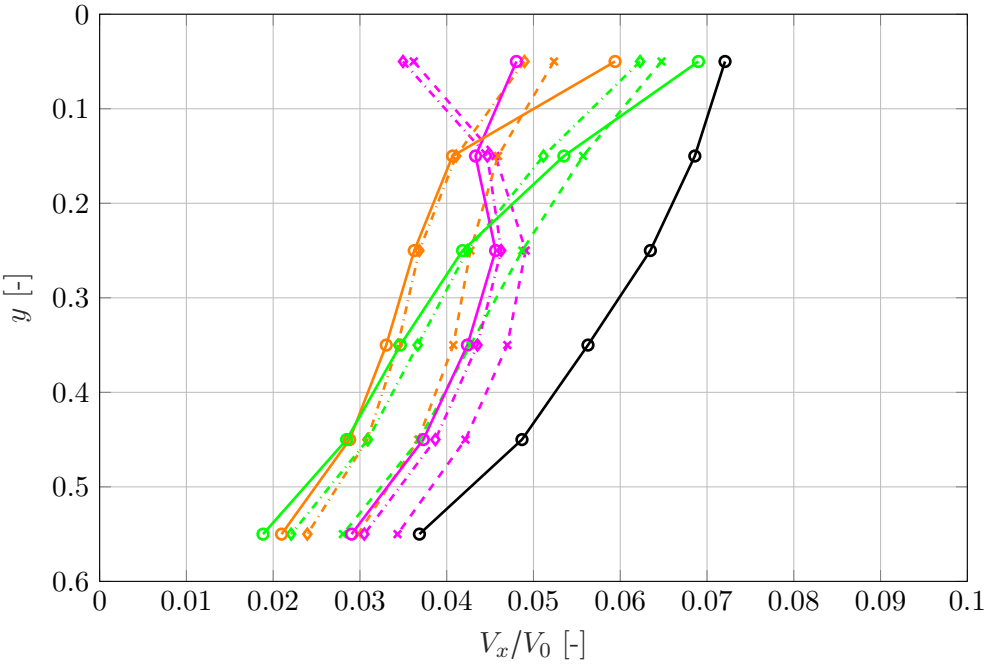

(b) *V_x/V_0 determined with $\omega_c = 0.25$.*

Figure 5.13: *Dimensionless entrainment velocity, V_x/V_0, for different d and R.*

5.3 Species transport

To directly measure the separation efficiency of the air curtain models, species transport is investigated using URANS simulations for the configurations with $d = \frac{4}{5}w_1$ and $d = 4w_1$.[3] A passive scalar called 'tracer air' is introduced as described in section 4.3.2. The mass fraction of tracer air, c_t, is measured during 150 s in the area at the right-hand side of the jet(s), and in nine points inside that area, as visualised in figure 5.14. The mass fraction always has a value between 0 and 1, corresponding to 0−100% of the concentration of tracer air in the measurement area or points. The size of the area in which the tracer air is measured has the same size as the area in which the tracer air is introduced at the left-hand side of the jet(s). Since that area is filled with 100% tracer air, the mass fraction of tracer air measured in the right area indicates the percentage of tracer air that passed across the jet(s).

Figure 5.15 shows the concentration of tracer air in the whole domain from the single jet model at different times t. At $t = 2$ s, it is clearly visible that tracer air is entrained by the jet at $y \sim 0.2 - 0.75$. The entrained tracer air is then transported downstream inside the jet. In the impingement zone, the mixture of normal air and tracer air is transported in horizontal direction to both sides of the domain due to advection, visible at $t > 10$ s. The tracer air then circulates through the domain due to advection, and spreads equally over the domain due to (turbulent) diffusion ($t > 25$ s).

5.3.1 Species transport across the air curtain

Figure 5.16 shows the mass fraction of tracer air from all configurations, measured for 150 s in the area indicated in figure 5.14. All configurations follow a similar trend; the gradient of c_t decreases gradually with time. This is because tracer air leaves the domain through the outlets and only normal air enters the domain through the inlets, so the available tracer air that can

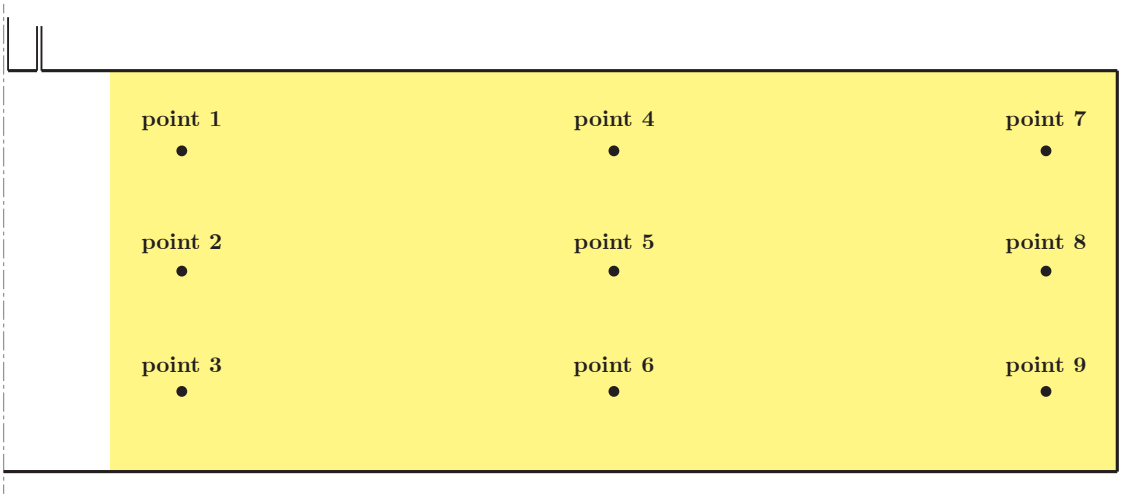

Figure 5.14: *Schematic of the right half of the domain. The yellow area indicates the area where the mass fraction of tracer air is measured. The points indicate the nine positions at which the mass fraction is measured.*

[3]The configurations with $d = 2w_1$ are omitted, since the results of velocity and entrainment do not differ much from the results with $d = 4w_1$. Therefore, the results of species transport are expected to not differ much either.

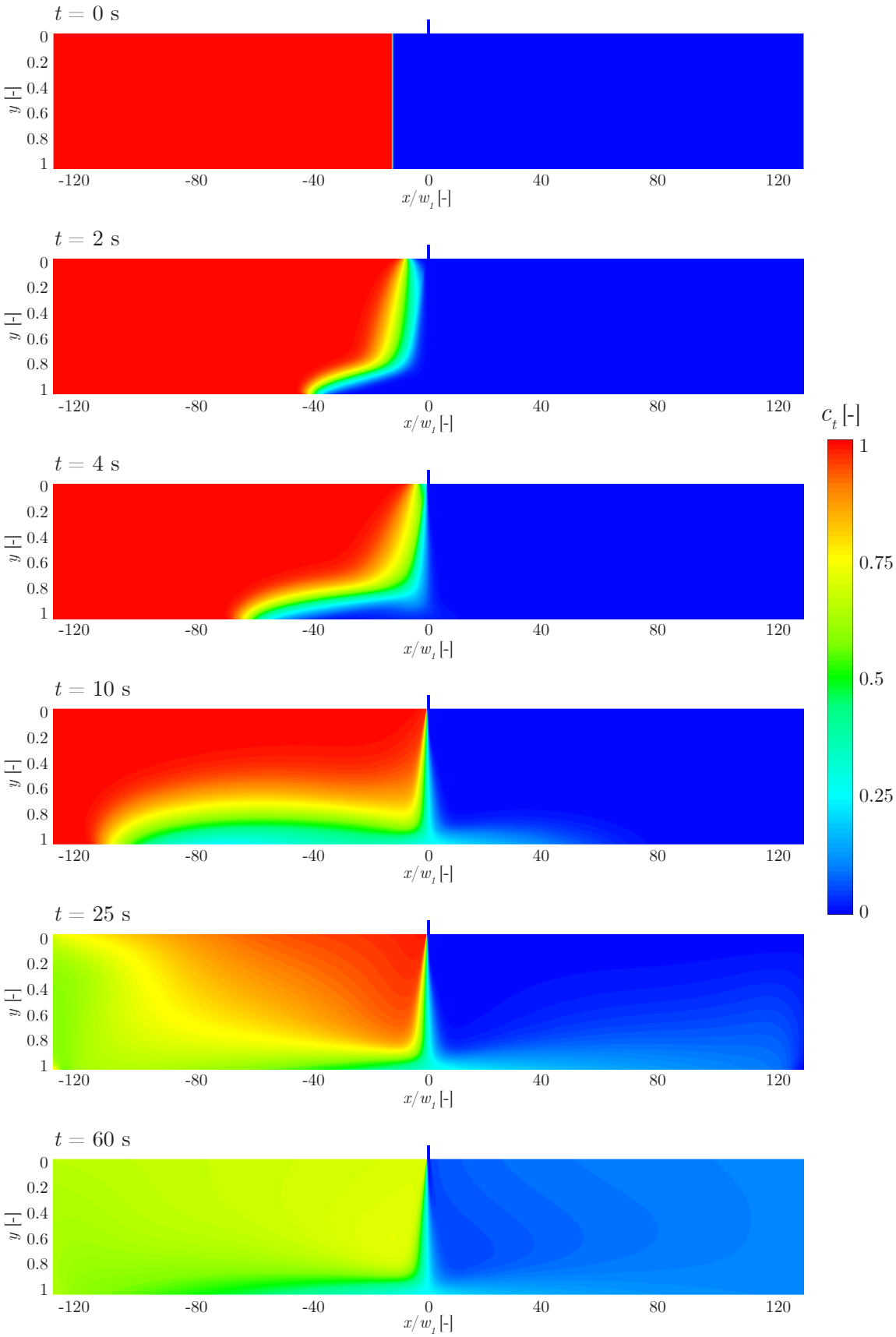

Figure 5.15: *Concentration of tracer air, c_t, in the whole domain of the single jet model at different time t.*

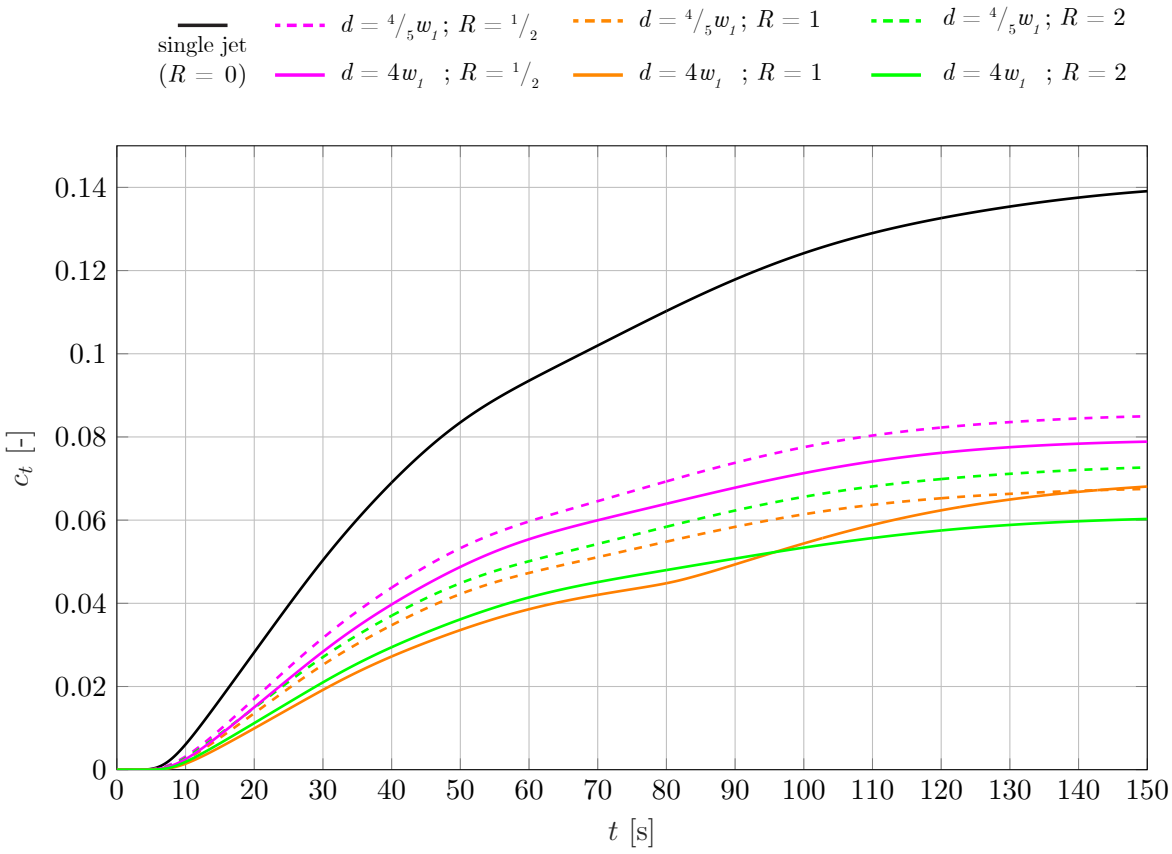

Figure 5.16: *Mass fraction of tracer air for different d and R measured in the area indicated in figure 5.14 for 150 s.*

transfer across the jet(s) reduces in time. Eventually ($t \gg 150$ s), this will lead to a decrease in tracer air in the right side of the domain until all tracer air has left through the outlets and is replaced by normal air. The single jet lets through approximately twice as much tracer air as the configurations with secondary jets. The difference between the configurations with secondary jets is also quite significant, leading up to a difference in c_t of approximately 50%. The species transport across the jets is smaller for larger d. However, larger spacings than $d = 4w_1$ are not investigated[4], hence an optimal separation distance has not been found. $R = 1$ and $R = 2$ give similar results, however, $R = 1/2$ results in more species transport across the jets. Since $R = 2$ results in slightly more species transport across the jets than $R = 1$, $R > 2$ is expected to result in a lower separation efficiency as well, therefore, it seems that $R \sim 1$ is the optimal velocity ratio.

As visible in figure 5.15, species first get entrained and then get transported downstream in the jet. Thus, the species transport seems to be dependent on the entrainment velocity as well as the (centreline) velocity of the jet. Consequently, a higher entrainment velocity causes a faster take-in of tracer air by the jet, and a higher centreline velocity causes a faster transport across the jet, resulting in more transport of species across the jet in time. From the analysis of the velocity and entrainment in sections 5.1 and 5.2, the single jet transports the largest amount of tracer air, since the entrainment velocity and the centreline velocity of the single jet

[4]Larger d have not been investigated due to model convergence problems. Steady RANS simulations could not be performed, and therefore, URANS simulations could not be initialised.

are significantly higher than those of the other configurations. Also, the centreline velocities decrease with increasing R and increasing d. The average entrainment velocities decrease with increasing d, but are the smallest for $R = 1$, and similar for $R = 1/2$ and $R = 2$. Therefore, the species transfer should decrease with increasing d, which can be observed in figure 5.16. The configurations with $R = 1/2$ have the highest centreline velocity, and therefore transport species quickly downstream through the jet. The configurations with $R = 2$ have low centreline velocities, but higher entrainment velocities, and the configurations with $R = 1$ have moderate centreline velocities, but the lowest entrainment velocities. As visualised in figure 5.16, the configurations with $R = 1$ transport slightly less species than the configurations with $R = 2$, and therefore it is assumed that the entrainment velocity has a larger effect on the species transport than the centreline velocity.

All configurations shown in figure 5.16 follow the same trend, except for the configuration with $d = 4w_1$ and $R = 1$. From $t \sim 80$ s, the concentration starts deviating from the results of the other configurations and a sudden increase in species transport is observed. The flow field of all configurations remained steady during the URANS simulations, except for the configuration with $d = 4w_1$ and $R = 1$. At $t \sim 80$ s the jets start experiencing a swaying motion called 'jet flapping'. This behaviour is visualised in figure 5.17. The jet flapping is also observed by Khayrullina et al. (2017), and reported and analysed in earlier studies, such as Goldschmidt and Bradshaw (1973) and Cervantes de Gortari and Goldschmidt (1981). The flapping motion may be a result of a small asymmetry or perturbation close to the nozzle.

The effect of jet flapping on the transport of species is visualised in figure 5.18. At $t = 60$ s, the jets are still steady and form a clear seal between both sides of the domain. Tracer air is only transported to the right side of the domain in the impingement zone, where the jets hit the bottom wall. At $t = 100$ s, the jets have started flapping and more tracer air gets entrained

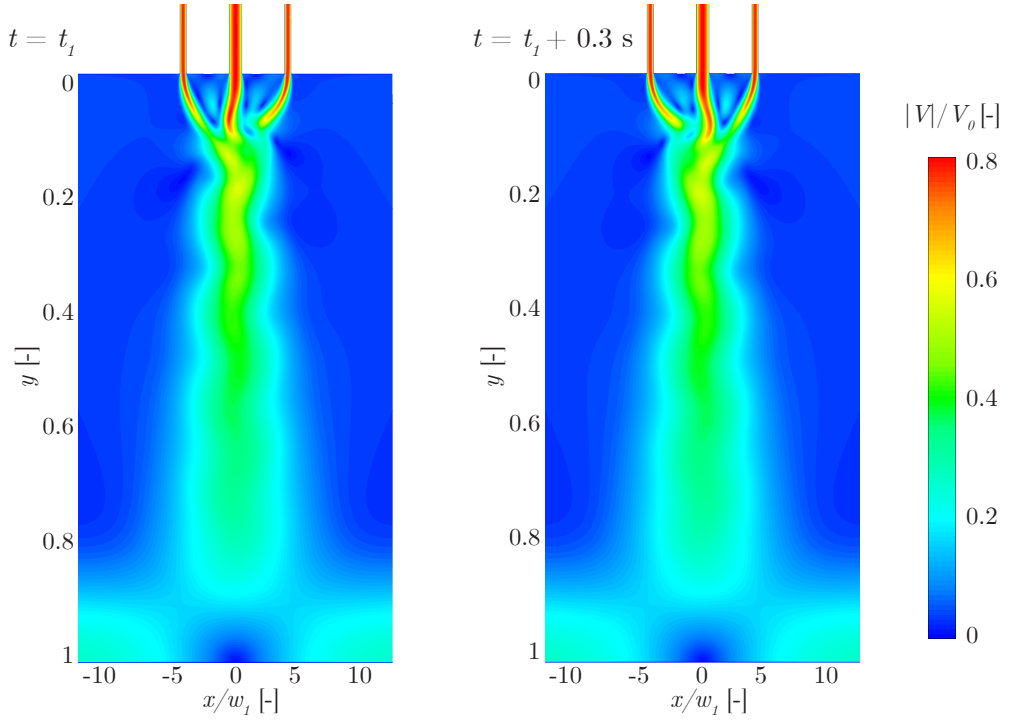

Figure 5.17: *Mean velocity magnitude, $|V|/V_0$, in the region of interest of the model configuration with $d = 4w_1$ and $R = 1$ at different time t.*

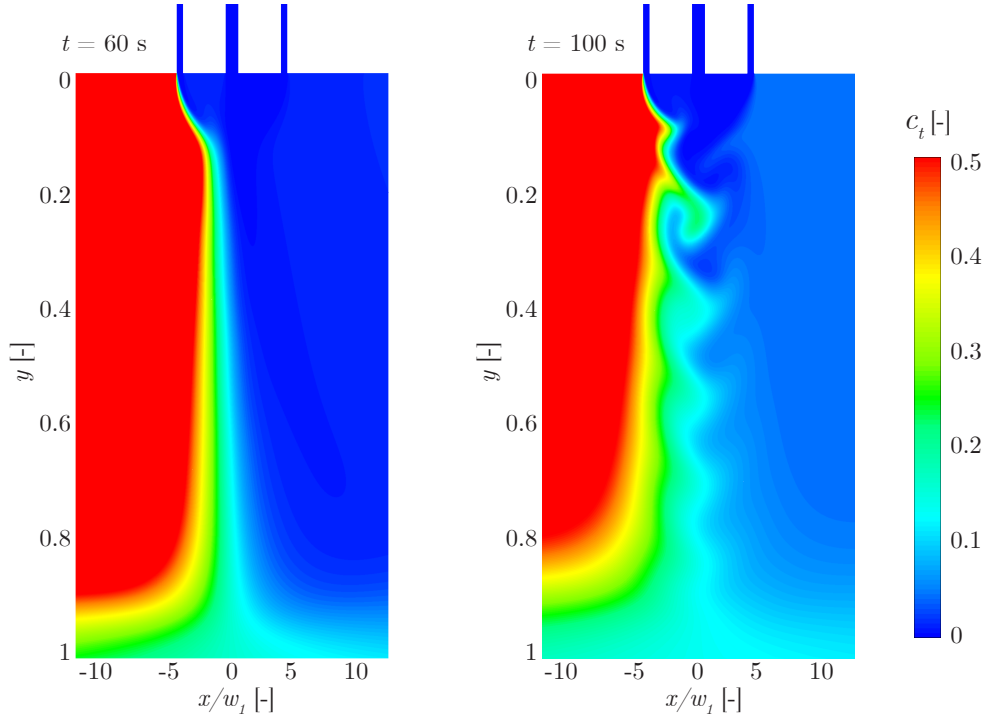

Figure 5.18: *Concentration of tracer air, c_t, in the region of interest of the model configuration with $d = 4w_1$ and $R = 1$ at $t = 60$ s and $t = 100$ s.*

due to the large turbulent motions. The jets do not form a clear seal any more, and tracer air is also leaving the jets at the sides instead of only at the bottom. Consequently, more tracer air is transported across the jets.

5.3.2 Species transport in the bounded domain

Figure 5.19 shows the concentration of tracer air, c_t, in nine points (figure 5.14), and reflects how the tracer air moves through the domain. In every point, c_t follows similar trends for every configuration, except for the configuration with $d = 4w_1$ and $R = 1$, due to the jet flapping. In contrast to the concentration measured in the volume, the concentration in the points does not increase gradually in time. Especially for points 3, 6, 7, 8 and 9, whose large gradients in the concentration are visible at certain t. For the single jet, c_t increases abruptly at $t \sim 10$ s in point 3, at $t \sim 15$ s in point 6, at $t \sim 23$ s in point 9, at $t \sim 26$ s in point 8, and at $t \sim 30$ s in point 7. This indicates a circular motion through the domain, as also visible in figure 5.15. Tracer air enters the domain around point 3 and circulates across points 6, 9, 8, 7, 4, 1, 2, respectively, to eventually return to point 3. Due to diffusion, the increase in concentration is more dominant for points 3, 6, 9, 8 and 7, and gradually decreasing in significance for points 4, 1 and 2. The jump in concentration is almost neglectable for point 5, since it is positioned in the middle of the domain and the tracer air is advected around it. The still present gradual increase in concentration at point 5 is almost solely due to diffusion. A second abrupt increase in concentration is visible at $t \sim 65$ s in point 3, at $t \sim 70$ s in point 6, at $t \sim 80$ s in point 9, at $t \sim 85$ s in point 8, and at $t \sim 90$ s in point 7. This implies that for the single jet configuration tracer air circulates through the domain in approximately 60 s.

To verify this, the circulation time is approximated by means of the stream function. For the configuration of the single jet, the stream function, ψ, in the right side of the domain is plotted

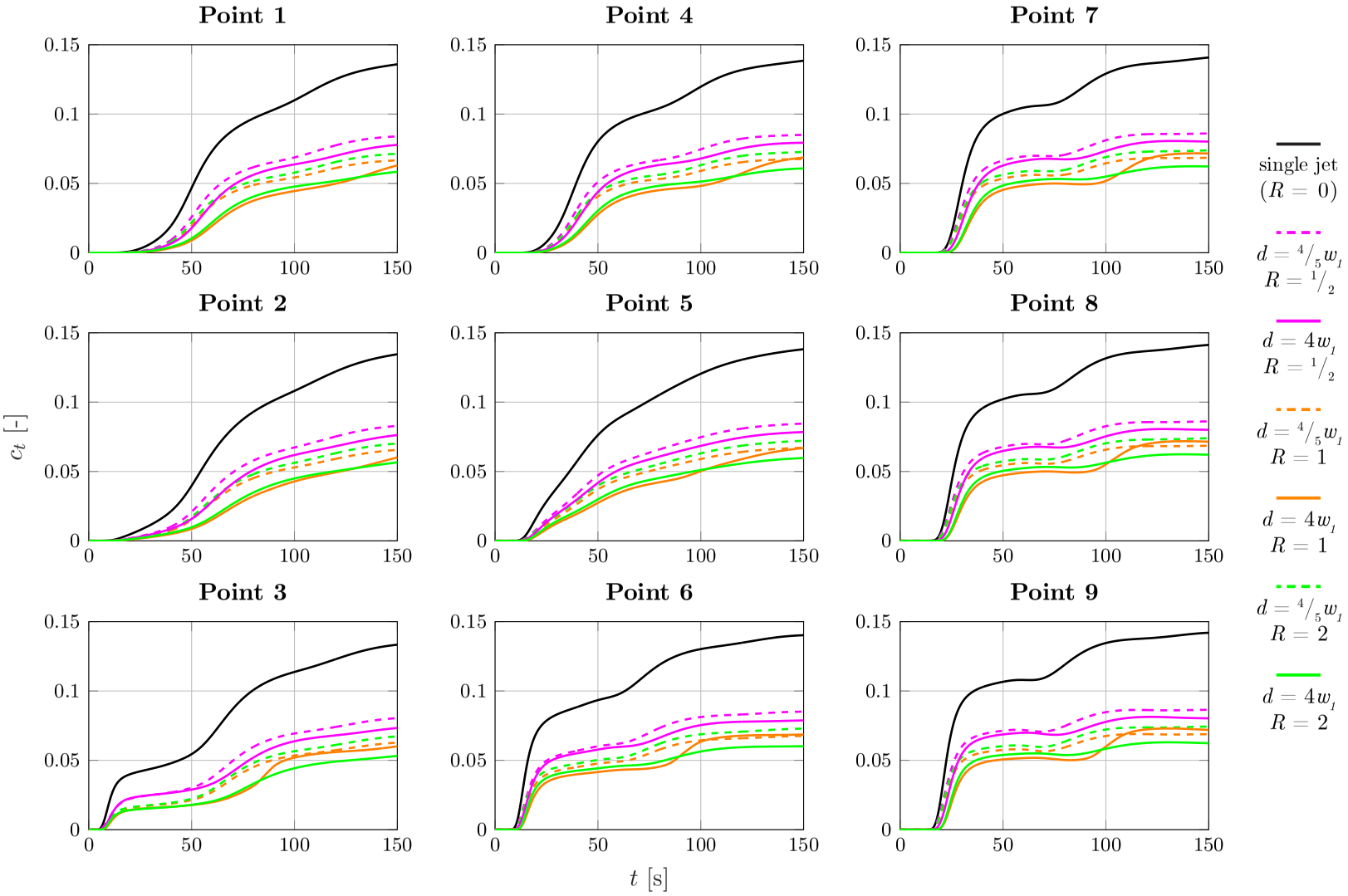

Figure 5.19: *Mass fraction of tracer air for different d and R measured in the points indicated in figure 5.14 for 150 s.*

Table 5.7: *Circulation time, T_c, and value of the dimensionless streamfunction, $\psi/V_0 w_1$, in nine points in the right side of the domain.*

	$\psi/V_0 w_1$ [-]	T_c [s]
Point 1	4.33	53.4
Point 2	5.17	64.3
Point 3	5.11	67.6
Point 4	4.77	64.4
Point 5	5.73	83.4
Point 6	4.91	60.2
Point 7	3.71	56.0
Point 8	3.90	50.4
Point 9	3.47	60.9
Average T_c [s]		**62.3**

in figure 5.20. The circular streamlines confirm the presence of a circulating motion. Since the flow of the single jet behaves steady, it is assumed that the streamlines represent the particle trajectories, i.e. the tracer air follows the streamlines. The streamlines through all nine points are determined, and by means of the velocity field, the time it takes for a particle to travel along each streamline is calculated. For the single jet, these circulation times, T_c, are presented in table 5.7 for each point. The average circulation time is approximately 60 s, which supports the observations in figure 5.19.

For the configurations with secondary jets, the abrupt increases in concentration of tracer air happen at later times, as visible in figure 5.19. Due to the smaller velocities of these configurations, it is expected that the velocities in the domain are also smaller, resulting in longer circulation times. For the configurations with $d = \frac{4}{5}w_1$, the abrupt increases in c_t happen at similar t as for the single jet configuration, which is expected since their centreline velocities are almost similar. The centreline velocities of the configurations with $d = 4w_1$ are smaller, and therefore the abrupt increases in c_t happen at later t.

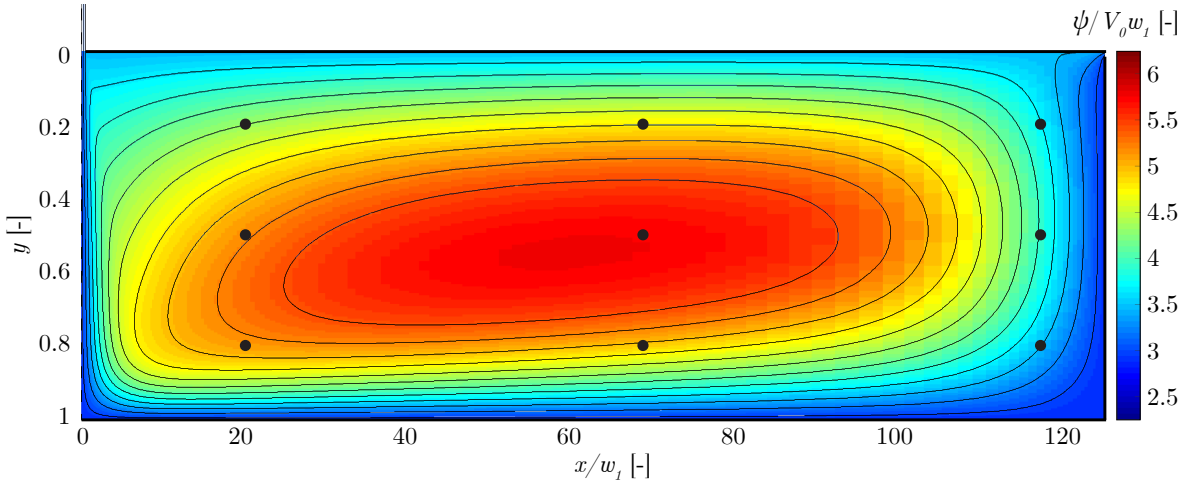

Figure 5.20: *Dimensionless streamfunction, $\psi/V_0 w_1$, in the right side of the domain. The black lines indicate streamlines.*

Chapter 6

Future work

The analysis on species transport in section 5.3 implies that a low centreline velocity is needed to decrease the species transfer across the air curtain. However, this only holds when there are no density differences present. In reality, density differences are often present as a result of temperature differences. Density differences induce free convection, and a flow is generated across the air curtain. Consequently, the air curtain bends to the low density side and does no longer form an optimal seal (Frank and Linden, 2014; Qi et al., 2018). Increasing the centreline velocity suppresses the bending (Gonçalves et al., 2012b), and therefore reduces the species transfer. However, increasing the centreline velocity also enhances the entrainment. Thus, an optimal velocity should be found to optimise the separation efficiency of an air curtain subjected to density differences. Costa et al. (2006) and Frank and Linden (2014) have found that such an optimal velocity exists for a single jet air curtain. Implementation of density differences in the CFD models is recommended, since it should give more insight in the optimal distance d between the jets. It is expected that a further increase of d will not reduce species transfer due to the decrease in centreline velocity. Further research should also point out whether $R \sim 1$ is still the optimal velocity ratio, since $R < 1$ result in higher centreline velocities, creating a more stable air curtain.

Furthermore, it is shown in section 5.3.1 that jet flapping enhances species transport across the jets. Jet flapping is caused by a small asymmetry or perturbation close to the nozzle (Goldschmidt and Bradshaw, 1973; Cervantes de Gortari and Goldschmidt, 1981). In reality, it can be expected that a jet is exposed to a lot of perturbations, and that small asymmetries in the nozzles are imminent. Therefore, it is expected that the jet flapping is more realistic than the steady behaviour. To gain a better understanding of the effect of jet flapping on the species transport, the unsteady RANS simulations should be performed for longer flow times. Also, Large Eddy Simulations (LES) could be performed to gain more insight in the flapping behaviour. LES solves all the large-scale motions and only models the small eddies. Therefore, it will always have superior performance compared to RANS and URANS (Wilcox, 2006). In addition, instantaneous values of the velocity field and the turbulence levels can be obtained with LES, in contrast to the RANS equations where only mean quantities are calculated. However, the use of LES comes with a strong increase in computational demand. Nevertheless, the differences between the steady configurations and the flapping configuration will then be more clear, and more accurate conclusions can be drawn. Furthermore, the results of other configurations that exhibit jet flapping should be compared.

Chapter 7

Conclusions

In this study, the influence of secondary jets on the separation efficiency of a PTIJ is investigated by means of 2D numerical (CFD) models. The distance d between the jets and the ratio of discharge velocities, $R = V_2/V_1$, are varied to find an optimal configuration. Steady and unsteady RANS simulations are performed to gather information about velocity, entrainment and species transport across the jets.

First, a theoretical model of a 2D plane jet is formulated. It is assumed that the cross-jet velocity profiles of the jet resemble Gaussians. By means of conservation of mass and momentum, expressions of the centreline velocity, cross-jet velocity, volume flux and entrainment velocity are formulated. The results from the theoretical model are in good agreement with the results of the CFD model of a 2D plane jet, especially when an opening angle of $\alpha = 1/6$ is considered, instead of the opening angle of $\alpha = 1/5$ as suggested in previous research. Nonetheless, the theoretical model only applies in the fully developed flow region, and thus does not apply to the full flow of the PTIJ. Additionally, the theoretical model assumes an unbounded domain, while the CFD model has a bounded domain, and therefore the flow at the boundaries of the jet exhibits different behaviour as well.

Furthermore, the centreline velocity and cross-jet velocity profiles, the volume flux and the entrainment velocity obtained with the CFD model configurations with secondary jets are compared with those obtained with the CFD model of a single jet. The centreline velocity is highest for the single jet, and decreases with increasing R and increasing d for the configurations with secondary jets. The dependence on d arises from the difference in shear between the jets. The smaller the distance between the jets, the less shear is present between them, reducing turbulence and preserving the centreline velocity. The dependence on R arises from the difference in shear at the outer boundaries of the secondary jets. The higher V_2, and thus R, the more shear at the outer boundaries, resulting in faster dissipation of the centreline velocity. The entrainment velocity of the single jet is significantly higher than that of the multiple jets. For the configurations with secondary jets, the entrainment velocity decreases with increasing d, as a result of the lower centreline velocities for larger d. The velocity ratio $R = 1$ results in a lower entrainment velocity than $R = 1/2$ and $R = 2$. For $R = 2$, higher entrainment velocities are due to higher shear at the outer boundaries. For $R = 1/2$, the higher centreline velocities result in higher entrainment velocities.

Lastly, the separation efficiency of the air curtain models is investigated by means of species transfer across the jets. The species transfer across the jets is dependent on the entrainment velocity, which controls the amount of species coming into the jet, and the centreline velocity,

which controls how fast the species are transported through the jets. The transfer of species across the jets decreases for increasing d. This is expected since large d results in low centreline velocities and low entrainment velocities. The transfer of species is highest for $R = 1/2$, since those configurations have the highest centreline velocity and a high entrainment velocity. The amounts of species transfer observed for the configurations with $R = 1$ and $R = 2$ are in the same order of magnitude. However, the species transfer is slightly less for $R = 1$, implying that the entrainment velocity plays a larger role than the centreline velocity on the species transfer through the jets. It can be concluded that an air curtain with secondary jets transfers significantly less species than a single jet air curtain. The results show that the secondary jets should have approximately the same velocity as the main jet ($R \sim 1$) to minimise the entrainment velocity. However, an optimal distance d between the jet has not been found. It is expected that when d is increased, the centreline velocity will decrease until the jets are too far apart to merge. Nevertheless, further research is needed to confirm this hypothesis.

Additional conclusions can be drawn on the effect of transient flow features on the results of species transport. First of all, an increase in species transport across the jets is shown as a result of jet flapping. The flapping behaviour generates more turbulence and increases the horizontal velocities, resulting in more transport of species across the jets. Secondly, circulating motions are observed in the bounded domain. By means of the stream function, the circulation time is determined for the single jet configuration. It is found that this circulation time can also be determined on the basis of the concentration gradient of species at certain points in the domain. Furthermore, it is shown that the circulation time decreases when the centreline velocity of the jet configurations decreases.

Overall, this numerical study shows that a more optimal separation efficiency of an air curtain is obtained by implementing secondary jets. The separation efficiency depends on the centreline velocity and the entrainment velocity of the air-curtain jets. This study shows that decreasing both velocities reduces the species transport across the jets. However, environmental parameters, such as density differences, are not taken into account, and should be investigated in future research.

Bibliography

ANSYS Inc. (2018). *ANSYS Fluent documentation (theory guide, users guide).* Release 19.0.

Beitelmal, A., Shah, A., and Saad, M. (2006). Analysis of an impinging two-dimensional jet. *Journal of Heat Transfer*, 128:307–310.

Celik, I. B., Ghia, U., Roache, P. J., Freitas, C. J., Coleman, H., and Raad, P. E. (2008). Procedure for Estimation and Reporting of Uncertainty Due to Discretization in CFD Applications. *Journal of Fluids Engineering*, 130(7):078001.

Cervantes de Gortari, J. and Goldschmidt, V. W. (1981). The apparent flapping motion of a turbulent plane jetfurther experimental results. *Journal of Fluids Engineering*, 103(1):119–126.

Cohen, R. E., Lide, D., and Trigg, G. (2003). *AIP Physics Desk Reference.* Springer-Verlag New York, third edition.

Colinet, J. F., Rider, J. P., and Thimons, E. D. (2006). Controlling respirable dust in underground coal mines in the United States. *The 21st World Mining Congress*, pages 231–238.

Costa, J. J., Oliveira, L. A., and Silva, M. C. (2006). Energy savings by aerodynamic sealing with a downward-blowing plane air curtain-A numerical approach. *Energy and Buildings*, 38(10):1182–1193.

Cushman-Roisin, B. (2014). *Environmental Fluid Mechanics.* Unpublished.

Elicer-Cortés, J. C., Demarco, R., Valencia, A., and Pavageau, M. (2009). Heat confinement in tunnels between two double-stream twin-jet air curtains. *International Communications in Heat and Mass Transfer*, 36(5):438–444.

Emmerich, S. J. and Persily, A. K. (1998). Energy Impacts of Infiltration and Ventilation in U.S. Office Buildings Using Multizone Airflow Simulation.

Frank, D. and Linden, P. F. (2014). The effectiveness of an air curtain in the doorway of a ventilated building. *Journal of Fluid Mechanics*, 756(May):130–164.

Frank, D. and Linden, P. F. (2015). The effects of an opposing buoyancy force on the performance of an air curtain in the doorway of a building. *Energy and Buildings*, 96:20–29.

Franke, J., Hellsten, A., Schlünzen, H., and Carissimo, B. (2007). *Best practice guideline for the CFD simulation of flows in the urban environment.* Number COST Action 732.

Fujisawa, N., Nakamura, K., and Srinivas, K. (2004). Interaction of two parallel plane jets of different velocities. *Journal of Visualization*, 7(2):135–142.

Goldschmidt, V. and Bradshaw, P. (1973). Flapping of a plane jet. *Physics of Fluids*, 16(3):354–355.

Gonçalves, J. C., Costa, J. J., Figueiredo, A. R., and Lopes, A. M. (2012a). CFD modelling of aerodynamic sealing by vertical and horizontal air curtains. *Energy and Buildings*, 52:153–160.

Gonçalves, J. C., Costa, J. J., Figueiredo, A. R., and Lopes, A. M. (2012b). Study of the aerodynamic sealing of a cold store - Experimental and numerical approaches. *Energy and Buildings*, 55:779–789.

Gutmark, E., Wolfshtein, M., and Wygnanski, I. (1978). The plane turbulent impinging jet. *Journal of Fluid Mechanics*, 88(4):737–756.

Guyonnaud, L., Solliec, C., Dufresne de Virel, M., and Rey, C. (2000). Design of air curtains used for area confinement in tunnels. *Experiments in Fluids*, 28:377–384.

Hendrix, W., Henderson, D., and Jackson, H. (1989). Infiltration heat gains through cold storage room doorways. *ASHRAE Transactions (American Society of Heating, Refrigerating and Air-Conditioning Engineers)*, 95, Part 2.

Jones, W. P. and Launder, B. E. (1972). The prediction of laminarization with a two-equation model of turbulence. *International Journal of Heat and Mass Transfer*, 15(2):301–314.

Khayrullina, A., van Hooff, T., Blocken, B., and van Heijst, G. J. (2017). PIV measurements of isothermal plane turbulent impinging jets at moderate Reynolds numbers. *Experiments in Fluids*, 58(4):1–16.

Kotsovinos, N. E. (1976). A note on the spreading rate and virtual origin of a plane turbulent jet. *Journal of Fluid Mechanics*, 77(2):305–311.

Krajewski, G. (2013). Efficiency of air curtains used for seperating smoke free zones in case of fire. In *13th Conference of International Building Performance Simulation Association*.

Kundu, P. K., Cohen, I. M., and Dowling, D. R. (2016). *Fluid Mechanics*. Sixth edition.

Launder, B. and Spalding, D. (1974). The numerical computation of turbulent flows. *Computer Methods in Applied Mechanics and Engineering*, 3(2):269–289.

Launder, B. E. (1989). Second-moment closure and its use in modelling turbulent industrial flows. *International Journal for Numerical Methods in Fluids*, 9(8):963–985.

Maurel, S. and Solliec, C. (2001). A turbulent plane jet impinging nearby and far from a flat plate. *Experiments in Fluids*, 31(6):687–696.

Menter, F. R. (1994). Two-equation eddy-viscosity turbulence models for engineering applications. *AIAA Journal*, 32(8):1598–1605.

Miller, D. R. and Comings, E. W. (1960). Force-momentum fields in a dual-jet flow. *Journal of Fluid Mechanics*, 7(2):237 – 256.

Nasr, A. and Lai, J. C. (1997). Two parallel plane jets: Mean flow and effects of acoustic excitation. *Experiments in Fluids*, 22(3):251–260.

Pope, S. B. (2000). *Turbulent Flows*. Cambridge university press.

Qi, D., Goubran, S., Wang, L. L., and Zmeureanu, R. (2018). Parametric study of air curtain door aerodynamics performance based on experiments and numerical simulations. *Building and Environment*, 129:65–73.

Reynolds, O. (1895). On the dynamical theory of incompressible viscous fluids and the determination of the criterion. *Philosophical Transactions of the Royal Society of London. A*, 186:123–164.

Roache, P. J. (1994). A method for uniform reporting of grid refinement studies. *Journal of Fluids Engineering*, 116:405–413.

Shih, T.-H., Zhu, J., and Lumely, J. L. (1994). A New Reynolds Stress Algebraic Equation Model. *Nasa Technical Memorandum*, (August).

Shih, Y. C., Yang, A. S., and Lu, C. W. (2011). Using air curtain to control pollutant spreading for emergency management in a cleanroom. *Building and Environment*, 46(5):1104–1114.

Shuja, S. Z., Yilbas, B. S., and Budair, M. O. (1999). *Gas jet impingement on a surface having a limited constant heat flux area: Various turbulence models*, volume 36.

Tanaka, E. (1970). The interference of two-dimensional parallel jets: 1st report, experiments on dual jet. *Bulletin of JSME*, 13(56):272 – 280.

Tanaka, E. (1974). The interference of two-dimensional parallel jets: 2nd report, experiments on the combined flow of dual jet. *Bulletin of JSME*, 17(109):920 – 927.

Townsend, A. A. (1970). Entrainment and the structure of turbulent flow. *Journal of Fluid Mechanics*, 41(part 1):13–46.

Turner, J. S. (1986). Turbulent entrainment: the development of entrainment assumption, and its application to geophysical flows. *Journal of Fluid Mechanics*, 173:431–471.

Welty, J. R., Wicks, C. E., Rorrer, G., and Wilson, R. E. (2009). *Fundamentals of Momentum, Heat, and Mass Transfer*. John Wiley & Sons, sixth edition.

Wilcox, D. C. (2006). *Turbulence Modeling for CFD*. DCW industries La Canada, CA, third edition.

Yakhot, V., Orszag, S. A., Thangam, S., Gatski, T. B., and Speziale, C. G. (1992). Development of turbulence models for shear flows by a double expansion technique. *Physics of Fluids A*, 4(7):1510–1520.

Appendix A

Validation metrics

Table A.1: *The factor of 1.1 of the observations, FAC1.1, defined for the dimensionless mean velocity magnitude along four lines in the region of interest, obtained with six different turbulence models.*

FAC1.1	**SKE**	**RNG**	**RKE**	**BSL**	**SST**	**RSM**
centreline	0.922	0.722	0.756	0.861	0.800	0.278
y = 0.8	0.722	0.204	0.830	0.793	0.747	0.102
y = 0.5	0.565	0.338	0.791	0.792	0.699	0.236
y = 0.2	0.482	0.574	0.560	0.653	0.222	0.218
Average	**0.673**	**0.460**	**0.734**	**0.775**	**0.617**	**0.208**

Table A.2: *The normalised mean squared error, NMSE, defined for the dimensionless mean velocity magnitude along four lines in the region of interest, obtained with six different turbulence models.*

NMSE	**SKE**	**RNG**	**RKE**	**BSL**	**SST**	**RSM**
centreline	0.0061	0.0082	0.0075	0.0066	0.0068	0.0158
y = 0.8	0.0043	0.0140	0.0006	0.0012	0.0009	0.0345
y = 0.5	0.0077	0.0092	0.0009	0.0046	0.0051	0.0252
y = 0.2	0.0084	0.0055	0.0058	0.0045	0.0056	0.0069
Average	**0.0066**	**0.0092**	**0.0037**	**0.0042**	**0.0046**	**0.0206**

Table A.3: *The correlation coefficient, R_p, defined for the dimensionless mean velocity magnitude along four lines in the region of interest, obtained with six different turbulence models.*

$\mathbf{R_p}$	**SKE**	**RNG**	**RKE**	**BSL**	**SST**	**RSM**
centreline	0.980	0.979	0.981	0.979	0.978	0.973
y = 0.8	0.995	0.995	0.988	0.989	0.990	0.995
y = 0.5	0.995	0.995	0.995	0.995	0.994	0.995
y = 0.2	0.992	0.992	0.991	0.992	0.992	0.990
Average	**0.990**	**0.990**	**0.989**	**0.989**	**0.988**	**0.988**

Table A.4: *The factor of 1.5 of the observations, FAC1.5, defined for the dimensionless TKE along four lines in the region of interest, obtained with six different turbulence models.*

FAC1.5	**SKE**	**RNG**	**RKE**	**BSL**	**SST**	**RSM**
centreline	0.929	0.880	0.782	0.880	0.803	0.820
$y = 0.8$	1	1	1	1	0.903	1
$y = 0.5$	1	1	0.772	0.753	0.634	1
$y = 0.2$	0.482	0.663	0.674	0.724	0.724	0.138
Average	**0.853**	**0.886**	**0.807**	**0.839**	**0.766**	**0.739**

Table A.5: *The normalised mean squared error, NMSE, defined for the dimensionless TKE along four lines in the region of interest, obtained with six different turbulence models.*

NMSE	**SKE**	**RNG**	**RKE**	**BSL**	**SST**	**RSM**
centreline	0.056	0.045	0.180	0.045	0.164	0.097
$y = 0.8$	0.036	0.005	0.049	0.051	0.080	0.031
$y = 0.5$	0.024	0.004	0.020	0.038	0.071	0.010
$y = 0.2$	0.233	0.248	0.335	0.285	0.258	0.243
Average	**0.087**	**0.075**	**0.146**	**0.105**	**0.143**	**0.095**

Table A.6: *The correlation coefficient, R_p, defined for the dimensionless TKE along four lines in the region of interest, obtained with six different turbulence models.*

$\mathbf{R_p}$	**SKE**	**RNG**	**RKE**	**BSL**	**SST**	**RSM**
centreline	0.849	0.810	0.633	0.713	0.786	0.750
$y = 0.8$	0.989	0.973	0.990	0.991	0.989	0.986
$y = 0.5$	0.993	0.991	0.993	0.993	0.987	0.993
$y = 0.2$	0.976	0.968	0.962	0.962	0.963	0.940
Average	**0.952**	**0.936**	**0.894**	**0.915**	**0.931**	**0.917**